SCUOLA DI DOTTORATO
UNIVERSITÀ DEGLI STUDI DI MILANO-BICOCCA

Dipartimento di / Department of **Physics**

Dottorato di Ricerca in / PhD program in **Astronomy and Physics** Ciclo / Cycle **XXXVIII**

DYNAMICS OF SPIN-PRECESSING AND ECCENTRIC COMPACT BINARIES IN POST-NEWTONIAN THEORY

Cognome / Surname **Fumagalli** Nome / Name **Giulia**

Matricola / Registration number **825592**

Tutore / Tutor: **Michele Fumagalli**

Supervisor: **Davide Gerosa**

Coordinatore / Coordinator: **Stefano Ragazzi**

ANNO ACCADEMICO / ACADEMIC YEAR 2024/2025

Doctoral School
University of Milano-Bicocca

Dynamics of spin-precessing and eccentric compact binaries in post-Newtonian theory

by

Giulia Fumagalli

A thesis submitted to the University of Milano-Bicocca for the degree of

Doctor of Philosophy

Supervised by

Prof. Davide Gerosa

Department of Physics "Giuseppe Occhialini"
Ph.D. program in Physics and Astronomy
Cycle XXXVIII

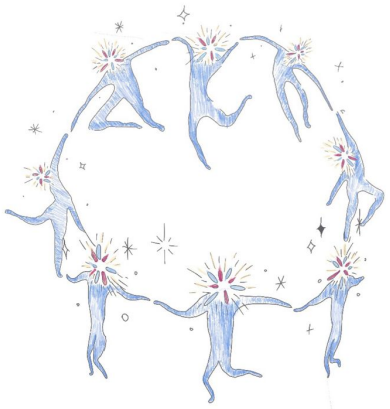

Do you not see that humanity could still go on living — it could live without science, it could live without bread — but only without beauty, it could no longer live, because there would be nothing left to do in the world! The whole secret is here, the whole story is here. Science itself would not last a minute without beauty — do you realize that, you who laugh? It would turn into vulgarity; you would not even fashion a single nail! … I will not yield!

Ma lo sapete voi che l'umanità può ancora vivere, può vivere senza la scienza, può vivere senza pane, ma soltanto senza la bellezza non potrebbe più vivere, perché non ci sarebbe più niente da fare al mondo! Tutto il segreto è qui, tutta la storia è qui. La scienza stessa non resisterebbe un minuto senza la bellezza, lo sapete voi, questo, voi che ridete? Si trasformerebbe in volgarità, non inventereste nemmeno un chiodo! … Io non cedo!

"Demons" ("I demoni"), Dostoevskij

Abstract

Understanding the dynamics of compact-object binaries is at the core of gravitational-wave astronomy. It enables not only the detection and characterization of gravitational signals but also the reconstruction of the astrophysical origins of compact objects like black holes, neutron stars, and their binary systems. Over the past decade, this knowledge has led to the detection of nearly 220 stellar-mass binary mergers and provided compelling evidence for a gravitational waves stochastic background from supermassive black hole binaries. Yet, the full exploration of the dynamical complexity of these systems remains incomplete, and the question of their origin is still open.

This thesis takes a step toward closing this gap by developing a post-Newtonian formalism to describe the evolution of spinning and eccentric black hole binaries, representing the most general and astrophysically relevant configuration at both stellar and supermassive scales. Spin precession and orbital eccentricity encode crucial information about binary formation, and only by treating them jointly can their dynamics be fully captured and exploited to retrieve the formation history it carries. The framework introduced here provides an efficient and robust description of these coupled effects, possibly paving the way for population-level studies of such systems and, ultimately, connecting gravitational-wave observations to their astrophysical origins.

Acknowledgments

"I don't know half of you half as well as I should like; and I like less than half of you half as well as you deserve."

–Tolkien (1954)

Writing this section is not easy since I have to thank so many people whom I met during the three years. I will surely forget someone, but I will try my best.

First on my list is Davide, the best supervisor one could hope for. I feel incredibly fortunate to have had the opportunity to do my Ph.D. under his guidance. I have deeply enjoyed every scientific and non-scientific conversation we have shared, as well as the excitement of new discoveries and the beauty of understanding something previously unknown. I want to thank him not only for his invaluable scientific contribution but also for his constant care over the past three years. There was never a meeting without him asking how I was, never a time he said no when I needed to talk, and he always found time to listen to me, even on personal matters. He is a true mentor, and if I ever reach his position [1], I can only hope to be half as good as he is. Finally, I want to thank him for teaching me how to do research, how academia works, and even how to climb a via ferrata; for the countless hikes in our beautiful mountains; for all the coffees I owe him; and for his guidance in shaping my career. Every one of my academic achievements will always be his as well.

[1] If I will not be able to stay in academia, I will open a bakery. Even in that case, I hope to be as kind and passionate about my job as Davide. Let's see in ten years if I will be writing papers or baking cookies.

Then I want to thank Nick, with whom I had the pleasure of working closely during the second and third years of my Ph.D. He is an amazing and patient collaborator who, as Davide, always had time for me and my countless questions about post-Newtonian stuff. Of which I reckon he is the most excellent expert. I have the feeling that I will continue to return to him with countless questions throughout the rest of my career.

I want to thank two Ph.D. students who have been important to me over these three years: Viola and Matteo. Viola, being a year ahead of me, has been my reference point at the beginning and has become a great friend. I want to thank her for her kindness and generosity in helping me and for all the fun we had together. Then I want to thank Matteo, with whom I share countless coffees in the morning and countless hours talking/complaining about eccentricity. He is a great colleague and I am happy to have had the opportunity to work with him.

Then I want to thank the postdocs and other Ph.D. students of our *gwfun* group: Alex, Alice, Arianna, Caroline, Chiara, Costantino, Daria, Federico, Matt, Michele, Pippa, Rodrigo, Ssohrab, and Tristan. You are a fantastic group, both scientifically and personally. I had a great time with you all, and I hope you enjoyed my cakes and cookies.

Thank you to the magic *AstroWappeu* group. How could I do all this work without our electric moka after lunch? Thank you for all your kindness, fun, and energy. Having people who care about each other is extremely valuable! Thank you.

I want to thank Golam, who has always cared deeply for me and all the Ph.D. students, supporting us with cookies and kindness. His constant presence and encouragement have accompanied every step of this journey, and he stands as a witness to all my achievements. For this, I am truly grateful.

Thank you to all the people in the astrophysics department. Working in a nice and

friendly environment is very precious. I feel so lucky to have spent all these years here. I want to thank Alessia, Irene, Cecilia, and Elisa for their help with the construction and all the initiative of *astroDEI*. We aimed to make our department an even better place in terms of inclusivity, diversity, and equity, and we tried our best to turn this vision into reality.

All of this work would not have been possible without my friends and family, whom I wish to thank in my own linguaggio. Grazie ai miei genitori e a mio fratello Marco per avermi sostenuto durante questi tre anni di dottorato nonostante non sia sempre facile capire quello che faccio. Grazie alla Zia Mariangela, allo Zio Paolo e ai miei cugini Andrea, Anna e Giorgio, per avermi ospitato durante il primo anno del dottorato nella loro casa e per avermi accolto come una nuova figlia e sorella. Grazie a Tia, Ale, Patti, Laura, Beppe, Marty, Piant e Giano per essere i migliori amici che una persona possa sperare di avere. Non sarei andata da nessuna parte senza di voi, grazie infinite per tutto il bene che mi volete e per essermi sempre vicino. Infine, grazie a Vale, la persona più importante di tutte. Il sogno di passare una vita insieme a lui mi ha spinta a dare il meglio di me durante il dottorato. Senza il suo amore e la sua infinita pazienza, nulla di tutto questo sarebbe stato possibile.

Ho ricevuto molto più amore e supporto di quanto abbia mai potuto restituire, o di quanto avessi mai potuto aspettarmi. A tutti voi, grazie ancora di cuore.

I received far more love and support than I could ever give back, or than I ever expected. To all of you, thank you once again from the bottom of my heart.

Funding

Giulia Fumagalli is supported by ERC Starting Grant No. 945155–GWmining, Cariplo Foundation Grant No. 2021-0555, MUR PRIN Grant No. 2022-Z9X4XS, the

ICSC National Research Centre funded by NextGenerationEU, Sigma Xi Grant No. G20230315-4609 and an Erasmus+ scholarship.

Contents

List of Figures

List of Tables

Chapter 1

Introduction

The coupling of spin vectors with the orbital angular momentum vector, and among themselves, is a clear prediction of general relativity (GR), while eccentric orbits represent the most generic closed trajectories that a binary system can follow. When combined, these two elements give rise to rich and complex dynamics. Nature provides many mechanisms for such a combination, particularly in compact-object binaries such as black holes (BHs) and neutron stars (NSs). Despite a long history of attempts to construct equations describing this dynamics (reviewed in Sec. 1.1 of this chapter), its full phenomenology has remained relatively unexplored. This thesis aims to carry out such an exploration.

More specifically, we study the dynamics of spin-precessing and eccentric BH binaries within the framework of post-Newtonian theory. Beyond their theoretical interest, these systems are especially relevant to current gravitational-wave (GW) astronomy, as both spin precession and eccentricity leave distinctive imprints on the GW signal. Detecting these features, as discussed in Sec. 1.2, would bring us closer to addressing the already decade-old question of the origin and formation channels of compact-object binaries.

In Sec. 1.3 we introduce the geometrical framework necessary to describe the evolution of eccentricity and spin precession. This framework provides the foundation for all the original results presented in the subsequent chapters.

This chapter is a review of prior work and does not contain material previously published by the author in this form.

1.1 The two-body problem in post-Newtonian theory

> *"The two-body problem in general relativity has a long and tortuous history."*
>
> *–Lincoln and Will (1990)*

Understanding the dynamics of a system of extended bodies moving under each other's gravity is a long-standing problem in physics. Initiated by Newton's *Principia* and significantly advanced by Einstein's theory of GR, the solution of this problem remains a driving force in theoretical astrophysics to this day. This thesis, along with the references within, serves as proof of it.

Of particular importance is the case of a system composed of two comparable-mass spinning bodies moving on eccentric orbits (see Sec 1.2 for motivation). In Newtonian mechanics, deriving the equations of motion for a two-body system on arbitrary orbits is straightforward, and the intrinsic angular momenta, i.e., the spins, of the bodies do not affect their dynamics. However, in GR, the situation is considerably more complex, and, as will be detailed in the following sections and chapters, both the spins and the orbital shape play a fundamental role in the system's motion.

Solving the full general relativistic equations of motion is both highly nontrivial and computationally demanding. Therefore, progress on the two-body problem has been closely tied to the still ongoing development of approximation methods. Among the first,

and still one of the most widely used, is the post-Newtonian (PN) approximation (see Ref. [9] for a review of PN theory). This framework assumes that gravitational fields around the bodies are weak and their characteristic velocities, v, are small compared to the speed of light, c. With Newtonian gravity as its lowest-order limit, the PN approximation systematically expands the equations of motion in powers of the small parameter $\epsilon \approx (v/c)^2 \approx GM/rc^2$, where G is the gravitational constant, M is the total mass of the system, and r is its orbital separation. Practically, this means that the expression for the acceleration of a two-body system can be written as

$$\boldsymbol{a} \equiv \frac{\mathrm{d}^2\boldsymbol{r}}{\mathrm{d}t^2} \approx -\frac{GM\boldsymbol{n}}{r^2}\left[1 + \mathcal{O}(\epsilon) + \mathcal{O}(\epsilon^2) + \mathcal{O}(\epsilon^{5/2}) + \cdots\right], \tag{1.1}$$

where $\boldsymbol{r}$ is the separation vector and $\boldsymbol{n} = \boldsymbol{r}/r$. The terms proportional to even powers of c^{-1} are denoted as conservative terms, while those proportional to odd powers are dissipative terms. This distinction reflects the fact that gravitationally radiating systems, such as a relativistic binary, break the time-reversal symmetry of the theory. In this thesis, dynamics is considered only within the PN framework, with spin effects limited to the conservative sector, while eccentricity is considered in both conservative and dissipative dynamics.

The first term of PN expansion was derived in 1938 for a non-spinning two-body system by Einstein *et al.* (1938) and describes the pericenter precession [11], which historically provided one of the first empirical confirmations of GR [12]. Around the same period, several groups worked on deriving the equations of motion for spinning bodies [13, 14]; however, these efforts primarily focused on the test-mass limit rather than on two-body systems with comparable masses. In the 1960s, new terms of PN expansion were found. Peters and Mathews (1963) and Peters (1964) explicitly derived

the effect of gravitational radiation on the dynamics of a comparable-mass, non-spinning binary system, considering directly the case of generic eccentric orbits. They computed the formulas for the energy and angular momentum loss due to GW emission, showing that these losses lead to the shrinking of the binary separation and circularization of the orbit over time. Most importantly, they demonstrated that considering astrophysical compact objects, gravitational emission could lead to the merger of the binary [16]. This dissipative effect, appearing at 2.5PN order and thoroughly discussed in Chap. 4, provided one of the first observationally testable predictions of GR in the dynamical regime. In the same period, Schiff (1960), building on the works of Refs. [13, 14], derived the evolution of a gyroscope (i.e., a test particle) orbiting a more massive spinning body (Earth), obtaining the relativistic spin precession arising from spin–orbit and spin–spin couplings, demonstrating that these effects appear at 1.5PN and 2PN orders. This work prompted other groups to extend these findings to comparable-mass systems. In the 1970s, this effort was undertaken through a variety of approaches, ranging from quantum field theory [18, 19] to classical gravity (see, e.g., Ref. [11]). Some of which already provide evolution equations for the spins, i.e., spin-precession equations, for two-body systems evolving on eccentric orbits [19].

In 1974, 60 years after the introduction of GR and 40 years after the advent of the PN expansion, the observation of binary pulsar PSR 1913+16 by Hulse and Taylor (1975) finally allowed these theoretical predictions to be tested for the first time. This system was the first observed to be formed by a spinning NS and a compact object, likely another NS, thus representing a perfect relativistic, comparable-mass two-body system. Moreover, by analyzing the times of arrival of the pulsar's radio emission, the orbital properties of the binary were determined, revealing that the system's bodies were moving on eccentric orbits with a measured eccentricity of ≈ 0.67. After a few

years of observation, some of the predicted relativistic effects were confirmed, specifically the emission of gravitational radiation with consequent decay of orbital separation and eccentricity and precession of the pulsar spin [21]. The observation campaign of PSR 1913+16 provided a strong impetus for the development of a more accurate equation of motion for comparable-mass, spinning systems. By the 1980s, even if in a still incomplete form, spin-precession equations were known up to the 2PN order for both BH [22, 23] and generic compact binaries [24].

Nevertheless, it was necessary to wait another 15 years to combine the contributions of spin-orbit and spin-spin coupling with the effects of gravitational radiation. By the 1990s, indirect proofs of the existence of GWs were established [25], as evidenced by the Nobel Prize awarded to Russell Hulse and Joseph Taylor [26], and the LIGO detectors for GWs were under construction [27]. Consequently, the focus evolved from finding the equation of motion to calculating the first waveforms and phases of GWs. Assuming balance between energy radiated and orbital energy lost, Kidder *et al.* (1993), were the first to determine the spin effects on the evolution of GW frequency and orbital separation. In particular, they predict the modulation of waveforms caused by the spin-induced precession of the orbital plane. A year later, the findings of Kidder *et al.* (1993) were confirmed and expanded by Refs. [29, 30] . Apostolatos *et al.* (1994) in particular, studied the spin evolution during the GW-driven inspiral of binary systems, introducing both a visual representation of spin precession and a classification of its different "flavors". Collectively, these studies laid the groundwork for the modern treatment of spin effects in GW data analysis.

However, all these works were still incomplete; even if aware of its existence, they all assumed that the spin-induced quadrupole moment was negligible. This effect, studied in the context of GWs by Poisson (1998), enters in the equation of motion at the 2PN

order and is related to the rotation-induced distortion of the mass distribution (the body becomes oblate) and the consequent distortion of the gravitational field outside the body. It needed to wait until 2008 to be introduced in the spin precession equation thanks to the work of Racine (2008). In this work, the author demonstrates that the complete, up to 2PN, spin-precession equations permit the existence of a new constant of motion, $\chi_{\rm eff}$, which now plays a central role in GW data analysis, being the best measurable spin-related quantity [33]. Therefore, after the work of Racine (2008), complete spin-precession equations up to 2PN order were finally known, but they were limited to the special case of circular orbits. Always in this limit, in subsequent years, studies on the phenomenology of spin precession and the dynamics of spinning BH systems were conducted, particularly in Refs. [34, 35].

In 2015, the GW signal from the merger of two BHs was finally detected [36]. Similar to observations of the binary pulsar PSR 1913+16, this detection, together with the growing number of subsequent observations, provided a direct test of the equations of motion derived over the past century following the introduction of GR, including predictions concerning the effects of spin on the dynamics of comparable-mass two-body systems (see, e.g., Refs. [37, 38, 39, 5]). Over the past decade, these observations have driven further progress in understanding spin effects. Of particular importance for this thesis are the works of Gerosa *et al.* (2015) and Gerosa *et al.* (2023). The formalism introduced in those works, limited to the treatment of quasi-circular binaries, is especially relevant for studying the dynamics of spinning two-body systems: it introduced the concepts of precession averaging and a multi-timescale approach to dynamics, providing an efficient computational framework for modeling spin precession in BH binaries and enabling an unprecedented exploration of their phenomenology.

But what about eccentricity? Eccentricity was reconsidered in combination with

spin[1] by Klein *et al.* (2018) and Klein (2021). These works, however, did not fully explore the phenomenology of such more complete, and arguably more realistic (see Sec. 1.2), systems. Building partially on these results and on earlier studies, Phukon *et al.* (2019) attempted this task, albeit in a limited manner, as it did not employ the multitimescale approach of Ref. [35]. As just underlined above, eccentricity was an element that needed to be *reintroduced* in the treatment of spin effects. Even if it began earlier, the development of equations of motion and the study of the impact of eccentricity on gravitational emission proceeded in parallel with those related to the spins, without intersecting for many years. Although eccentricity is an intrinsic element of the dynamics, influencing it more than the spins, it has been neglected in the later development of spin-precession equations [29]. In fact, it was already understood that GW detectors would mainly observe the final inspiral [44], where binaries, even if initially highly eccentric, are expected to have nearly circularized [16]. The early works of Peters and Mathews (1963) and Peters (1964) already testify the central role of eccentricity in the dynamics of the two-body problem. Yet, unlike spin effects, whose development followed a relatively direct trajectory, the treatment of eccentricity evolved through a more subtle and, at times, controversial history. Chap. 4 is entirely dedicated to tracing these developments in detail.

In the spirit of this section, it is worth mentioning, already at this point of the thesis, some key advances in the eccentric two-body problem after those of the 1960s. The first important contribution is that of Damour and Deruelle (1985), who developed the quasi-Keplerian formalism, in which orbital parameters are expanded beyond their Keplerian definition, enabling the formulation of eccentric equations of motion up to high PN orders. This was followed by that of Lincoln and Will (1990), who derived

[1] It is worth noting that eccentricity had already been included in early studies of spin precession for comparable-mass BH binaries, e.g., Ref. [18], and later in Ref. [32].

Lagrangian planetary or osculating equations and introduced a multi-timescale method to describe the evolution of eccentric systems under GW emission. In subsequent years, efforts were directed both toward extending these calculations to increasingly higher PN orders (see, e.g., Refs. [46, 47, 48, 49]) and toward clarifying the definition of eccentricity in GR (see, e.g., Refs. [50, 51]), both of which remain active areas of research today. As with spins, the observation of binary pulsars PSR 1913+16 and the detection of GW events have significantly contributed to testing theoretical predictions about eccentricity. However, eccentricity remains a challenging parameter to measure, especially given the limited sensitivity of GW detectors at low frequencies that does not allow for observation of early inspiral where eccentricity might still be large enough to be measured [52], and the issues related to the detection and analysis of potentially eccentric signals, as reviewed in Refs. [53, 54]. After 10 years of collecting GW data, some evidence is now emerging regarding possible eccentric events [55, 56, 57]. Nevertheless, as already noted in Ref. [16], binaries spend the majority of their inspiral at orbital separations comparable to their initial values. This implies that, although systems circularize by the time they merge, a significant fraction of their evolution, and thus most of the spin precession if present, takes place while the orbit is still eccentric. For this specific reason, it is worthwhile to study and explore the interplay between spin evolution and eccentricity, which is the primary goal of this thesis.

1.2 Spin-precession and eccentricity: Why care? Why together?

> *"Non-rotating bodies are about as rare as a relativist at a biophysics convention"*
>
> *–Poisson and Will (2014)*

There are two short answers to both questions: *astrophysics* and *fundamental physics*.

The long answers go as follows. As pointed out in the previous section, the detection of GWs is revolutionizing our understanding of binary systems composed of compact objects, such as BHs and NSs. Specifically, they provide information, usually inaccessible by other means, about the masses, spins, and internal structure of such objects. So far, almost 220 GW signals from compact binaries have been recorded [58], a number that is expected to grow further with the ongoing observing run [59]. As a result, we are becoming more confident in describing compact objects, especially BHs; however, as recently shown, there is still room for surprises [60, 61]. This demonstrates that our understanding, particularly from an astrophysical perspective, remains incomplete. One major gap concerns the formation of the observed binary systems: pairing two compact objects that can merge within a Hubble time is higly non-trivial and requires synergy between astrophysics and GR [62, 63, 64, 65, 66, 67]. However, key observed parameters, such as masses, spin magnitudes and orientations, and orbital eccentricity, can be used to address this problem [68, 67, 69, 70, 71]. For instance, large BH masses suggest hierarchical mergers in dense environments [63, 72]; BHs with spins aligned with their orbital angular momentum likely arise from the evolution of isolated field binaries [69, 73], while eccentric mergers are expected from binaries assembled via

recent dynamical interactions [70, 74, 71], notably including Kozai-Lidov oscillations in triple systems [75]. For supermassive BH binaries, eccentricity and spins both encode information on the pairing and hardening processes that lead to the formation of such systems following galaxy mergers [76].

We *care* about spin precession [77, 78, 79, 80, 69, 81, 73, 82] and eccentricity [83, 70, 71] since they are arguebly the most promising indicators of the BH progenitors and their formation mechanisms. Moreover, in the simplified picture of two formation scenarios—the isolated and the dynamical channels— spin precession and eccentricity are correlated, with the former scenario predicting minimal to no spin precession and circular orbits, while the latter can lead to binaries with significant spin misalignments and large eccentricities [83, 70, 71]. As shown in Ref. [84], we expect that a significant fraction of the observed binaries originates from the dynamical formation scenario, forcing us to consider, in modeling the evolution of GW sources, spin precession and eccentricity *together*.

Chapter 2 of this thesis is entirely devoted to this problem, even though, as in Chap. 4, the focus is not primarily on astrophysical considerations. We *care* about spin precession and eccentricity and their evolution *together* in the two-body problem, also because they constitute a fascinating and fundamental theoretical challenge. This motivation is as strong and vital as the astrophysical one and, as often occurs in the development of GR, is not always the initial driving force. The pursuit of fundamental physical understanding is indeed a key motivation underlying the works presented in Chaps. 2 and 4.

In the former, we report the work done in [85], where, starting from the spin-precession equations generalized to eccentric orbits, we explore the dynamics of these systems employing the multi-timescale approach proposed by [40], focusing in particular

on understanding the evolution of spin direction in non-circular orbits. These systems are expected to produce peculiar GW signals since both spin precession and orbital eccentricity are predicted to leave distinct imprints on the GW waveform (see Ref. [53] and references therein). Specifically, spin-induced precession modulates the orientation of the orbital plane, resulting in variations in the observed amplitude and phase of the waveform. Likewise, in eccentric binaries, the GW emission is asymmetric between apocenter and pericenter, introducing additional changes. However, to date, no complete waveform model exists that describe the full inspiral–merger–ringdown of eccentric, precessing binaries, preventing the secure and direct detection of these sources. Only the inspiral phase has been modeled by a few groups [42, 86], with complementary efforts in numerical relativity [87, 88, 89]. In the circular case, spin-precession equations and the use of precession averaging are already incorporated into waveform models [90, 91]; for eccentric binaries, similar approaches will be required, further motivating the work presented in Chap. 2.

Although, once observed, spin orientations and eccentricity provide valuable insights into the formation mechanisms, they are not constants in the relativistic two-body problem. As a result, the values of these parameters, as measured via GWs, will not directly reflect their values at formation, which is the point in binaries' evolution that we are particularly interested in. Here, a detailed understanding of the dynamics of precessing and eccentric systems is once again crucial. In Fumagalli *et al.* (2024), which is reported in Chap. 3, we show that the formalism of Chap. 2 can be used to accurately connect observed parameters to their initial conditions, where astrophysically meaningful information can be extracted. Explicitly, we show the considerable influence that eccentricity can have on the evolution of the spin, and how problematic this is for the inference of formation channels.

The treatment of spin-precessing and eccentric binaries that we propose in Chap. 2 is based, as already underlined, on a multi-timescale approach, which requires that the timescales at play in the two-body problem under study are always well-separated [40]. For circular binaries, this is always true within the regime of validity of the PN approximation. However, this is no longer the case for eccentric systems, where the timescale hierarchy strongly depends on how the evolution of eccentricity is modeled [93]. In the works presented in Chap. 2, we considered the evolution equations for eccentricity proposed by Peters (1964). These equations, which are averaged over the orbital period, are widely used by the GW community even though they are known to be ill-defined for parabolic and hyperbolic orbits. In those regimes, the orbital timescale becomes longer than the timescale on which GW emission changes the binary. As also exposed in Chap. 3, to gain astrophysically significant insight into the formation of binary systems, we need to push backwards in time the measured spin parameters, reaching or getting very close to those problematic regimes. This issue led us to the work described in Chap. 4, where we explore a new way to describe the dynamics of eccentric-only binaries capable of working also in the theoretically expected and astrophysically meaningful parabolic and hyperbolic limits. This provides us with a tool to test unambiguously the region of parameter space where the timescale hierarchy is maintained, and thus where the formalism introduced in Chap. 2 can be applied to treat spin precession and eccentric BH binaries.

1.3 Setting the stage

> *"What diabolically clever physics would ever foist on man a theory with such a complicated geometric foundation as Newtonian theory?"*
>
> –*Misner* et al. *(1973)*

In the previous section, spin precession and eccentricity have been mentioned a lot of times, along with terms such as eccentric orbits, spin-orbit coupling, and spin-spin coupling, as well as concepts like orbital and precession averages. What do we mean by those? This section is dedicated to introducing the geometrical setting that all the original works of this thesis share, clarifying what we mean by eccentric orbits, introducing the orbital parameter later used in Chap. 4, and briefly reviewing the formalism of Gerosa *et al.* (2023), explaining what we mean by spin precession. In this section, we adopt geometric units setting $G = c = 1$.

In this thesis, any time we consider a two-body system, we suppose it to be formed by point particles of mass m_1 and m_2 where $m_2 \leq m_1$ such that the total mass of the system is given by $M = m_1 + m_2$, the mass ratio by $q = m_2/m_1 \leq 1$, the reduced mass by $\mu = (m_1 m_2)/M$ and the symmetric mass ratio by $\eta = \mu/M$.

The most generic bound orbits in Kepler's two-body problem are ellipses, which are parametrized by their eccentricity $0 \leq e < 1$. In GR, point particles represent compact objects [95, 96], which, if not stated otherwise, we will consider as BHs, and, at least in the PN approximation, the underlying timescale separation implies that orbits can still be treated using conic sections [16]. Therefore, in this thesis, we always keep the Keplerian description of the systems as a reference. Specifically, we consider the scenario sketch on the left side of Fig. 1.1, where, working in the center-of-mass frame, eccentric binaries reduce to an effective system where a single particle of mass μ orbits around a

fixed mass M located in one of the foci of the ellipse. Describing the orbital elements of such an effective system requires the introduction of two planes: the invariant plane and the orbital plane [9]. The geometry of the orbit in the orbital plane is mainly described by the semi-major axis a, the semi-latus rectum $p = a(1-e^2)$, the distance at pericenter $a(1-e)$, the true anomaly f, which is measured counterclockwise from the direction of the pericenter to the orbital separation vector $\boldsymbol{r}$ and can be interpreted as the angular position of the lighter body along the orbit, and finally by the longitude of pericenter ω which is defined as the angle between the line of nodes and the direction of the pericenter, and is informative of the pericenter advance. In the purely Newtonian limit, the lighter body experiences a central acceleration described by Eq. (1.1) truncated at $\mathcal{O}(\epsilon^0)$, and the binding energy and orbital angular momentum of the system can be defined as

$$E = \frac{1}{2}\mu v^2 - \frac{\mu M}{r}, \tag{1.2}$$

$$\boldsymbol{L} = \mu \boldsymbol{r} \times \boldsymbol{v}, \tag{1.3}$$

where $\boldsymbol{v}$ is the relative velocity vector of the bodies. Considering the radial and azimuthal coordinates r and ϕ, we can define a basis formed by the vectors $\boldsymbol{n} = [\cos\phi, \sin\phi, 0]$, already introduced with Eq. (1.1), $\boldsymbol{\lambda} = [-\sin\phi, \cos\phi, 0]$, and $\boldsymbol{e}_z = [0, 0, 1]$, which is normal to the orbital plane and parallel to $\boldsymbol{L}$ (See Ref. [9] for a more detailed description of reference frames for this problem). With this basis, we can define

$$\boldsymbol{r} = r\boldsymbol{n}, \tag{1.4}$$

$$\boldsymbol{v} = \dot{r}\boldsymbol{n} + r\dot{\phi}\boldsymbol{\lambda}, \tag{1.5}$$

$$\boldsymbol{a} = \left(\ddot{r} - r\dot{\phi}^2\right)\boldsymbol{n} + \left(2\dot{r}\dot{\phi} + r\ddot{\phi}\right)\boldsymbol{\lambda}. \tag{1.6}$$

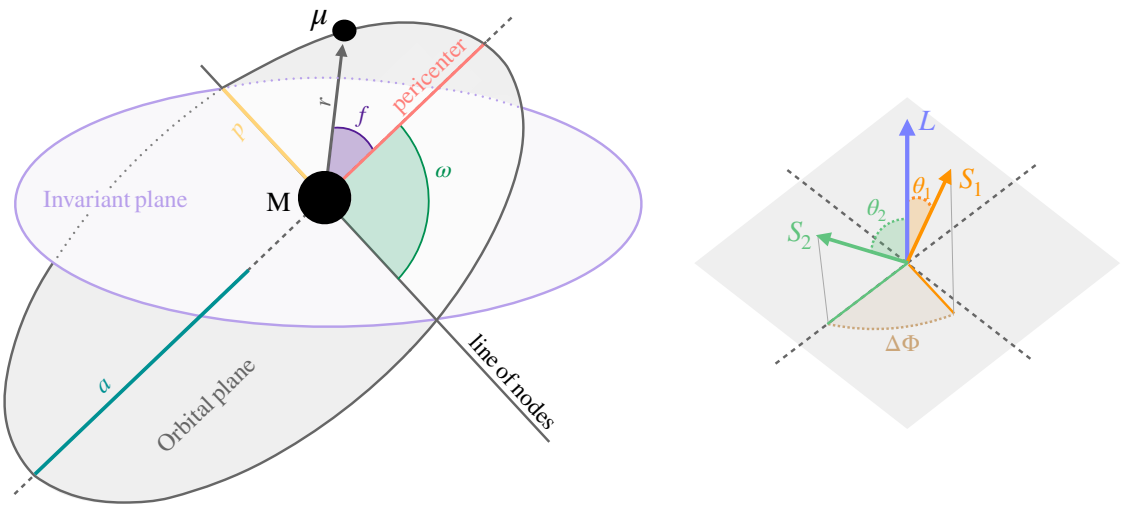

Figure 1.1: In the PN approximation, binaries on elliptic orbits can be simplified to an effective system with a fixed mass M orbited by a body of mass μ (black circles), as shown in the sketch on the left. The orbital elements are defined within the orbital plane (grey), including the longitude of the pericenter ω, which must be defined relative to an invariant plane (purple), specifically with respect to its intersection with the orbital plane, known as the line of nodes. The true anomaly f (green) measures the angle between the pericenter (red) and the separation vector $\boldsymbol{r}$. A key element for analyzing the eccentric system, especially in Chap. 4, is the semi-latus rectum, highlighted in yellow. On the right, the orbital angular momentum vectors $\boldsymbol{L}$ and the spins of the two bodies, $\boldsymbol{S}_1$, $\boldsymbol{S}_2$ are displayed, along with the relevant angles for treatment of spin precession.

The Newtonian conservation of energy and angular momentum relates the terms appearing in Eqs. (1.4), (1.5), and (1.6) to the orbital elements characterizing the binary

$$r = \frac{p}{1 + e\cos f}, \tag{1.7}$$

$$\dot{r} = \sqrt{\frac{M}{p}} e \sin f, \tag{1.8}$$

$$\dot{\phi} = \sqrt{\frac{M}{p^3}} \left[1 + e \cos f\right]^2, \tag{1.9}$$

$$v = \sqrt{\frac{M}{p} (1 + 2e \cos f + e^2)}. \tag{1.10}$$

Using such definitions, the magnitude of energy and orbital angular momentum reads as

$$|E| = \frac{q\, M^2}{(1+q)^2} \frac{(1-e^2)}{2\, p}, \tag{1.11}$$

$$L = \frac{q\, M^2}{(1+q)^2} \sqrt{\frac{p}{M}}\,. \tag{1.12}$$

Throughout this thesis, we will consistently refer to the eccentricity and semi-major axis in accordance with their Keplerian definitions. We will treat the orbital elements introduced in the right-hand side of Eqs. (1.7)-(1.10) as constants while neglecting the emission of GWs. Chapter 4 is entirely devoted to how these parameters change when GWs can no longer be ignored.

Finally, we define the orbital period or orbital timescale as

$$\tau_{\rm orb} = \frac{2\pi}{\sqrt{M}} \left(\frac{p}{1-e^2}\right)^{3/2}, \tag{1.13}$$

and the orbit-averaging operation, for a generic quantity X, as

$$\langle X \rangle = \frac{1}{\tau_{\rm orb}} \int_0^{\tau_{\rm orb}} X(t) {\rm d}t. \tag{1.14}$$

Now that we have explained how two bodies are placed on an eccentric orbit, we

make them spin. The framework we consider is the one sketch on the right of Fig. 1.1. The spins of the bodies are identified by vectors $\boldsymbol{S}_1$ and $\boldsymbol{S}_2$, where the former is assigned to the more massive body and the latter to the lighter one. The magnitudes of the spins $S_{1,2} = |\boldsymbol{S}_{1,2}|$ are defined in terms of the dimensionless Kerr parameters $\chi_{1,2} = S_{1,2}/m_{1,2}^2 \in [0,1]$ and explicitely expresed as

$$S_1 = \frac{\chi_1}{(1+q)^2} M^2 \,, \tag{1.15}$$

$$S_2 = \frac{q^2 \chi_2}{(1+q)^2} M^2 \,. \tag{1.16}$$

We describe the spin orientations using the polar angles $\theta_{1,2} \in [0,\pi]$ between each of the spin vectors and the angular momentum and the azimuthal angle $\Delta\Phi \in [-\pi,\pi]$ between the projections of the two spins onto the orbital plane (see Fig. 1.1). Explicitly, their cosine are defined as

$$\cos\theta_1 = \hat{\boldsymbol{S}}_1 \cdot \hat{\boldsymbol{L}}, \tag{1.17}$$

$$\cos\theta_2 = \hat{\boldsymbol{S}}_2 \cdot \hat{\boldsymbol{L}}, \tag{1.18}$$

$$\cos\Delta\Phi = \frac{\hat{\boldsymbol{S}}_1 \times \hat{\boldsymbol{L}}}{|\hat{\boldsymbol{S}}_1 \times \hat{\boldsymbol{L}}|} \cdot \frac{\hat{\boldsymbol{S}}_2 \times \hat{\boldsymbol{L}}}{|\hat{\boldsymbol{S}}_2 \times \hat{\boldsymbol{L}}|}, \tag{1.19}$$

$$\operatorname{sgn}\Delta\Phi = \operatorname{sgn}(\boldsymbol{L} \cdot [(\boldsymbol{S}_1 \times \boldsymbol{L}) \times (\boldsymbol{S}_2 \times \boldsymbol{L})]) \,, \tag{1.20}$$

where $\hat{\boldsymbol{L}} = \boldsymbol{L}/L$, $\hat{\boldsymbol{S}}_{1,2} = \boldsymbol{S}_{1,2}/S_{1,2}$ and sgn is a function extracting the sign of the quantity at which is applied. These quantities can be used to construct the effective spin [97]

$$\chi_{\rm eff} = \frac{\chi_1 \cos\theta_1 + q\chi_2 \cos\theta_2}{1+q}, \tag{1.21}$$

and the weighted spin difference [42]

$$\delta\chi = \frac{\chi_1 \cos\theta_1 - q\chi_2 \cos\theta_2}{1+q}, \tag{1.22}$$

which will allow us to greatly simplify the treatment of spin evolution [40].

The spin of the bodies, along with the orbital angular momentum vector, defines the total angular momentum $\boldsymbol{J} = \boldsymbol{L} + \boldsymbol{S}_1 + \boldsymbol{S}_2$. [2] When considered in a general relativistic framework, but ignoring GW emission, the spins are involved in three main effects: (*i*) they couple with the orbital angular momentum vector, (*ii*) they couple among themself, and (*iii*) they induce a quadrupole moment. Spin–orbit coupling (*i*) includes both geodetic precession, which is the influence on the spin vector transport in the curved spacetime caused by the companion's mass, and the Lense–Thirring effect, which relates to frame dragging caused by the companion's spin and acts on both the orbital angular momentum and spin vectors. These effects, as spoiled in Sec. 1.1, appear at 1.5PN order. Spin–spin coupling (*ii*), on the other hand, arises at 2PN order and corresponds to the direct dipole–dipole interaction between the two spins, similar to a magnetic dipole interaction in electromagnetism [9]. At the same PN order, the effect caused by the spin-induced monopole-quadrupole interaction (*iii*) appears; in this case, the bodies, while rotating, deform their own mass distribution, which then alters the gravitational fields outside them [31, 32].

Considered altogether, these effects cause a time evolution of the directions of the spin and orbital angular momentum vectors. Specifically, these vectors precess about the direction of $\boldsymbol{J}$ and nutate, leading to a complex phenomenology [29]. This applies both in the eccentric and circular regimes. In this section, we treat the circular limit

[2] Throughout this thesis, we will always consider $\boldsymbol{J} = \boldsymbol{L}_N + \boldsymbol{S}_1 + \boldsymbol{S}_2$, with $\boldsymbol{L}_N$ defined as in Eq. (1.3) consistently with Ref [98].

and present its eccentric counterpart in Chap. 2.

The formal derivation of the evolution equation for the spin vectors is lengthy and goes beyond the scope of this thesis (see Refs. [9] and [94] for a complete derivation). However, following Kidder (1995), it can be shown quite simply that the time evolution of the spins directly results in the time evolution of the orbital angular momentum vector. In fact, if we only consider the conservative dynamics, $\boldsymbol{J}$ is conserved, which means that

$$\frac{\mathrm{d}\boldsymbol{L}}{\mathrm{d}t} = -\frac{\mathrm{d}\boldsymbol{S}}{\mathrm{d}t}, \tag{1.23}$$

and, therefore, if the spins precess, $\boldsymbol{L}$ must also do so. Additionally, since the orbital angular momentum is, by definition, always perpendicular to the orbital plane, its precession causes the orbital plane itself to precess. Finally, the complete set of spin-precession equations results in [32]

$$\frac{\mathrm{d}\boldsymbol{S}_1}{\mathrm{d}t} = \frac{1}{2r^3}\left\{(4+3q)\,\boldsymbol{L} + 3q\left[\hat{\boldsymbol{r}}\cdot\left(\boldsymbol{S}_1 + \frac{\boldsymbol{S}_2}{q}\right)\right]\hat{\boldsymbol{r}} - \boldsymbol{S}_2\right\}\times\boldsymbol{S}_1, \tag{1.24}$$

$$\frac{\mathrm{d}\boldsymbol{S}_2}{\mathrm{d}t} = \frac{1}{2r^3}\left\{\left(4+\frac{3}{q}\right)\boldsymbol{L} + 3\left[\hat{\boldsymbol{r}}\cdot\left(\boldsymbol{S}_1 + \frac{\boldsymbol{S}_2}{q}\right)\right]\hat{\boldsymbol{r}} - \boldsymbol{S}_1\right\}\times\boldsymbol{S}_2, \tag{1.25}$$

$$\frac{\mathrm{d}\boldsymbol{L}}{\mathrm{d}t} = \frac{1}{2r^3}\left\{\left[(4+3q)\,\boldsymbol{S}_1 + \left(4+\tfrac{3}{q}\right)\boldsymbol{S}_2\right]\times\boldsymbol{L} + 6q\left[\hat{\boldsymbol{r}}\cdot\left(\boldsymbol{S}_1 + \tfrac{\boldsymbol{S}_2}{q}\right)\right]\left[\hat{\boldsymbol{r}}\times\left(\boldsymbol{S}_1 + \tfrac{\boldsymbol{S}_2}{q}\right)\right]\right\}, \tag{1.26}$$

where $\hat{\boldsymbol{r}} = \boldsymbol{r}/r$. From these equations, it is possible to extract an order of magnitude estimate of the precession timescale (see Chap. 2 for more details)

$$\tau_{\mathrm{prec}} = \frac{S}{\mathrm{d}\boldsymbol{S}/\mathrm{d}t} \propto \frac{r^3}{L} \propto r^{5/2}, \tag{1.27}$$

while the orbital timescale, as defined in Eq. (1.13), results to be $\tau_{\mathrm{orb}} \propto r^{3/2}$. This

means that the evolution of spin and orbital angular momentum directions occurs over many orbits, implying that the spin dynamics can be consistently orbit-averaged. When such an operation is carried out (see Eq. (1.14) and Appendix of Ref. [98]) and the spin parameters defined in Eqs. (1.21), and (1.22) are used, we obtain the following spin-precession equations [40]

$$\left\langle \frac{\mathrm{d}\boldsymbol{S}_1}{\mathrm{d}t} \right\rangle = \boldsymbol{\omega}_1 \times \boldsymbol{S}_1, \tag{1.28}$$

$$\left\langle \frac{\mathrm{d}\boldsymbol{S}_2}{\mathrm{d}t} \right\rangle = \boldsymbol{\omega}_2 \times \boldsymbol{S}_2, \tag{1.29}$$

$$\left\langle \frac{\mathrm{d}\boldsymbol{L}}{\mathrm{d}t} \right\rangle = \boldsymbol{\omega}_\mathrm{L} \times \boldsymbol{L}, \tag{1.30}$$

where, $\langle\cdot\rangle$ denotes the orbit-averaging operation and

$$\boldsymbol{\omega}_1 = \frac{1}{2r^3}\left\{\left[4+3q-\frac{3(1+q)\chi_\mathrm{eff}}{\sqrt{r/M}}\right]\boldsymbol{L}+\boldsymbol{S}_2\right\}, \tag{1.31}$$

$$\boldsymbol{\omega}_2 = \frac{1}{2r^3}\left\{\left[4+\frac{3}{q}-\frac{3(1+q)\chi_\mathrm{eff}}{q\sqrt{r/M}}\right]\boldsymbol{L}+\boldsymbol{S}_1\right\}, \tag{1.32}$$

$$\boldsymbol{\omega}_L = \frac{1}{2r^3}\left\{\left[4+3q-\frac{3(1+q)\chi_\mathrm{eff}}{\sqrt{r/M}}\right]\boldsymbol{S}_1+\left[4+\frac{3}{q}-\frac{3(1+q)\chi_\mathrm{eff}}{q\sqrt{r/M}}\right]\boldsymbol{S}_2\right\}. \tag{1.33}$$

Neglecting radiation reaction and exploiting the conservation of χ_eff, one can reduce Eqs. (1.24)–(1.33) to a single differential equation for the weighted spin difference [40]

$$M\frac{\mathrm{d}\delta\chi}{\mathrm{d}t} = \frac{3q}{(1+q)^2}\chi_1\chi_2\left(\frac{r}{M}\right)^{-3}\left[1-\frac{\chi_\mathrm{eff}}{\sqrt{r/M}}\right]\sin\theta_1\sin\theta_2\sin\Delta\Phi\,, \tag{1.34}$$

where the angles θ_1, θ_2, and $\Delta\Phi$ depend on $\delta\chi$. The solution is quasi-periodic, with $\delta\chi$ oscillating between two extrema $\delta\chi_\pm$ which are themselves functions of r, q, χ_1, χ_2, χ_eff, and J. In turn, these are used to define the spin precession period (i.e. S is substituted

by $\delta\chi$, see Eq. (1.27))

$$\tau_{\rm pre} = 2\int_{\delta\chi_-}^{\delta\chi_+}\left(\frac{{\rm d}\delta\chi}{{\rm d}t}\right)^{-1}{\rm d}\delta\chi\,, \tag{1.35}$$

which can be expressed in closed form using elliptic integrals [40]. The argument of dynamics spreading over different timescales can be extended further when the GW emission is reintroduced. Gravitational radiation affects the orbits over a timescale $\tau_{\rm rr} \propto r^4$ [16]. Since this is much larger than $\tau_{\rm prec}$, it is possible to proceed as before and introduce another average now over the precession cycles. In fact, the angular momentum vectors complete many precessional cycles before GW emission effectively reduces the binary's orbital separation. The operation of precession averaging, similar to that introduced with Eq. (1.14), for a generic quantity Y is given by

$$\langle Y\rangle = \frac{\displaystyle\int_{\delta\chi_-}^{\delta\chi_+} Y(\delta\chi)\left(\frac{{\rm d}\delta\chi}{{\rm d}t}\right)^{-1}{\rm d}\delta\chi}{\displaystyle\int_{\delta\chi_-}^{\delta\chi_+}\left(\frac{{\rm d}\delta\chi}{{\rm d}t}\right)^{-1}{\rm d}\delta\chi}\,, \tag{1.36}$$

This idea, initially proposed by Gerosa *et al.* (2015) and further refined by Gerosa *et al.* (2023), enables us to handle the problem efficiently. Once double-averaged, the dynamics only need to be integrated over the radiation reaction timescale, allowing for larger integration steps. With spin-precession equations in hand and the eccentric scenario fully defined, we are ready to raise the curtain on the next chapter, where these two elements are brought together.

1.4 Researh overview

> *"It is often said that it takes a 2σ result to convince a theorist that his theory is correct, a 5σ result to convince an observer that an effect is real, and a 10σ result to convince a theorist that his theory is wrong"*
>
> –*Ivezić* et al. *(2020)*

All the work presented in this thesis has been published in peer-reviewed international journals. In the cited and presented studies, the order of authorship reflects each researcher's relative contribution. I have led all publications where I am the first author, including those that form the basis of this thesis. The main contributions are summarized below.

- Chapter 1 reviews the two-body problem in post-Newtonian theory and the astrophysical and geometrical contexts central to the works presented in the remaining chapters. It does not include material I have previously published in this form.

- Chapter 2 is based on the works Fumagalli and Gerosa (2023) and Fumagalli *et al.* (2025), both conducted in close collaboration with Davide Georsa and, for the latter, with Nicholas Loutrel, who assist us with eccentric PN-complete orbit-averaged equations. Both the theoretical and computational frameworks presented are extensions of the previous work of Gerosa *et al.* (2023). For that publication, I contributed as a second author by reviewing the theoretical formalism and its derivation, as well as testing the code. The code presented in Fumagalli *et al.* (2025) was also tested in collaboration with a bachelor student, William Toscani, by verifying that it correctly reproduces the well-known [35] property of circular spin-precessing BH binaries: "isotropic stays isotropic", which

states that if a population of BH binaries is initialized with spin orientations isotropically distributed, such isotropy is preserved throughout the inspiral. We then investigated whether this property also holds when considering eccentric binaries, finding that isotropy remains conserved in this more general configuration as well. Finally, Sec. 2.6 contains preliminary work done in collaboration with a master student, Simone Restuccia, and Davide Gerosa, and will soon be published.

- Chapter 3 is based on the works Fumagalli *et al.* (2024). I started this work during a three-month visit to the Department of Applied Math and Theoretical Physics at the University of Cambridge, and I carried it out in close collaboration with Isobel Romero-Shaw and Davide Gerosa, who contributed to developing the astrophysical case and provided insight into the interesting data to consider. For this work, Viola De Rensiz provided the simulated events [101] and assistance with their analysis. Konstantinos Kritos and Aleksandra Olejak provided the output of their population synthesis codes, Rapster [102] and StarTrack [103]. We used these to build the histograms presented in Figure 3 of the paper.

- Chapter 4 is based on the works Fumagalli *et al.* (2025).The formalism presented has been developed together with Nicholas Loutrel. Davide Gerosa and Matteo Boschini assist in its advancement.

- Chapter 5 summarizes the results of the work presented in previous chapters and briefly discusses possible future developments. It does not include material I have previously published in this form.

Besides the work presented explicitly in this thesis, I also contributed to the works of Boschini *et al.* (2025), assisting in the interpretation of the results, of Stegmann *et al.* (2025), for which I directly produced Appendix B and Fig. 7 and of Gerosa *et al.*

(2025), for which I review the analytical findings. Finally, I led the work Fumagalli *et al.* (2025) on analyzing Pulsar Timing Arrays signals as part of my master's thesis.

Along with those already mentioned, two other bachelor students worked under my supervision and that of Davide Gerosa: Leonardo Toti, who studied BHs merger trees and runaway collisions in dense clusters, and Marco Bianchi, who tested a machine learning approach to compute the averaged precession parameter $\chi_{\rm p}$ of BH binaries.

During my Ph.D., I served twice as a teaching assistant for the Laboratory of Machine Learning for Physics and Astronomy course. I contributed to organizing the biennial conference of the Italian Society of General Relativity and Gravitation (XXVI SIGRAV Conference on General Relativity and Gravitation). In particular, I helped coordinate a session on gender and precarious careers in academia, a topic that has been especially important to me throughout my doctoral studies. Together with Alessia Franchini, Irene Ferranti, Cecilia Fabbri, and Elisa Bortolas, and in collaboration with a research group from the Department of Human Sciences, I organized several sessions and activities focused on gender issues in academia within the Astrophysics section of the University of Milano-Bicocca.

Finally, I participated in various outreach activities, including the European Researcher Night [107] and several events with high school students, where I gave introductory lectures on gravitational-wave astronomy.

Chapter 2

Spin-eccentricity interplay in merging binary black holes

Abstract

Orbital eccentricity and spin precession are precious observables to infer the formation history of binary black holes with gravitational-wave data. We present a post-Newtonian, multi-timescale analysis of the binary dynamics, which is able to capture both precession and eccentricity over long inspirals. We show that the evolution of an eccentric binary can be reduced to that of an effective source on quasi-circular orbits, coupled to a post-Newtonian prescription for the secular evolution of the eccentricity. Our findings unveil an interplay between precession and eccentricity: the spins of eccentric binaries precess on shorter timescales and their nutation amplitude is altered compared to black holes on quasi-circular orbits, consequently affecting the so-called spin morphology.

Even if binaries circularize by the time they enter the sensitivity window of our detectors, their spin orientations retain some memory of the past evolution on eccentric orbits, thus providing a new link between gravitational-wave detection and astrophysical formation. At the same time, we point out that residual eccentricity should be considered a source of systematics when reconstructing the past history of black-hole binaries using the spin orientations.

Summary

In this chapter, we developed a PN formalism to describe binaries that are both eccentric and subject to spin precession (Sec. 2.2). We then applied this framework to investigate the robustness of the underlying timescale hierarchy and to assess the impact of eccentricity on the evolution of precessing black-hole binaries (Sec. 2.3). Our analysis highlights how eccentricity modifies spin dynamics, with observable consequences for quantities such as tilt angles and spin morphologies. These results indicate that the interplay between spin precession and eccentricity provides a new phenomenological window into the past evolution of black-hole binaries (Sec. 2.5). At the same time, neglecting residual eccentricity can introduce significant systematic biases in astrophysical inference, motivating the dedicated study presented in Chap. 3. Throughout this chapter, we adopt natural units with $G = c = 1$.

The material presented in this chapter is based on the work published in Fumagalli and Gerosa (2023) and Fumagalli *et al.* (2025). The material in Sec. 2.6 is preliminary and originates from research conducted by the author that has not yet been published, but is intended for future publication.

2.1 Introduction

As discussed in Sec. 1.2, jointly considering spin precession and eccentricity is astrophysically well motivated. The relativistic two-body problem exhibits distinctive dynamical features associated with BH spins and orbital eccentricity. In binaries where the component spins are misaligned with the orbital angular momentum, the orbital plane undergoes precession around the total angular momentum, continuously varying its orientation (see Sec. 1.3). Meanwhile, orbital eccentricity decreases during the inspiral due to GW emission [16]. As pointed out in Sec. 1.2, both effects leave characteristic imprints on the emitted GW signals, and their simultaneous detection would provide key insights into the formation channels and evolutionary pathways of compact-object binaries.

At present, LIGO-Virgo-KAGRA data shows tantalizing evidence of both eccentricity [55, 56, 57, 108] and spin precession [5, 109, 56, 57] in a few GW events. The combined inference of the two effects is still beyond the horizon because of the related waveform-modeling challenges [110, 111, 112, 113] as well as potential degeneracies [53]. LIGO and Virgo can distinguish eccentricities [1] $e \gtrsim 0.05$, future ground third-generation detectors will push this limit to $e \gtrsim 10^{-4}$ [52], while LISA will be sensitive to $e \gtrsim 10^{-2.5}$ for supermassive BH binaries [114]. In practice, sources with eccentricities smaller than these thresholds are to be considered circular for observational purposes. For context, an equal-mass BH binary with total mass $M = 20\ M_\odot$ evolving in isolation under radiation reaction from an initial semi-major axis $a = 30\ R_\odot$ and an initial eccentricity $e = 0.6$ will reach the innermost stable orbit with eccentricity $e \sim 10^{-4}$. In other words,

[1] No unique definition of eccentricities exists in general relativity (see Ref. [51] and reference within). In this thesis, we consider eccentricity with its classical Keplerian definition. When quoting the minimum detectable values, we consider eccentricity as defined in Ref. [52], and measured at 10 Hz.

PN circularization is brutal, and most binaries that are formed on highly eccentric orbits might enter the detector sensitivity range with eccentricity values that are well below the distinguishability threshold [52, 71]. While hoping for prominent outliers [70, 57, 108], solid inference on orbital eccentricity might well remain challenging.

Thus, BH binaries that are observed as circular might have spent a significant fraction of their lifetime on eccentric orbits. Is this information somewhat accessible to GW detectors? Do merging BHs retain any memory of their eccentric past? In this chapter, we explore this line of reasoning and show that some information is indeed encoded in the spin sector of the gravitational dynamics. The evolution of the BH spins depends on the binary eccentricity [115, 41, 43, 116, 42] opening for the exciting possibility of using accurate spin measurements to infer the presence of eccentricity at BH formation, even if this does not correspond to eccentricity at detection. In particular, this chapter focuses on the methodological aspects of this problem and develops the appropriate formalism to capture long-term evolutions of precessing, eccentric BH binaries. Specifically, we exploit a multi-timescale approximation to the inspiral of BH binaries, which relies on averaging the dynamics in sequence over the short timescales of the problem (orbit and spin precession, see Sec. 1.3) while introducing the evolution over the longer timescale (radiation reaction) in a quasi-adiabatic fashion. This framework has been developed [34, 35] and extensively tested [117, 40] for circular binaries and is here fully generalized to eccentric sources (see also Refs. [43, 116, 42] for other attempts in this direction).

In a nutshell, the inclusion of eccentricity requires two ingredients:

(i) First, we show that the short-timescale dynamics of any eccentric binary can be mapped to that of an effective circular source. This is an extremely elegant property of the gravitational two-body problem, allowing us to make direct use of

the existing numerical infrastructure [40].

(ii) One then needs to add an evolutionary prescription for the decay of the orbital eccentricity on the radiation-reaction timescale. At leading order, this is the seminal result by Peters (1964) [16], which is here presented in a regularized form that allows for safe numerical evaluations at arbitrarily low eccentricities.

2.2 Binary evolution

We organize our discussion around the three key phenomena of the problem: orbit, precession, and radiation reaction. The former two have already been introduced in Sec. 1.3. In what follows, we extend the spin-precession equations to eccentric sources (Sec. 2.2.1) and analyze the evolution of eccentric, spin-precessing systems driven by GW emission (Sec. 2.2.2). Finally, we compare the relevant timescales in Sec. 2.2.4.

2.2.1 Spin precession

As discussed in Sec. 1.1, the 2PN spin-precession equations for eccentric orbits have been derived by several authors [98, 32, 42] and take the form

$$\frac{\mathrm{d}\boldsymbol{S}_1}{\mathrm{d}t} = \boldsymbol{\omega}_1 \times \boldsymbol{S}_1, \tag{2.1}$$

$$\frac{\mathrm{d}\boldsymbol{S}_2}{\mathrm{d}t} = \boldsymbol{\omega}_2 \times \boldsymbol{S}_2, \tag{2.2}$$

$$\frac{\mathrm{d}\boldsymbol{L}}{\mathrm{d}t} = \boldsymbol{\omega}_L \times \boldsymbol{L} + \frac{\mathrm{d}L}{\mathrm{d}t}\hat{\boldsymbol{L}}, \tag{2.3}$$

where

$$\boldsymbol{\omega}_1 = \frac{1}{2a^3\left(1-e^2\right)^{3/2}}\left\{\left[4+3q-\frac{3(1+q)\chi_{\rm eff}}{\sqrt{a\left(1-e^2\right)/M}}\right]\boldsymbol{L}+\boldsymbol{S}_2\right\}, \tag{2.4}$$

$$\boldsymbol{\omega}_2 = \frac{1}{2a^3\left(1-e^2\right)^{3/2}}\left\{\left[4+\frac{3}{q}-\frac{3(1+q)\chi_{\rm eff}}{q\sqrt{a\left(1-e^2\right)/M}}\right]\boldsymbol{L}+\boldsymbol{S}_1\right\}, \tag{2.5}$$

$$\boldsymbol{\omega}_L = \frac{1}{2a^3\left(1-e^2\right)^{3/2}}\left\{\left[4+3q-\frac{3(1+q)\chi_{\rm eff}}{\sqrt{a\left(1-e^2\right)/M}}\right]\boldsymbol{S}_1+\left[4+\frac{3}{q}-\frac{3(1+q)\chi_{\rm eff}}{q\sqrt{a\left(1-e^2\right)/M}}\right]\boldsymbol{S}_2\right\}, \tag{2.6}$$

model the conservative dynamics and $\mathrm{d}L/\mathrm{d}t$ encodes dissipation via GWs. Applying the same reasoning that led to Eq. (1.34), i.e., neglecting radiation reaction and using the conservation of $\chi_{\rm eff}$, one can compress Eqs. (2.1)-(2.6) into a single equation for the weighted spin difference $\delta\chi$ defined in Eq. (1.22) [40]

$$\begin{aligned} M\frac{\mathrm{d}\delta\chi}{\mathrm{d}t} = {} & \frac{3q}{(1+q)^2}\chi_1\chi_2\left(1-e^2\right)^{3/2}\left[\frac{a\left(1-e^2\right)}{M}\right]^{-3} \\ & \times\left[1-\frac{\chi_{\rm eff}}{\sqrt{a\left(1-e^2\right)/M}}\right]\sin\theta_1\sin\theta_2\sin\Delta\Phi\,. \end{aligned} \tag{2.7}$$

Thus $\delta\chi$, also in this case, evolves quasi-periodically in time, oscillating between the two extrema $\delta\chi_\pm$ which are, in turn, functions of a, e, q, χ_1, χ_2, $\chi_{\rm eff}$, and J. Setting $e=0$ in the expressions above trivially returns the equations used in Refs. [35, 40] which are reported in Eqs. (1.28)–(1.33) for circular binaries where $r=a$. Moreover, it is immediate to prove that the spins evolution of an eccentric binary on an orbit described by a and e is mathematically equivalent to that of a circular binary with orbital separation

$$a' = a\left(1-e^2\right), \tag{2.8}$$

provided one also changes the time variable to

$$t' = t\left(1-e^2\right)^{3/2}. \tag{2.9}$$

This change of variables for space and time is reminiscent of the Lorentz transformations of special relativity, where the eccentricity e enters the Lorentz factor $\gamma = 1/\sqrt{1-e^2}$ in place of the velocity v/c.

The spin properties of eccentric BH binaries can thus be mapped to those of an effective circular source. In other words, the eccentricity can be transformed away and dealt with in post-processing. We can thus make direct use of the numerical infrastructure that has already been developed for circular binaries: when tackling spin precession for eccentric sources, one can evolve the corresponding circular source and rescale the solution according to Eqs. (2.8) and (2.9). More about this computational implementation is explicitly reported in Sec. 2.4.

2.2.2 Radiation reaction

At lowest order, the eccentricity and semi-major axis evolve according to Peters' equations [16]

$$\frac{\mathrm{d}a}{\mathrm{d}t} = -\frac{64}{5}\frac{q}{(1+q)^2}\frac{1+\frac{73}{24}e^2+\frac{37}{96}e^4}{a^3\left(1-e^2\right)^{7/2}}M^3, \tag{2.10}$$

$$\frac{\mathrm{d}e}{\mathrm{d}t} = -\frac{304}{15}\frac{q}{(1+q)^2}\frac{e\left(1+\frac{121}{304}e^2\right)}{a^4\left(1-e^2\right)^{5/2}}M^3. \tag{2.11}$$

Equations (1.12), (2.10), and (2.11) can be used to derive the radiation-reaction timescale, which is the time over which GW effectively changes the binary orbit

$$\tau_{\rm rr} = \frac{L}{|\mathrm{d}L/\mathrm{d}t|} = \frac{5}{32}\frac{(1+q)^2}{qM^3}\frac{a^4\left(1-e^2\right)^{5/2}}{1+\frac{7}{8}e^2}\,. \tag{2.12}$$

Compared to other possible definitions, including the more common $a/|\mathrm{d}a/\mathrm{d}t|$, defining $\tau_{\rm rr}$ in terms of L as in Eq. (2.12) is more appropriate in our context because the

derivative $\mathrm{d}L/dt$ directly enters Eq. (2.3).

Equations (2.10) and (2.11) lead to several predictions when integrated either forward or backward in time from some initial condition (a_0, e_0). First, one has $\mathrm{d}a/\mathrm{d}t < 0$ for all values of a and e, which is trivially related to the fact that GWs can only dissipate energy and not inject it into the system. This implies one can use a as a time coordinate and consider $\mathrm{d}e/\mathrm{d}a = \mathrm{d}e/\mathrm{d}t \times (\mathrm{d}a/\mathrm{d}t)^{-1}$. If $e_0 = 0$, one has $\mathrm{d}e/\mathrm{d}a = 0$ and the orbit remains circular throughout its evolution. If $e_0 > 0$, one has $\mathrm{d}a/\mathrm{d}e > 0$, i.e., the eccentricity tends to decrease along with the semi-major axis, eventually approaching zero. Conversely, the eccentricity tends to increase when integrating backward in time up to $e = 1$. The $e_0 = 0$ case is akin to a point of unstable equilibrium: while perfectly circular binaries stay circular even at past time infinity, binaries that are eccentric (even if arbitrarily close to circular!) become parabolic when traced back far enough in time. In particular, for eccentric binaries one has [16]

$$\lim_{t\to-\infty} a \propto \frac{1}{1-e^2}\,, \tag{2.13}$$

which implies that, although $a \to \infty$ and $1 - e^2 \to 0$, their product stays constant. The key consequence is that the angular momentum L of an eccentric source from Eq. (1.12) asymptotes to a constant value when backpropagated to past time infinity. This is in contrast with the circular case, where instead the angular momentum $L \propto \sqrt{a}$ diverges for wide orbits. Such an asymptotic distinction between eccentric and circular binaries plays a pivotal role in this study and constitutes a fundamental aspect of the interplay between spins and eccentricity in BH binaries. The analytic results presented in Refs. [35, 40] in the $a \to \infty$ limit intrinsically rely on the divergence of L and thus cannot be generalized to eccentric orbits, with conceptual consequences for GW

population analyses [118] that still need to be explored. We note, however, that the Peters' equations themselves lose validity in this limit [119, 93]. Equations (2.10) and (2.11) have been orbit-averaged [16] and thus are valid only when $\tau_{\rm orb} \ll \tau_{\rm rr}$. From Eqs. (1.13), (2.12), and (2.13), it is straightforward to prove that the two timescales are of the same order of magnitude when $a \to \infty$ and $e \to 1$ (see Sec. 2.2.4 and Chap. 4).

2.2.3 Precession-averaged inspiral

We now proceed on extending the precession-average formalism to eccentric binaries. As pointed out in Eq. (1.36), generic quantity Y can be averaged to $\langle Y\rangle = \left(\int_0^{\tau_{\rm pre}} Y {\rm d}t\right)/\tau_{\rm pre}$, where the integral is more conveniently implemented using Eq. (2.7); cf. Ref. [40] and Eq. (1.35). Once the constants of motion are taken into account and both the orbital and precessional motions are averaged over, one only needs to connect quantities that vary on the radiation-reaction timescale. For the circular problem, there are only two such quantities, namely the magnitudes of the orbital and total angular momenta. The evolution thus reduces to integration a single ordinary differential equation (ODE) [34, 35]:

$$\frac{{\rm d}\kappa}{{\rm d}u} = \langle |\boldsymbol{S}_1 + \boldsymbol{S}_2|^2\rangle, \tag{2.14}$$

where

$$u = \frac{1}{2L}, \tag{2.15}$$

and

$$\kappa = \frac{J^2 - L^2}{2L}, \tag{2.16}$$

are convenient reparametrizations of L and J, respectively. The right-hand side of Eq. (2.14) depends on quantities that are either constants of motion or vary on $\tau_{\rm rr}$ and

can be written down in closed form [42, 40]. The key assumptions used in the derivation of Eq. (2.14) is that $\mathrm{d}\boldsymbol{L}/\mathrm{d}t$ is parallel to $\boldsymbol{L}$ and independent of the spins [34, 35], which are still true for eccentric binaries at leading order in radiation reaction [98]. We can thus use Eq. (2.14) as it is, provided one properly generalizes L as in Eq. (1.12). The eccentric problem, however, has three, and not two, quantities that vary on the radiation reaction time: a, e, and J (or some equivalent reparametrization). We already have two variables, κ and u. For the third, we choose

$$u_c \equiv u(a, e=0) = \frac{(1+q)^2}{2qM^2}\sqrt{\frac{M}{a}}\,, \tag{2.17}$$

which is the coordinate used previously for the integration of circular binaries and does not depend on e. In particular, the condition $0 \leq e < 1$ implies $u \geq u_c > 0$. The resulting evolutionary equation can be easily derived from Eq. (2.10) and (2.11) and reads:

$$\frac{\mathrm{d}u}{\mathrm{d}u_c} = -\frac{12u_c u\,(7u_c^2 - 15u^2)}{37u_c^4 - 366u_c^2u^2 + 425u^4}\,. \tag{2.18}$$

With some tedious but straightforward algebraic manipulation, the solution can be written down as

$$u_c u^{37/84}\left(\frac{u^2}{u_c^2}-1\right)^{121/532}\left(\frac{u^2}{u_c^2}-\frac{121}{425}\right)^{145/532} = k_0\,, \tag{2.19}$$

where k_0 is a constant that needs to be determined from the initial conditions u_{c0} and u_0. For an initially circular binary, one has $u_0 = u_{c0}$ and $k_0 = 0$. The only solution to Eq. (2.19) is indeed $u = u_c$, i.e., circular binaries stay circular. For an initially eccentric binary, one has $k_0 > 0$ and Eq. (2.19) can be solved numerically to identify $u(u_c)$. This is simpler and more accurate than numerically integrating Eq. (2.18).

Compared to the analytic expression for $a(e)$ reported in Ref. [16], our formulation has the key advantage of being regular in the limit of circular binaries —the first term in parentheses in Eq. (2.19) acting as a regularizer— and thus more amenable to numerical evaluations. In summary, given a set of constants of motion (q, χ_1, χ_2, $\chi_{\rm eff}$) and initial conditions (u_{c0}, u_0, κ_0), performing a precession-averaged evolution of an eccentric binary reduces to integrating the ODE (2.14) under the constraint imposed by Eq. (2.19). The ODE solver is identical to that of the circular case, and the root finder for $u(u_c)$ is an additional, but trivial, computational task. Overall, the performance of our implementation is similar to what we reported in Ref. [40] for the circular case.

2.2.4 Timescale separation

We now investigate the validity of our formalism. Averaging over the orbital and precessional motions in sequences relies on the timescale separation $\tau_{\rm orb} \ll \tau_{\rm pre} \ll \tau_{\rm rr}$. In the circular limit, this inequality trivially corresponds to the PN condition $a = r \gg GM/c^2$. As illustrated in Fig. 2.1, the eccentric case is less straightforward. In particular, one has

$$\frac{\tau_{\rm rr}}{\tau_{\rm orb}} \propto \begin{cases} a^{5/2} & \text{if} \quad e \to 0\,, \\ \text{const.} & \text{if} \quad e \to 1\,, \end{cases} \tag{2.20}$$

and

$$\frac{\tau_{\rm rr}}{\tau_{\rm pre}} \propto \begin{cases} a^{3/2} & \text{if} \quad e \to 0\,, \\ \text{const.} & \text{if} \quad e \to 1\,, \end{cases} \tag{2.21}$$

where the circular (parabolic) limit corresponds to the late time (early time) behavior of a generic eccentric source. It follows that, for eccentric binaries, the accuracy of the multitimescale approach does not keep on improving as one moves to larger and

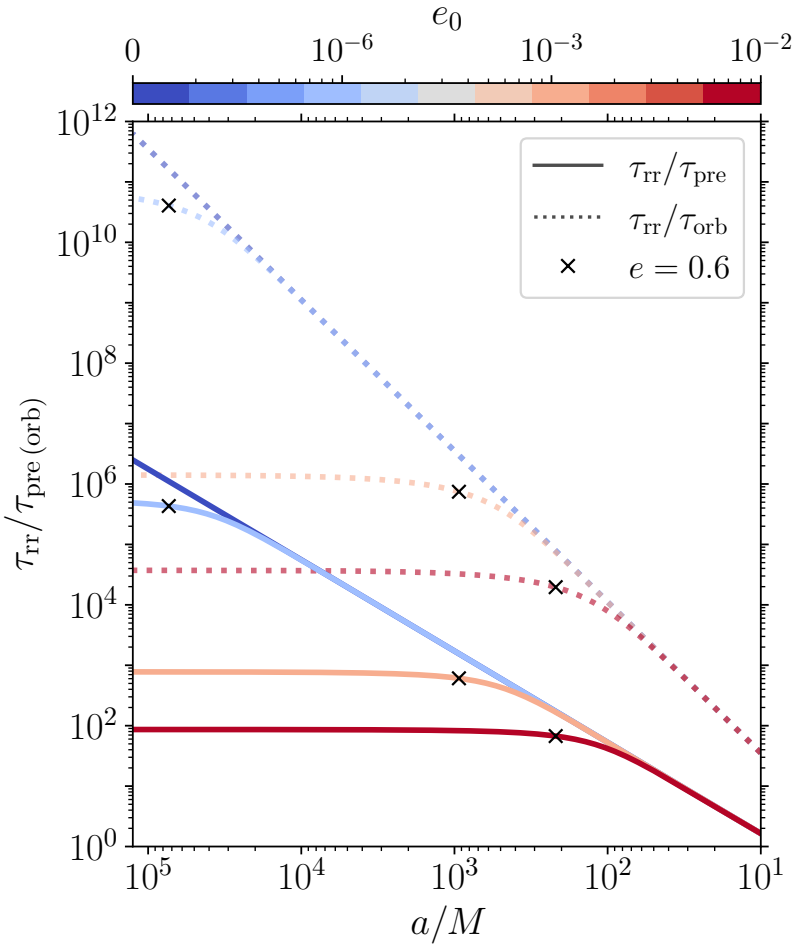

Figure 2.1: Evolution of the timescale ratios $\tau_{\rm rr}/\tau_{\rm pre}$ (solid) and $\tau_{\rm rr}/\tau_{\rm orb}$ (dotted) as a function of the binary semi-major axis for four GW sources with $q = 0.5$, $\chi_1 = 0.6$, $\chi_2 = 0.9$, and $(\theta_1, \theta_2, \Delta\Phi) = (\pi/3, \pi/4, -\pi/3)$. These are initialized with different eccentricities $e_0 = 0$, 10^{-6}, 10^{-3}, 10^{-2} at a separation $a = 10M$ as indicated on the color scale and propagated backward. Crosses indicate the location of the inspiral where the eccentricity reaches $e = 0.6$.

larger separations. Rather, it plateaus. From Fig. 2.1, the transition between the two behaviors takes place when $e \sim 0.5$. This is qualitatively different than the circular case, where multi-timescale evolutions are inaccurate close to merger (because of the breakdown of the PN approximation) but become increasingly accurate toward past time infinity [35].

We express the regime of validity of the multi-timescale approach in terms of two approximate conditions:

(i) At small separations, the pericenter distance should be sufficiently large for the equations to remain PN-valid. Borrowing the threshold from Ref. [120], we set $a(1-e) \gtrsim 10M$.

(ii) At large separations, the Peters' equations predict parabolic orbits. These have infinitely large periods, which is manifestly against the quasi-adiabatic approach used to derive the equations themselves. This is a known issue [121] and, in particular, Refs. [50, 119] suggest that orbit averaging can only be meaningfully applied if $e \lesssim 0.6$. We explore this problem in detail in Chap. 4.

These forbidden regions are highlighted in Fig. 2.2. In the remaining grey-shaded region, the applicability of our formalism depends on the precession timescale. Figure 2.2 shows contours of $\tau_{\rm rr}/\tau_{\rm pre}$ for populations of BH binaries with different values of the mass ratio, averaging over both spin magnitudes and directions. Regions to the left of each curve correspond to $\tau_{\rm rr}/\tau_{\rm pre} > 100$, which is safe territory for the multi-timescale approach. This is not dissimilar to the circular case [35] and, indeed, the black curves in Fig. 2.2 remain essentially vertical, i.e., independent of the eccentricity. The $e = 0.6$ limit indicated in condition (ii) above roughly separates the region of the parameter space where the $\tau_{\rm rr}/\tau_{\rm pre}$ contours start bending leftward. For a quick rule of thumb, our

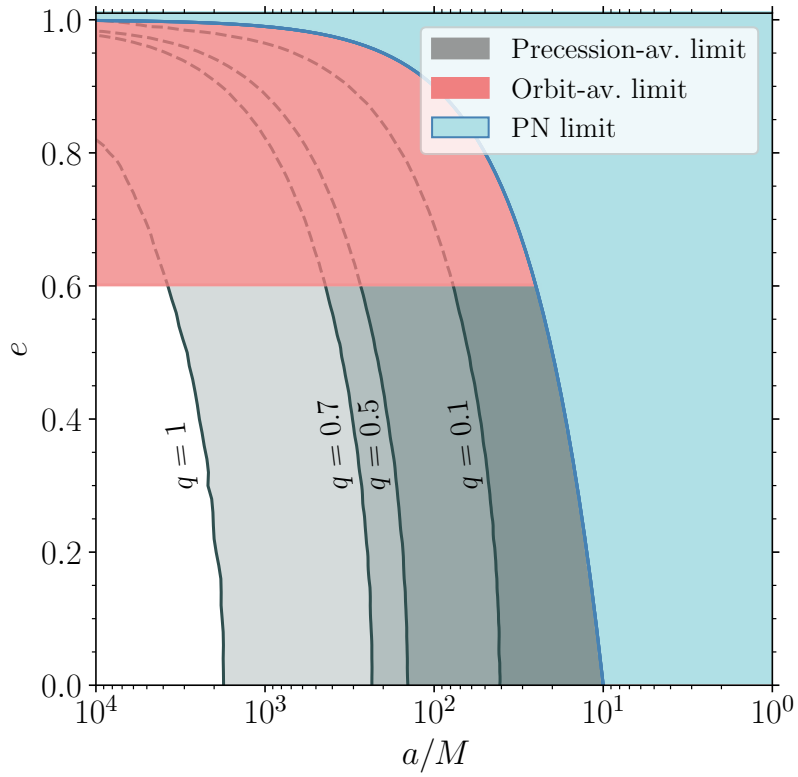

Figure 2.2: Validity region of the precession-average formalism as a function of binary semi-major axis a and eccentricity e. The light blue area indicates the region where the close-passage distance is $a(1-e) < 10M$, likely beyond the regime of validity of the PN approximation. The red area indicates the condition $e > 0.6$, which is our conservative limit for the inapplicability of the orbit-averaged approach to radiation reaction. The black solid curves show the condition $\tau_{\rm rr}/\tau_{\rm pre} = 100$, with > 100 being true in the lighter regions to the left of each curve. We average the value of $\tau_{\rm rr}/\tau_{\rm pre}$ over four sets of binaries with fixed mass ratios $q = 0.1, 0.5, 0.7, 1$ and spins that are generated uniformly in magnitudes in $[0.1, 1]$ and isotropic in directions.

multi-timescale approach can be applied to eccentric binaries much like in the circular case as long as the eccentricity is small to moderate, with $e = 0.6$ providing a nominal threshold. The high-eccentricity case requires a new formalism, perhaps averaging over the various phenomena entering the dynamics (orbit, precession, inspiral, eccentricity decay) in a different order (see Chap. 4).

2.3 Phenomenology

We first describe our findings in terms of the parameter that most directly enters our formalism in Sec. 2.3.1. Then, in Secs. 2.3.2 and 2.3.3, we present predictions for quantities that are more directly observable, like spin tilts and morphologies.

2.3.1 Weighted spin difference

Compared to the quasi-circular case, eccentricity enters our formalism in two key aspects. First, the coordinate transformation of Eqs. (2.8) and (2.9) accelerates the evolution of all quantities that vary on the precession timescale, including the spin directions (this feature was already noted in Ref. [122]). Second, the orbital angular momentum L does not diverge as $t \to -\infty$ [16]. For quasi-circular binaries, the right-hand side of Eq. (2.7) tends to zero in this limit, which implies that at large separations, BH spins move on precession cones of constant opening angles $\theta_{1,2}$ [40]. This is not true in general for eccentric binaries, suggesting that, even at early times, the BH spin continues to nutate with an amplitude that approaches a constant value and does not degenerate to zero (but see Sec. 2.2.4 on the validity of our formalism). Figure 2.3 shows the precession-timescale evolution (i.e., without radiation reaction) of the weighted spin difference $\delta\chi$ for three binaries with different eccentricities. Notably, the spins of

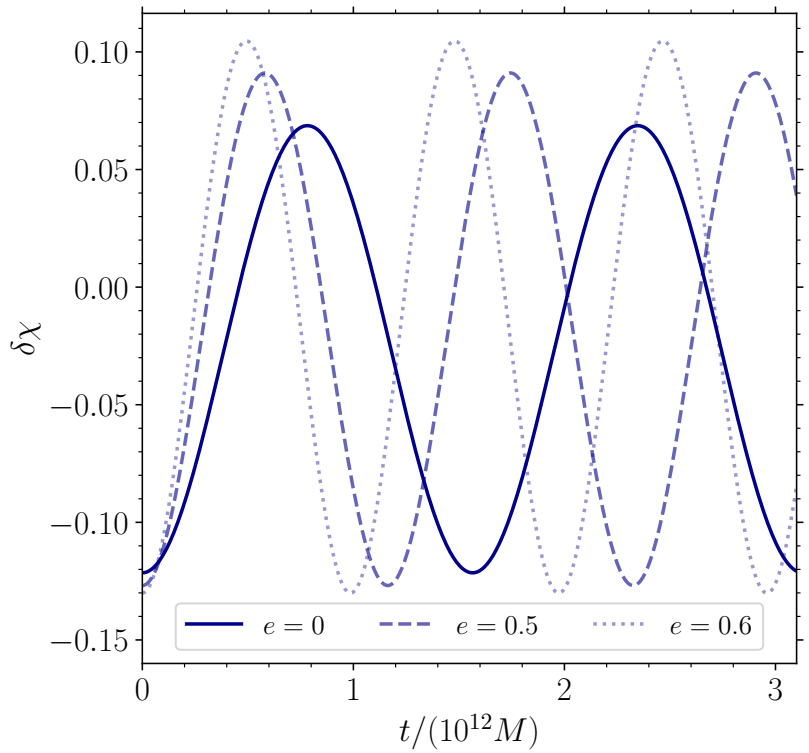

Figure 2.3: Time evolution of the weighted spin difference $\delta\chi$ for three representative BH binaries with mass ratio $q = 0.95$, spin magnitudes $\chi_1 = \chi_2 = 0.9$, initial spin orientations $(\theta_1, \theta_2, \Delta\Phi) = (\pi/3, \pi/4, -\pi/3)$, semi-major axis $a = 10^4 M$, and eccentricities $e = 0$ (solid), 0.5 (dashed), and 0.6 (dotted). In terms of the deviation parameter from Eq. (2.23), these three sources have $\Delta = 0$, 1.5×10^{-3}, and 2.4×10^{-3}, respectively.

eccentric binaries oscillate with a shorter period and a larger amplitude. These are direct consequences of the two dynamical features we just highlighted.

We further quantify the impact of eccentricity on spin precession with a suitable deviation parameter Δ. We first precession-average $\delta\chi$ and rescale it to its oscillation amplitude [40]

$$\langle\delta\tilde{\chi}\rangle = \frac{\langle\delta\chi\rangle - \delta\chi_-}{\delta\chi_+ - \delta\chi_-} \in [0, 1]\,. \tag{2.22}$$

We then compute $\langle\delta\tilde{\chi}\rangle$ for a given eccentric binary and compare it against an equivalent

quantity $\langle\delta\tilde{\chi}\rangle_c$, which is estimated assuming the same values of a, q, χ_1, χ_1, θ_1, θ_2 and $\Delta\Phi$ but setting $e = 0$. Our deviation parameter is then defined as

$$\Delta = \frac{\langle\delta\tilde{\chi}\rangle - \langle\delta\tilde{\chi}\rangle_c}{\langle\delta\tilde{\chi}\rangle + \langle\delta\tilde{\chi}\rangle_c} \in [-1, 1]\,, \tag{2.23}$$

and can be interpreted as a fractional measurement of the impact of eccentricity on spin precession. Figure 2.4 illustrates the value of Δ across some sections of our parameter space. We consider six sets with fixed mass ratios and spin magnitudes and average our results over spin directions distributed isotropically. In general, we find that the magnitude $|\Delta|$ increases with both the mass ratio and the spin magnitudes, signaling an enhanced interplay between spins and eccentricity in such systems. The deviation Δ is largely positive across the parameter space, with the key exception of binaries with nearly equal masses and large spins. Note that Δ is a precession-averaged quantity and as such is only accurate when the underlying timescale hierarchy is respected.

2.3.2 Spin orientations

While $\delta\chi$ is the quantity that directly enters our formalism, a more intuitive insight can be gained by rephrasing our findings in terms of the spin angles θ_1, θ_2, and $\Delta\Phi$. Our results are shown in Figs. 2.5 and 2.6 for some representative sources. Note we only illustrate the range of variation of each of these angles as the timescale separation $\tau_{\rm pre} \ll \tau_{\rm rr}$ implies they oscillate many times at each orbital separation. Figure 2.5 shows the evolution of three systems with $q = 0.95$, $\chi_1 = \chi_2 = 0.96$, and initial spins orientation $(\theta_1, \theta_2, \Delta\Phi) = (\pi/3, 2\pi/3, -\pi/9)$. Integrations are initialized at the initial semi-major axis $a_0 = 4000M$, considering three different initial eccentricities $e_0 = 0$, 0.5, and 0.6. While we can formally integrate both forward and backward in time (i.e.,

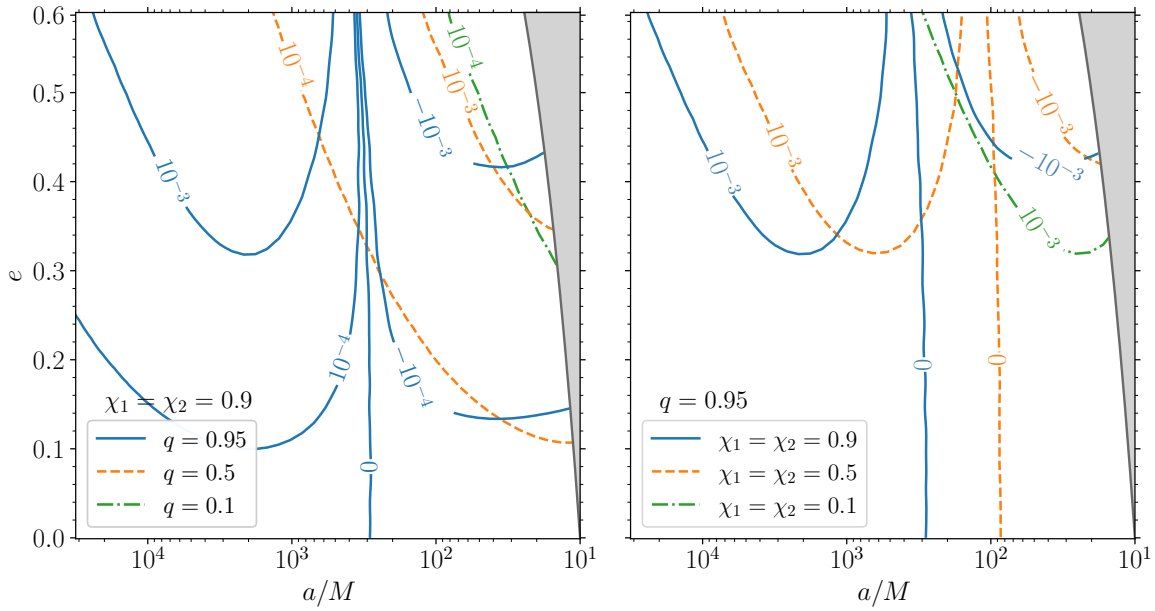

Figure 2.4: Spin-eccentricity interplay in terms of the deviation parameter Δ as a function of binary semi-major axis a and eccentricity e. We consider sources with $e < 0.6$, which sets the validity of our model (Sec. 2.2.4). For each panel, we consider three sets of BH binaries with different mass ratios and spin magnitudes. In all cases, we average over the orientations of the spins, which are assumed to be distributed isotropically. In the right panel, we set $\chi_1 = \chi_2 = 0.9$ and vary $q = 0.95$ (blue solid), 0.5 (orange dashed), and 0.1 (green dotted). In the left panel, we instead set $q = 0.95$ and vary $\chi_1 = \chi_2 = 0.9$ (blue solid), 0.5 (orange dashed), and 0.1 (green dotted). The blue solid contours are the same across the two panels. Grey areas indicate the region $a(1-e) \leq 10M$ where the PN approximation breaks down.

toward smaller and larger eccentricities, respectively), we expect our formalism to break down at early times when $e \gtrsim 0.6$, cf. Sec. 2.2.4 and Chap. 4.

The key message here is that the spins of these binaries trace different precession cones as they evolve toward merger. That is, the spin dynamics depends on the eccentricity. As these binaries approach merger, the range the spin angles can vary within is smaller for sources with larger initial eccentricities. It is worth noting that this is true even if the eccentricity of all three sources close to merger is essentially zero ($e \sim 10^{-4}$ at $a = 30M$): the spins of BH binaries at small separations (i.e., when they

become detectable by our instruments) "remember" their past evolution on eccentric orbits. The smaller nutation amplitude observed close to merger for the eccentric evolutions compared to the circular case is consistent with the results reported in Sec. 2.3.1 for BH binaries with nearly equal masses and high spins. While this is the case for the sources in Fig. 2.5, we do not expect this to be a generic feature.

The strong features observed at $a \simeq 2210M$ $(4000M)$ for the $e_0 = 0$ (0.5) binary in Fig. 2.5 are phase transitions of the spin dynamics. These configurations were studied at length in Ref. [35] and correspond to cases where one of the two spins is instantaneously aligned or anti-aligned with the angular momentum (in this case $\hat{\boldsymbol{S}}_2 = -\hat{\boldsymbol{L}}$, i.e. $\theta_2 = \pi$) and the azimuthal angle $\Delta\Phi$ is instantaneously ill-defined. The occurrence of these phase transitions is deeply affected by the eccentricity to the point that, at least for these specific cases, the transition itself disappears in the case of the most eccentric source. This point is further explored in Sec. 2.3.3 below. While likely outside the regime of validity of our formalism, the backward integration of these sources toward larger separation shows how eccentric sources maintain a finite nutation amplitude, i.e., the range of variations of $\theta_{1,2}$ does not go to zero as a increases. This is a direct consequence of the magnitude of the orbital angular momentum remaining finite at past time infinity. The eccentric binaries of Fig. 2.5 reach merger with eccentricities of $\sim 10^{-4}$, which is well below the distinguishability threshold of our detectors [52]. In practice, these sources will all be classified as circular. Figure 2.6 demonstrates the impact of such indistinguishability on the reconstruction of the spin history. We consider the same $e_0 = 0.6$ evolution of Fig. 2.5, where the source is evolved from large to small separations. We then take the final condition, reset its residual eccentricity to 0, and evolve it back to the initial large separation. This "back and forth" evolution is *not* invertible, i.e., the binary does not go back to where it started in parameter space. As

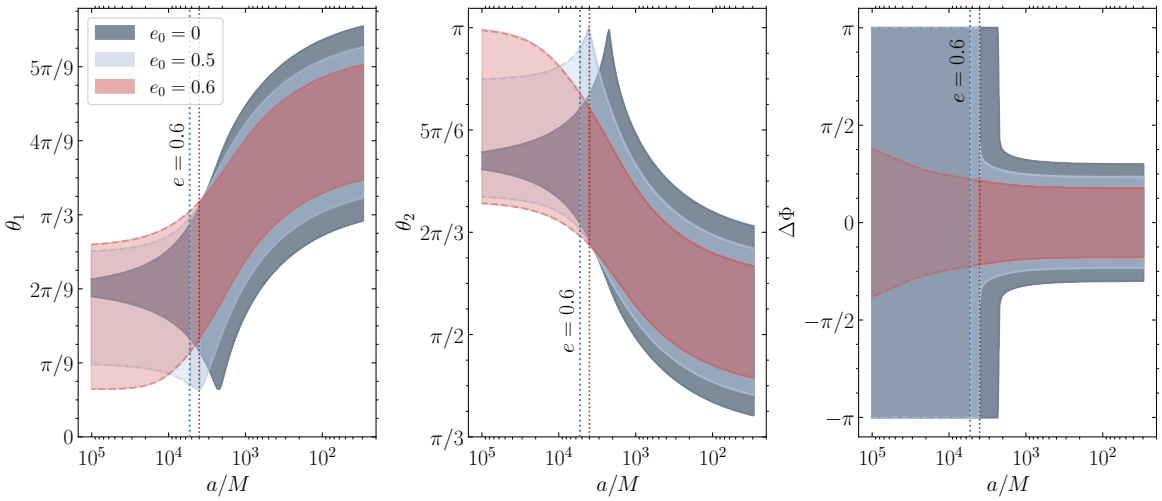

Figure 2.5: Evolution the spin angles θ_1 (left), θ_2 (middle), and $\Delta\Phi$ (right) under radiation reaction. Each of the angles oscillates in the reported ranges. We consider three binaries with mass ratio $q = 0.95$, spin magnitudes $\chi_1 = \chi_2 = 0.96$, and initial spins orientation $(\theta_1, \theta_2, \Delta\Phi) = (\pi/3, 2\pi/3, -\pi/9)$. Sources are evolved assuming initial eccentricities $e_0 = 0$ (dark grey), 0.5 (light grey), and 0.6 (red) at $a_0 = 4000M$. We track the evolution both forward to $a = 30M$ and backward to $a = 10^5 M$. At large separations, the eccentricity grows beyond $e = 0.6$ (vertical dotted lines) and our formalism loses validity (lighter shaded areas and dashed curves).

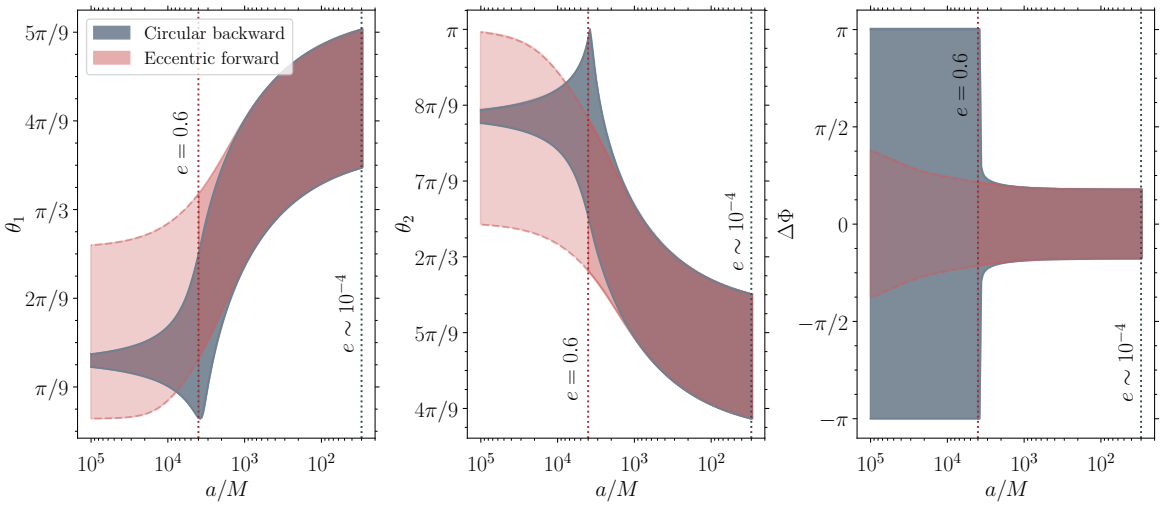

Figure 2.6: Forward and backward evolution of the spin angles θ_1 (left), θ_2 (middle), and $\Delta\Phi$ (right), resetting the eccentricity to zero near merger. We consider the same binary of Fig. 2.5 with $q = 0.95$, $\chi_1 = \chi_2 = 0.96$, $(\theta_1, \theta_2, \Delta\Phi) = (\pi/3, 2\pi/3, -\pi/9)$, $a_0 = 4000M$, and $e_0 = 0.6$, and evolve it toward merger (red). At $a = 30M$, this binary has an eccentricity $e \sim 10^{-4}$. We artificially set this value to zero and evolve the same binary backward to large separations (dark grey).

shown in Fig. 2.6, the two evolutions are similar to each other only at small separations when the eccentricity is low and differ as e increases. For context, the forward evolution had $e \sim 0.14$ at $a = 1000M$. The backward evolution (i.e., which in this example corresponds to our reconstructed information) exhibits a prominent phase transition that is absent in the eccentric forward evolution (i.e., which corresponds to the actual source). This experiment shows that eccentricity, even when it is far below the threshold of distinguishability, poses a serious challenge when attempting a reconstruction of the binary formation history using the spin directions [78, 123, 124, 63, 77, 69, 125]. Residual eccentricity is a systematic uncertainty that needs to be taken into account when interpreting GW data. Chapter 3 is entirely dedicated to dissecting this problem.

2.3.3 Spin morphologies

The parameter space of precessing BH binaries can be divided into three distinct regions, or "morphologies," according to the evolution of the azimuthal angle $\Delta\Phi$ [35, 40, 105]. In particular, this angle can either (i) circulate between $\Delta\Phi = 0$ to $\Delta\Phi = \pm\pi$, (ii) librate about $\Delta\Phi = 0$ (and never reach $\Delta\Phi = \pm\pi$), or (iii) librate about $\Delta\Phi = \pm\pi$ (and never reach $\Delta\Phi = 0$). In particular, the zero-amplitude limits of the two librating morphologies are the so-called spin-orbit resonances of the spin precession problem [98]. While morphology is an integrated quantity defined over an entire precession cycle, radiation reaction causes secular transitions between the different classes. Some examples are shown in Figs. 2.5 and 2.6, where in both cases the $e = 0$ and $e = 0.5$ binaries belong to the circulating morphology at large separations and transition toward the librating about $\Delta\Phi = 0$ morphology at some point during the inspiral. Classifying BH binaries in terms of these classes is promising because, at least for the quasi-circular problem, the morphology near merger (where binaries are detected) tracks the spin tilts at large

separations (where binaries are formed) [35, 126]. For circular sources, one can prove that all binaries belong to the circulating morphology at large separations, while the two librating morphologies can only be populated by transitions occurring during the inspiral [40]. Once more, this feature is due to the divergence of L at early times and does not hold for eccentric sources. This implies that eccentric binaries will more likely be found in the two librating morphologies compared to their circular counterparts. This point is illustrated in Fig. 2.7. We consider BH binaries with $q = 0.95$, $\chi_{1,2}$ uniformly distributed in $[0.5, 1]$, and spin orientations distributed isotropically. Sources are evolved backward in time from small ($a_0 = 30M$) to large separations ($a_{\rm f} = 10^6 M$) with an initial eccentricity $e_0 = 2 \times 10^{-3}$. We report the fraction of binaries in each of the spin morphologies, together with analogous fractions obtained by setting $e_0 = 0$. The key conclusion is that, as the evolution proceeds, some eccentric sources remain in their librating morphologies at large separations while all circular binaries transit to circulation. This may have significant implications when attempting to use spin morphologies to constrain astrophysical formation channels.

2.4 Numerical implementation

As presented in Sec. 2.2.1, on the precessional timescale, the dynamics of an eccentric binary can be mapped onto that of an effective circular source through the coordinate transformations of Eqs. (2.8) and (2.9). This has the advantage of directly utilizing the numerical implementation of the formalism of Gerosa *et al.* (2023) PRECESSION[2] [127], after a few modifications which we report in the following section. This section is based on the original work presented in Fumagalli *et al.* (2025) as the proceedings of the 24th International Conference on General Relativity and Gravitation and the 16th

[2] PRECESSION is distributed via git (github.com/dgerosa/precession)

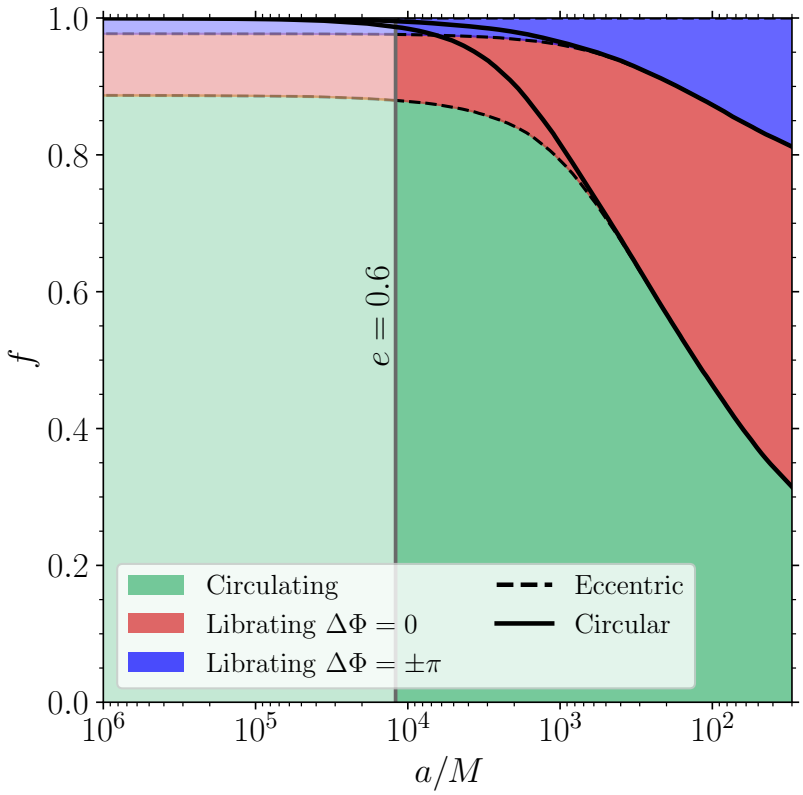

Figure 2.7: Fraction of eccentric (colored areas and dashed black curves) and circular (solid black curves) binaries falling in each of the three morphologies as a function of the binary semi-major axis a. We assume a set of BH binaries with fixed mass ratio $q = 0.95$, spin magnitudes $\chi_{1,2}$ uniformly distributed in $[0.5, 1]$, and isotropic spin directions. Sources are initialized at $(a_0 = 30M, e_0 = 2 \times 10^{-3})$ and evolved backward to $a = 10^6 M$. Lighter areas to the left of the vertical grey line indicate the region where $e > 0.6$ and our formalism loses validity.

Edoardo Amaldi Conference on Gravitational Waves. Fumagalli *et al.* (2025) has been submitted together with a fully working implementation of the framework presented in this chapter, which constitutes version 2.1 of PRECESSION.

To implement the mapping involving the orbital separation, we developed a utility that dynamically wraps functions in PRECESSION using a Python decorator. This decorator, named `eccentricize`, modifies the user-facing interface of selected functions by replacing the argument r with a and e. Internally, the functions continue to operate in terms of r, which is computed from a and e via Eq. (2.8), thereby preserving their original logic while extending compatibility to eccentric binaries. The decorator also updates function signatures and docstrings to reflect the new input parameters. Consequently, there is no need to manually rewrite each function from the circular version of PRECESSION. While this addresses the a re-mapping, functions that explicitly depend on time have been manually modified, as they already required additional adjustments to extend their applicability to eccentric orbits.

Not all functions in PRECESSION can be extended to the eccentric case using the `eccentricize` decorator. Some require more careful treatment, either because they do not have a counterpart in the circular case (e.g., the definition and evolution of eccentricity) or because they involve non-trivial modifications.

The inspiral of a BH binary using orbit-averaged equations is implemented in `inspiral_orbav`. For circular binaries, PRECESSION employs the 2PN spin-precession equations together with the 3.5PN orbital-velocity evolution equation (including spin terms up to 2PN; see Sec. V of Ref. [40]). For eccentric binaries, we have implemented the 2PN spin-precession equations and the 3PN evolutionary equations for the semi-major axis and eccentricity (with spin terms up to 2PN) [see Eqs. (C1a)–(C2l) of Ref.[41]]. Three additional angular variables appear in this case: Ψ_1, Ψ_2, and $\delta\lambda$ [43, 41, 42]. The

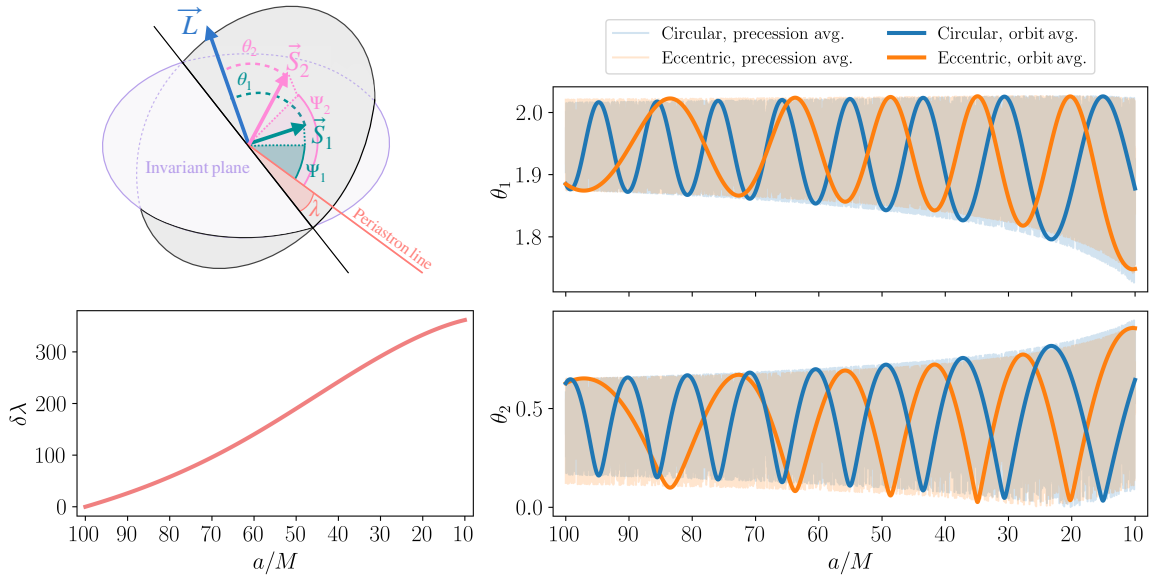

Figure 2.8: Orbit-averaged (heavy) and precession-averaged (light) evolution of the spin angles θ_1 (top-right) and θ_2 (bottom-right) under radiation reaction. The orbit-averaged evolution of the periastron angle $\delta\lambda$ is shown in the bottom-left panel. We consider two binaries with mass ratio $q = 0.8$, spin magnitudes $\chi_1 = 0.7$, $\chi_2 = 0.6$, and initial spin orientations $(\theta_1, \theta_2, \Delta\Phi) \approx (3/5\,\pi, 1/5\,\pi, 9/10\,\pi)$. The systems are evolved from $a_0 = 100M$ to $a = 10M$, assuming initial eccentricities $e_0 = 0$ (blue) and $e_0 = 0.5$ (orange). The geometric configuration of the eccentric binary is shown in the top-left panel.

first two describe the angles between the projections of the spin vectors onto the orbital plane and the periastron line, while the third identifies the position of the periastron, as illustrated in Fig. 2.8. Therefore, in addition to tracking the spin orientations, it is also necessary to evolve $\delta\lambda$. In the implementation we present here, we adopt the evolution equation for the latter as given in Eq. (17b) of Ref. [42]. In Fig. 2.8 we present an example of orbit-averaged evolution of the tilt angles θ_1, θ_2, and $\delta\lambda$ for a BH binary with an initial eccentricity of $e_0 = 0.5$, initialized at a large separation ($a = 100M$) and evolved down to $a = 10M$. For comparison, we also show the evolution of the spin angles for the same binary initialized with $e_0 = 0$ (the circular case). We note that,

when setting $e = 0$, the eccentric and circular evolutions do not coincide, because the derivative of e (expressed in terms of e^2 to avoid divergences) is not zero. This is a known feature of orbit-averaged equations [115, 41, 43], which encodes the influence of spins on eccentricity. We verify that these discrepancies vanish when spin terms are turned off.

Another aspect that required careful handling is the conversion between the GW emission frequency $f_{\rm GW}$ and the orbital separation, namely `pnseparation_to_gwfrequency` and `gwfrequency_to_pnseparation`. For eccentric binaries, GW emission is more complex than in the circular case [15], as it occurs across multiple harmonics of the orbital frequency. Moreover, the distribution of power among these harmonics depends sensitively on the eccentricity [15, 128, 129]. In this implementation, we proceed as follows: given the semi-major axis a and eccentricity e, we first compute the orbital frequency ω and then map ω to $f_{\rm GW}$, either considering the second harmonic, which dominates in the circular limit, or the harmonic that carries the maximum power. The latter is identified using the fitting formulae of Refs. [128, 129], which we have reimplemented. If ω or $f_{\rm GW}$ at a specific harmonic is known, and the eccentricity e is given, the corresponding semi-major axis can be directly computed using Eqs. (4a) and (B2a) of Ref. [41]. To perform the inverse operation—recovering the frequency from the semi-major axis—we analytically invert Eq. (B2a) of Ref. [41], obtaining

$$M\omega = \left(\frac{M}{a}\right)^{3/2} + \mathcal{A}_{\rm 1PN}\left(\frac{M}{a}\right)^{5/2} + \mathcal{A}_{\rm 1.5PN}\left(\frac{M}{a}\right)^{3} + \mathcal{A}_{\rm 2PN}\left(\frac{M}{a}\right)^{7/2} \tag{2.24}$$

where the coefficients are defined as

$$\mathcal{A}_{\rm 1\,PN} = -\frac{1}{2(1+q)^2(1-e^2)}\left\{3 + q(5+3q) - e^2\left[9 + q(17+9q)\right]\right\}, \tag{2.25}$$

$$\mathcal{A}_{1.5\,\mathrm{PN}} = -\frac{1}{2(1+q)^2(1-e^2)^{3/2}}\left\{\left[2+3q+3e^2(2+q)\right]\chi_1\cos\theta_1+\right.$$
$$\left.+\,q\left[3+2q+3e^2(1+2q)\right]\chi_2\cos\theta_2\right\}, \tag{2.26}$$
$$\mathcal{A}_{2\,\mathrm{PN}} = \frac{1}{8(1+q)^4\left(1-e^2\right)^2}\Big\{75-60\sqrt{1-e^2}+\left(323-216\sqrt{1-e^2}\right)q+$$
$$+\left(499-312\sqrt{1-e^2}\right)q^2+\left(323-216\sqrt{1-e^2}\right)q^3+\left(75-60\sqrt{1-e^2}\right)q^4+$$
$$+\,e^2\left[36+60\sqrt{1-e^2}+q\left(38+216\sqrt{1-e^2}\right)-\left(2-312\sqrt{1-e^2}\right)q^2+\right.$$
$$\left.+\left(38+216\sqrt{1-e^2}\right)q^3+12\left(3+5\sqrt{1-e^2}\right)q^4\right]+e^4\left(147+563q+\right.$$
$$\left.+\,835q^2+563q^3+147q^4\right)+3(1+q)^2\left(1+e^2\right)\left[2\,q\,\chi_1\chi_2\left(2\cos\theta_1\cos\theta_2+\right.\right.$$
$$\left.\left.-\cos\Delta\Phi\sin\theta_1\sin\theta_2\right)+\left(3\cos\theta_1^2-1\right)\chi_1^2+\left(3\cos\theta_2^2-1\right)q^2\chi_2^2\right]\Big\}. \tag{2.27}$$

In the previous, circular-only version of PRECESSION, the conversions between r and f_{GW} were based on Eqs. (4.5) and (4.13) of Ref. [30]. However, these did not include the spin-induced quadrupole term, a contribution that enters at 2PN order [31, 32]. In the current release of the code, we have corrected the expressions for the circular case, now including this missing contribution. While the impact of this term in the frequency-separation conversion equation is expected to be small, it is nonetheless important for consistency and completeness in spin-precession modeling.

PRECESSION also includes a legacy implementation of analytic fits for the post-merger BH mass, spin, and recoil [127]. These fits were developed only for quasi-circular binaries and, therefore, have not been ported to the eccentric version of the code.

2.5 Conclusions

Spin precession and eccentricity are precise indicators of the astrophysical origin of binary BHs in both the stellar-mass and the supermassive regimes. As binaries evolve

from formation to merger, couplings between the orbital eccentricity and the BH spins enter the dynamics, with potential consequences for our astrophysical inference.

Binaries tend to circularize during their long inspiral before merger [16], which implies most sources are expected to enter the sensitivity window of our detectors with vanishingly small eccentricities, likely below the distinguishability threshold [52, 114]. This chapter shows that the spin evolution retains some memory of the eccentric past of BH binaries. The implications are twofold, with a pro and a con:

(i) Because the spin orientations depend on the eccentricity, interplay between the two effects provides an avenue to infer that sources *formed* on eccentric orbits even if they are not *detected* as such. Astrophysical degeneracies will likely prevent us from inferring this effect on an event-by-event basis, but the implications for the GW population problem are promising. If a sizable fraction of BH binaries forms on eccentric orbits, this should have an impact on the statistical properties of the spin orientations inferred via GWs. The next step is to formalize this intuition in terms of concrete observational predictions.

(ii) The interplay between orbital eccentricity and spin precession implies that inference using the latter will be polluted by the former. The broader program of inferring the astrophysical formation channels of BH binaries using the spin directions thus suffers from an important systematic, namely residual eccentricity. Analyses that attempt reconstructing the spin history of BH binaries should be carried out taking residual eccentricity into account. The next step is to design a suitable strategy to "marginalize out" this source of uncertainty. Chapter 3 is entirely dedicated to a deeper analysis of these issues.

In this chapter, we present a multi-timescale treatment of the binary dynamics

able to capture moderately eccentric sources, generalizing results that were previously restricted to circular orbits [35, 40] (see also Refs. [43, 116, 42, 117]). This extension involves two key steps: an analytical rescaling of the spin-precession equations and an additional prescription for the evolution of the eccentricity itself. We explored the resulting phenomenology showing in particular how eccentricity impacts (i) the dynamical quantities entering our formalism, (ii) the nutation amplitude of the BH spins and (iii) the so-called spin morphologies. Our findings are implemented in the latest public version (see Sec. 2.4) of the PRECESSION code [127, 40]. It is important to stress that our approach relies on the well-known, orbit-averaged PN equations of motion [16], which cannot be used reliably when the eccentricity is $e \gtrsim 0.6$ [119]. Pushing our formalism beyond this limit is a promising avenue for future work, which likely requires going back to the drawing board aand carefully considering how the different timescales separate across the parameters space. This work is initiated in Chap. 4.

2.6 Looking ahead: spin precession in neutron stars and exotic compact objects

The formalism introduced in this chapter focuses only on BH binaries. What about other compact objects? Similar to BHs, NSs, and exotic objects like Boson stars are compact objects that can spin and form binaries, which, in turn, can emit GWs. In contrast to BHs, these kinds of objects can be easily deformed. The intrinsic angular momentum of the bodies distorts their mass distribution in a way that explicitly depends on the equation of state of the bodies. This can be quantified via the quadrupole-moment tensor, which, assuming rigid rotation, axial symmetry, and reflection symmetry about

the equatorial plane, is given for a general object A, by [130]

$$Q_{\rm A}^{\langle ij\rangle} = -\frac{k_{\rm A}}{m_1}\left(S_{\rm A}^i S_{\rm A}^j - \frac{1}{3}\delta^{ij} S_{\rm A}^k S_{\rm A}^k\right), \tag{2.28}$$

where $\langle ij\rangle$ represents the symmetric trace-free projection, $S_{\rm A}^i = \chi_A m_A^2 \hat{S}_{\rm A}^i$, and k_A is a constant (up to the PN order considered) that depends on the equation of state of the body. An important consequence of the no-hair theorem implies that, for BHs, k_A is exactly equal to 1, while for other objects, it can assume different values and, in particular, would be $\mathcal{O}(10)$ for NSs [131] and $\mathcal{O}(100)$ for Boson stars [132, 133].

To Newtonian order, this quadrupole introduces an extra coupling in the gravitational potential between the mass quadrupole of each spinning compact object and the mass of its companion. Considering a binary system like the one described in Sec. 1.3, the contribution of this "quadrupole-monopole" interaction to the evolution of the spin of, for example, the most massive body, is given by

$$\frac{{\rm d}S_1^i}{{\rm d}t} = 3\epsilon_{ijk} Q_1^{\langle jm\rangle} m_2 \frac{r^{\langle k} r^{m\rangle}}{r^3}, \tag{2.29}$$

where r^i is a unit vector pointing in the direction of the r. By substituting Eq. (2.28) into Eq. (2.29) one obtians

$$\frac{{\rm d}\boldsymbol{S}_1}{{\rm d}t} = \frac{3}{r^3} q k_1 (\hat{\boldsymbol{r}} \times \boldsymbol{S}_1)(\boldsymbol{S}_1 \cdot \hat{\boldsymbol{r}}). \tag{2.30}$$

This term can be included in the spin-precession equations and, as previously mentioned in Sec. 1.3, enters at 2PN order

$$\frac{{\rm d}\boldsymbol{S}_1}{{\rm d}t} = \frac{1}{2r^3}\left\{\left(4+\frac{3}{q}\right)\boldsymbol{L} + 6q\left[\hat{\boldsymbol{r}}\cdot\left(k_1\boldsymbol{S}_1 + \frac{\boldsymbol{S}_2}{q}\right)\right]\hat{\boldsymbol{r}} - \boldsymbol{S}_2\right\} \times \boldsymbol{S}_1, \tag{2.31}$$

$$\frac{\mathrm{d}\boldsymbol{S}_2}{\mathrm{d}t} = \frac{1}{2r^3}\left\{(4+3q)\,\boldsymbol{L} + 6\left[\hat{\boldsymbol{r}}\cdot\left(\boldsymbol{S}_1 + \frac{k_2}{q}\boldsymbol{S}_2\right)\right]\hat{\boldsymbol{r}} - \boldsymbol{S}_1\right\}\times\boldsymbol{S}_2, \tag{2.32}$$

$$\begin{aligned}\frac{\mathrm{d}\boldsymbol{L}}{\mathrm{d}t} = &-\frac{1}{2r^3}\left\{(4+3q)\,\boldsymbol{L} + 6q\left[\hat{\boldsymbol{r}}\cdot\left(k_1\boldsymbol{S}_1 + \frac{\boldsymbol{S}_2}{q}\right)\right]\hat{\boldsymbol{r}}\right\}\times\boldsymbol{S}_1 + \\ &-\frac{1}{2r^3}\left\{\left(4+\frac{3}{q}\right)\boldsymbol{L} + 6\left[\hat{\boldsymbol{r}}\cdot\left(\boldsymbol{S}_1 + \frac{k_2}{q}\boldsymbol{S}_2\right)\right]\hat{\boldsymbol{r}}\right\}\times\boldsymbol{S}_2.\end{aligned} \tag{2.33}$$

As done in Sec. 1.3 these equations can be safely orbit avareged obtaing

$$\left\langle\frac{\mathrm{d}\boldsymbol{S}_1}{\mathrm{d}t}\right\rangle = \frac{1}{2r^3}\left\{\left[4+3q-\frac{3q}{L^2}\left(k_1\boldsymbol{S}_1+\frac{\boldsymbol{S}_2}{q}\right)\cdot\boldsymbol{L}\right]\boldsymbol{L}+\boldsymbol{S}_2\right\}\times\boldsymbol{S}_1, \tag{2.34}$$

$$\left\langle\frac{\mathrm{d}\boldsymbol{S}_2}{\mathrm{d}t}\right\rangle = \frac{1}{2r^3}\left\{\left[4+\frac{3}{q}-\frac{3}{L^2}\left(\boldsymbol{S}_1+\frac{k_2}{q}\boldsymbol{S}_2\right)\cdot\boldsymbol{L}\right]\boldsymbol{L}\ +\boldsymbol{S}_1\right\}\times\boldsymbol{S}_2, \tag{2.35}$$

$$\begin{aligned}\left\langle\frac{\mathrm{d}\boldsymbol{L}}{\mathrm{d}t}\right\rangle = \frac{1}{2r^3}\Bigg\{&\left[4+3q-\frac{6q}{L^2}\left(k_1\boldsymbol{S}_1+\frac{\boldsymbol{S}_2}{q}\right)\cdot\boldsymbol{L}\right]\boldsymbol{S}_1 + \\ &+\left[4+\frac{3}{q}-\frac{6}{L^2}\left(\boldsymbol{S}_1+\frac{k_2}{q}\boldsymbol{S}_2\right)\cdot\boldsymbol{L}\right]\boldsymbol{S}_2\Bigg\}\times\boldsymbol{L}.\end{aligned} \tag{2.36}$$

Setting $k_1 = k_2 = 1$ one reobtain Eqs. (1.28)–(1.33). In that limit, it has been demonstrated by Racine (2008) that the spin parameter $\chi_{\rm eff}$ is a constant of motion for the orbit average spin-precession equations up to the 2PN order. Practically, this means that

$$\frac{\mathrm{d}\chi_{\rm eff}}{\mathrm{d}t} \propto \left[\left(\frac{\mathrm{d}\boldsymbol{S}_1}{\mathrm{d}t}+\frac{1}{q}\frac{\mathrm{d}\boldsymbol{S}_2}{\mathrm{d}t}\right)\cdot\hat{\boldsymbol{L}} + \left(\boldsymbol{S}_1+\frac{\boldsymbol{S}_2}{q}\right)\cdot\frac{\mathrm{d}\hat{\boldsymbol{L}}}{\mathrm{d}t}\right] = 0. \tag{2.37}$$

Moreover, since there are no dependencies on the orbital separation, $\chi_{\rm eff}$ also remains constant at 2.5PN order when radiation–reaction contributions enter the equations. The presence of this conserved quantity is essential because it reduces the problem's dimensionality, as shown in Sec. 1.3. Specifically, it enables, through $\delta\chi$, to compress the spin–precession equations into a single one (see Eq. (1.34)), which can be integrated

semi-analytically. Finally, $\chi_{\rm eff}$ remaining constant throughout the entire evolution of the BH binaries is the most accurately measured spin-related parameter through GWs.

In the more general case where $k_{1,2} > 1$, the dynamics become much less straightforward because $\chi_{\rm eff}$ is no longer conserved. This results in three main points:

(i) In principle, spin dynamics cannot be reduced to a single equation anymore, but require an additional evolution equation for $\chi_{\rm eff}$, although a new constant of motion can be identified;

(ii) With multiple fundamental quantities evolving on the precession timescale, even the definition of this timescale becomes complex if one aims to retain the definition given in Eq. (1.35);

(iii) The preferred spin-related parameter considered the "best measured" is no longer well-defined, as all those presented so far evolve over time.

Fortunately, Nature did not run out of constants of motion, and we were able to identify a substitute for $\chi_{\rm eff}$ to address the spin-precession problem in *generic* compact-object binaries. This new conserved quantity, $\chi_{\rm cons}$, is constructed to depend only on θ_1 and θ_2, similarly to $\chi_{\rm eff}$ and $\delta\chi$, and it reduces to $\chi_{\rm eff}$ both in the BH limit and as $r \to \infty$, where the bodies behaves like point particles and the matter effects should vanish. Thus resulting in the following expression

$$\chi_{\rm cons} = \sqrt{r} - \sqrt{\left(\sqrt{r} - \chi_{\rm eff}\right) + \chi_*^2}\,, \tag{2.38}$$

where

$$\chi_* = \frac{\sqrt{(k_1-1)(\chi_1\cos\theta_1)^2 + (k_2-1)(q\chi_2\cos\theta_2)^2}}{1+q}. \tag{2.39}$$

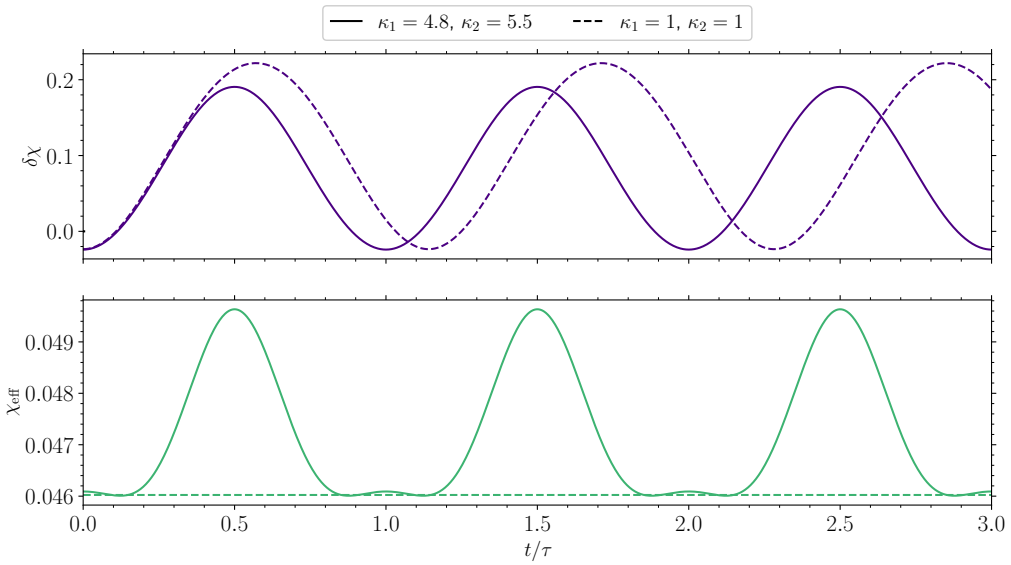

Figure 2.9: Time evolution of the weighted spin difference $\delta\chi$ (top) and $\chi_{\rm eff}$ (bottom) for two representative compact object binaries: a BH binary and a NS binary. These systems have mass ratio $q = 0.8$, spin magnitudes $\chi_1 = 0.7$ and $\chi_2 = 0.4$, initial spin orientations $(\theta_1, \theta_2, \Delta\Phi) = (\pi/2, 9\pi/20, -\pi/6)$, orbital separation $r = 100M$, and either $k_1 = 4.8$ $k_2 = 5.5$ (dashed, both the objects are NSs) or $k_1 = k_2 = 1$ (solid, both the objects are BHs).

With this new quantity, it can be shown that the entire spin-precession dynamics can once again be compressed into the single derivative of $\delta\chi$, where the previous dependence on $\chi_{\rm eff}$ is now replaced by $\chi_{\rm cons}$. The treatment of spin precession in generic compact-object binaries was initially studied, although with significant approximations to address the lack of a constant of motion in the problem, in Ref. [134]. Our complete formalism, along with a more detailed derivation of $\chi_{\rm cons}$ and an examination of the dynamics, will be presented elsewhere in a forthcoming publication.

In Fig. 2.9, we present a preliminary example of the evolution on the precession timescale of $\delta\chi$ and $\chi_{\rm eff}$ for two compact object binaries. We consider two systems with the same parameters, except for the values of k_1 and k_2, thus obtaining a NS and a BH binary. In the former case, we set $k_1 = 4.8$ and $k_2 = 5.5$, obtained considering

the APR equation of state [135] and selecting two NSs of masses $m_1 = 1.4M_\odot$ and $m_2 = 1.3M_\odot$. For these two NSs, we estimate the tidal deformabilities $\lambda_1 \approx 248$ and $\lambda_2 \approx 392$, and then converted into k_1 and k_2 via quasi-universal equation of state independent relations [136]. For the BH binary, it naturally follows that $k_1 = k_2 = 1$. For both systems, we set $q = 0.8$, $\chi_1 = 0.7$, $\chi_2 = 0.4$, initial spin inclination angles $(\theta_1, \theta_2, \Delta\Phi) = (\pi/2, 9\pi/20, -\pi/6)$ and we evolve $\chi_{\rm eff}$ and $\delta\chi$ over 3 periods, $\tau_{\rm prec}$, considering a fixed orbital separation $r = 100M$. As observed, the two evolutions of $\delta\chi$, which parameterize that of spin angles, differ since the right-hand side of Eqs. (2.34)–(2.36) changes with the value of the spin-induced quadrupolar constants. In turn, $\chi_{\rm eff}$, when NSs are involved, does evolve on the precession timescale, unlike in the BH scenario (see Eq. (2.37)). Finally, it is worth noting that the phenomenology we examined in the preliminary stage of this work is more diverse and complex than that of BHs, and the parameter space where precession can occur is consequently more convoluted. It seems that the analytical simplifications achieved for BHs by [40] are mostly lost, leaving us to depend on numerical integration. Despite this, $\chi_{\rm cons}$ should serve as the new "best-measured" spin-related quantity for binaries that contain at least one NS or another non-BH object. This hypothesis still needs to be thoroughly tested, with a campaign of parameter estimation on simulated events, which is currently ongoing. Based on the results presented in Sec. 2.2, extending this formalism to eccentric orbits should be straightforward.

Chapter 3

Residual eccentricity as a systematic uncertainty on the formation channels of binary black holes

Abstract

Resolving the formation channels of merging binary black holes is a key goal in gravitational-wave astronomy. Orbital eccentricity is believed to be a precious tracer of the underlying formation pathway but is largely dissipated during the typically long inspiral between black hole formation and merger. As a result, most gravitational-wave sources are expected to enter the sensitivity windows of current detectors in configurations consistent with quasi-circular orbits. In this chapter, we examine the impact of "negligible" residual eccentricity—lower than current detection capabilities—on inferring the formation history of binary black holes, with a particular focus on their spin orientations. We trace the evolution of both observed and synthetic gravitational-wave events backward in time, resampling their residual eccentricities to values below the detectability threshold.

Eccentricities in band as low as $\sim 10^{-4}$ can lead to significant biases when reconstructing the spin directions, especially in the case of loud, highly precessing systems. Residual eccentricity thus acts like a systematic uncertainty for our astrophysical inference. As a mitigation strategy, one can marginalize the posterior distribution over the residual eccentricity using astrophysical predictions.

Summary

In this chapter, we apply the formalism introduced in Chap. 2 to demonstrate that residual and non-detectable eccentricity is a source of systematics that can affect all astrophysical analyses of BH binaries that rely on reconstructing spin evolution history. In Sec. 3.2, we show this by measuring the difference between back-propagated posteriors of spin directions, considering the effect of non-detectable eccentricities at detection for both real and simulated GW events. In Sec. 3.3, we present our results in terms of the bias induced and propose a strategy to marginalize over residual eccentricity using astrophysical predictions; in Sec. 3.4, we discuss the implications of our findings. Throughout this chapter, we adopt natural units with $G = c = 1$.

The material presented in this chapter has been published in Fumagalli *et al.* (2024).

3.1 Introduction

Inferring the formation and evolutionary processes of merging stellar-mass BHs is one of the most pressing questions in modern high-energy astrophysics (see Sec. 1.2). LIGO, Virgo, and KAGRA (LVK) are delivering hundreds of GW detections [137, 138,

139, 4, 58] and, despite some initial optimism, the "formation-channel" problem is still far from solved [62, 63, 64, 65, 66, 67]. As pointed out in Sec. 1.2, BHs are simple objects in general relativity. This implies that we have a limited number of observables at our disposal, notably masses, spins, merger rates, and potentially the orbital eccentricity. Among these, spin directions and eccentricity are believed to be clean indicators of formation mechanisms, with large spin misalignments and large eccentricities pointing to dynamical assembly in densely populated environments.

As shown in Chap. 2, precession and orbital eccentricity are deeply intertwined. From a signal perspective, they both introduce on timescales that are longer than that of the orbit [29, 30, 140]. Such waveform features can be comparable, and isolating the two effects in current GW data presents challenges, at least for sufficiently short signals [53]. As for the binary evolution, couplings between the spin and eccentricity sectors of the binary dynamics introduce a non-trivial phenomenology. Specifically, sources formed with identical parameters but different eccentricities might enter the LVK band with spin evolution patterns that are considerably different (see Fig. 2.5).

This interplay between spins and eccentricity requires careful consideration when reconstructing the history of BH binaries from their parameters inferred from their GW signals. Propagating spin directions from formation to detection [35, 40] is crucial to transfer astrophysical predictions to the regime where sources are observable [77, 78, 69], thus allowing for a meaningful comparison with the data. The reverse operation, "back-propagating" binaries from detection to formation, has key applications in single-event inference [118, 117, 141], population studies [118, 142], and archival searches for, say, the LISA mission [143, 144, 145, 146]. In this Chapter, we show that eccentricity is a source of systematics that might affect, perhaps significantly, these downstream applications.

The BH binaries observed by LVK have been consistently reported to be quasi-circular [147, 148], perhaps with a few exceptions [55, 56, 57]. This is not surprising, as leading-order PN effects tend to remove eccentricity from binary systems on a timescale that is shorter than that of the inspiral itself (see Ref. [16] and Sec. 2.2.2), leading to quasi-circular mergers even for systems that initially formed on highly eccentric orbits. Current ground-based interferometers are capable of detecting eccentricities as low as $e_{\rm thr} \simeq 0.05$ for GW150914-like binaries [52], meaning that binaries entering the sensitivity band of our instruments with eccentricities lower than this threshold will be reported as quasi-circular. In reality, GW sources have some residual eccentricity $e_{\rm res} < e_{\rm thr}$ which cannot be captured. For typical astrophysical environments, current models predict values of $e_{\rm res} \lesssim 10^{-8}$ for field binaries and $\sim 10^{-7} \lesssim e_{\rm res} \lesssim 10^{-4}$ for the majority of binaries formed in clusters (cf. Sec. 3.3.3 below). For binaries that are assembled dynamically, models also predict a small fraction of sources merging with $e_{\rm res} > e_{\rm thr}$ which, if detected, are poised to be highly informative [70].

Quasi-circular orbits act as dynamical attractors for the forward evolution of BH binaries [16], which unfortunately implies they act as repulsors where sources are back-propagated: for binaries on eccentric orbits, small variations of their parameters at GW detection imply large variations at BH formation. As suggested in Chap. 2, this issue is particularly concerning when considering the spin directions.

Therefore, do residual, below-threshold eccentricities significantly affect our inference on the spin of BH binaries and thus their formation mechanism? How can this source of systematic be mitigated? What are the consequences when inferring the formation channels of GW sources?

We tackle these questions by applying the PN formalism presented in Secs. 1.3 and 2.2 to real LVK observations, synthetic GW events, and predictions from astrophys-

ical population-synthesis simulations. For each event, instead of making the common assumption that $e_{\rm res} = 0$, we resample the residual eccentricity $e_{\rm res} < e_{\rm thr}$ and back-propagate the resulting spin evolution to a common large separation. We compare the resulting spin distributions against those obtained assuming quasi-circularity for the entire inspiral. For events up to GWTC-3 [137, 138, 139, 4], we find that residual eccentricity introduces a rather mild systematic effect. This is due to the large uncertainties in the spin directions, as well as the weak or absent evidence of spin precession in most of the signals. We are safe, for now. Using a set of synthetic injections [101] with higher signal-to-noise ratios (SNR) and prominent two-spin effects, we observe severe divergences between the eccentric and quasi-circular spin predictions. Unaccounted (and, at present, unaccountable) eccentricity at detection can introduce substantial variation in our inference of spins at BH binary formation, which implies that residual eccentricity is effectively a systematic that one should take into account when inferring the origin of GW events. We show that astrophysical models of BH binary formation [103, 149, 150] can be used to heuristically "marginalize" over this systematic, thereby mitigating its impact.

3.2 Back propagation

We consider the same binary setting used in Chap. 2 and presented in Sec. 1.3. In this chaper we consider the spin information to be condensed, a part from the spin angles θ_1 and θ_2, into the parameters $\chi_{\rm eff}$ (which includes information about the aligned components of the spins [32]) and $\chi_{\rm p}$ (which instead captures spin precession [151, 152]) along with spin angles θ_1, and θ_2. In the following, we use the "average" definition of $\chi_{\rm p}$ put forward in Refs. [152, 101]. In particular, one has $\chi_{\rm p} \in [0, 2]$ where the lower bound implies aligned spins and $\chi_{\rm p} > 1$ implies that both spins are precessing. Such definition

can be trivially extended to eccentric orbits using the mapping detailed in Sec. 2.2. We evolve binaries along their inspiral using the precession-averaged PN approach of Chap. 2. Posterior samples are provided at the reference GW frequency $f_{\rm ref} = 20$ Hz, with the exception of GW190521 where instead $f_{\rm ref} = 11$ Hz [138]. From these, we calculate the semi-major axis a using the PN expression reported in Eq. (4.13) of Ref. [30], which results in separations of $\mathcal{O}(10M)$. This conversion neglects the presence of eccentricity, which is appropriate for $e_{\rm res} < e_{\rm thr}$.

3.2.1 Residual eccentricity

Residual eccentricity in band might go unnoticed. We capture this effect by assigning each posterior sample a new value of the eccentricity that is below the distinguishability threshold. In the following, we pursue two strategies:

(i) For a rather agnostic approach, we consider thermal distributions $f(e) \propto e$ which naturally arise in statistical physics. We set $e \in [0, e_{\rm max}]$ such that $e_{\rm max} = 0$ corresponds to assuming binaries that evolved on quasi-circular orbits since formation. In the following, we use $e_{\rm max} = 10^{-4}, 10^{-3}, 10^{-2}$ such that all samples have an eccentricity $e \leq e_{\rm max} < e_{\rm thr} \simeq 0.05$ in band. Note that eccentricities are resampled at $f_{\rm ref} = 20$ Hz (just in the case of GW190521, we resampled eccentricity at $f_{\rm ref} = 11$ Hz) while Ref. [52] quotes the threshold $e_{\rm thr} \sim 0.05$ at 10 Hz. We check that our resampled values of $e_{\rm res}$ are lower than $e_{\rm thr}$: using Peters' equations [16], a binary $e = 10^{-2}$ at 20 Hz reaches $e \sim 0.02$ at 10 Hz. For a more in-depth study, one should consider an eccentricity threshold that depends on the binary parameters (for instance, it is easier to infer the eccentricity for binaries with lower masses because they complete more cycles in band [153]). We leave this to future work.

(ii) For a more astrophysically motivated approach, we attempt a direct modeling of the residual eccentricity predicted by state-of-the-art population-synthesis codes. We make use of simulations of both binaries formed in isolation [154] and binaries assembled dynamically in dense stellar clusters [150, 71]. We draw eccentricities directly from their distributions as predicted at GW detection; see Sec. 3.3.3 for details. In particular, distributions are truncated at $e_{\rm res} < e_{\rm thr}$. This mimics a scenario where highly eccentric sources predicted can be identified as such and are not affected by the systematic uncertainty targeted here.

Given this initial configuration, we propagate binaries backward in time until the separation reaches $a = 10^4 M$. This is rather conservative as BH binary formation typically happens at separations as large as $\sim 10^6 M$ [155, 156, 150]. If the residual eccentricity in band is $\neq 0$, binaries will reach this large separation with orbits that are considerably more eccentric; this is due to the repulsive character of Peters' equations. When back propagating from eccentricities $e_{\rm res}$ of $\mathcal{O}(10^{-2})$, the resulting eccentricities at $a = 10^4 M$ can be larger than 0.6, which was quoted as a conservative limit for the validity of our formalism [85]. Extending the applicability of PN integrations to the high-eccentricity regime is a conceptual problem addressed in Chap. 4. For simplicity, here we nonetheless use the Peters' equations for all our sources, which is in line with common practice in the astrophysical community.

3.2.2 Gravitational-wave signals

We consider both LVK observations and synthetic injections. Together, these sources cover a broad range of SNRs and degrees of spin precession.

(i) We consider 69 binary BH mergers as reported in the past GWTC catalogs

[137, 138, 139, 4] (the inclusion of GWTC-4.0 [58] will be addressed in future work), selecting events with false alarm rate $< 1\,\mathrm{yr}^{-1}$ and astrophysical probability $p_{\rm astro} > 0.5$. We use samples labeled as Mixed-Cosmo, which combine results from the IMRPhenomXPHM [90] and SEOBNRv4PHM [157] waveform approximants. For event GW200129_065458, we also consider posterior samples obtained with NRSur7dq4 [158] from Ref. [5], which present a much stronger evidence for spin precession (see also Ref. [159] for similar conclusions and Ref. [109] for caveats related to data quality).

(ii) We also use 100 publicly available [3] software injections which specifically target highly precessing systems. These were first presented in Figs. 4 and 5 of Ref. [101]. The parameters of these sources are distributed by reweighting the uninformative prior used in LVK parameter estimation in favor of a uniform distribution in $\chi_{\rm p} \in [0, 2]$ and applying an SNR threshold of 20. In particular, these binaries have masses $m_{1,2} \in [5, 100] M_\odot$ constrained to $q \in [1/8, 1]$ and $\mathcal{M}_c \in [10, 60] M_\odot$ (where $\mathcal{M}_c$ is the detector-frame chirp mass), spins $\chi_{1,2} \in [0, 0.99]$, and luminosity distances $D_L \in [100, 5000]$ Mpc. Source are injected and recovered with the IMRPhenomXPHM [90] approximant, assuming detector performances representative of the 4th observing run of LVK and neglecting non-stationary noise realizations (for details see Ref. [101]).

Crucially, all these sources, both real and synthetic, have been analyzed assuming BHs on quasi-circular orbits. We do not have posterior distributions for the residual eccentricity in band, which thus acts as a systematic uncertainty.

	1σ	2σ	3σ	4σ	5σ	...	10σ
$d_{\rm H}$	0.343	0.627	0.822	0.930	0.978		$\sim 1-10^{-6}$

Table 3.1: Values of the Hellinger distance for two identical Gaussian distributions separated by an increasing number n of standard deviations σ.

3.2.3 Hellinger distance

Quantifying the impact of residual eccentricities requires a notion of distance between probability distributions. Among the many available options [160], we opt for the Hellinger distance [161]. This is defined as

$$d_{\rm H}(p,q) = \sqrt{1 - \int \sqrt{p(x)q(x)}\, dx}\,, \tag{3.1}$$

where p and q are probability density functions of a (possibly multi-dimensional) variable x. In our case, these are the back-propagated posteriors obtained assuming either quasi-circularity or resampled eccentricities, respectively. We integrate over $x = (\cos\theta_1, \cos\theta_2)$ and have verified that $x = \chi_{\rm p}$ yields results that are largely indistinguishable. We evaluate probability density functions using Kernel Density Estimation and compute the integral in Eq. (3.1) via Monte Carlo. The Hellinger distance has the desirable properties of being symmetric, i.e. $d_{\rm H}(p,q) = d_{\rm H}(q,p)$, and defined in $[0,1]$ such that $d_{\rm H} = 0$ implies that the two distributions are identical and $d_{\rm H} = 1$ implies that their supports are disjoint. For some intuition, one can convert Hellinger-distance values into σ levels by considering two one-dimensional Gaussians separated by n standard deviations. The result is

$$d_{\rm H}\big[\mathcal{N}(\mu,\sigma), \mathcal{N}(\mu + n\sigma, \sigma)\big] = \sqrt{1 - \exp\left(-\frac{n^2}{8}\right)}\,. \tag{3.2}$$

Some evaluations are reported in Table 3.1.

3.3 Systematic uncertainty

3.3.1 A few examples

The top panels of Fig. 3.1 show posterior distributions of the spin angles (θ_1, θ_2) and the effective precession parameter $\chi_{\rm p}$ for the synthetic event labeled as `uni_88` in the dataset of Ref. [3]. This signal was handpicked for illustrative purposes because it has the largest Hellinger distance between the quasi-circular and eccentric reconstructions. This is a loud (SNR $\simeq$ 118) system with BHs of detector-frame masses $m_1 = 49.5^{+1.2}_{-1.8} M_\odot$, $m_2 = 45.3^{+1.1}_{-1.1} M_\odot$ and spin magnitudes $\chi_1 = 0.95^{+0.03}_{-0.06}$, $\chi_2 = 0.94^{+0.04}_{-0.07}$ (hereafter we report medians and 90% credible intervals). We show posterior distributions at detection ($f_{\rm ref} = 20$ Hz) as well as those resulting from our back-propagation procedure ($a = 10^4 M$) assuming residual eccentricities extracted from a thermal distribution truncated at some $e_{\rm max}$. An animated version of Fig. 3.1 is available at www.davidegerosa.com/spinprecession and shows the evolution of such posteriors as a function of a.

As the adopted residual eccentricity increases, the back-propagated posterior distributions show larger deviations from the expected circular predictions, possibly leading to biased estimations of the spin parameters. For this event, the Hellinger distance between the back-propagated posterior obtained with $e_{\rm max} = 10^{-2}$ and its circular counterpart with $e_{\rm max} = 0$ is ~ 0.79 (i.e. $\gtrsim 2\sigma$ levels).

It is informative to compare the locations of the back-propagated distributions against those at detection as a function of the residual eccentricity. When projected in the $(\cos\theta_1, \cos\theta_2)$ plane, all distributions lie roughly on the same diagonal line; this

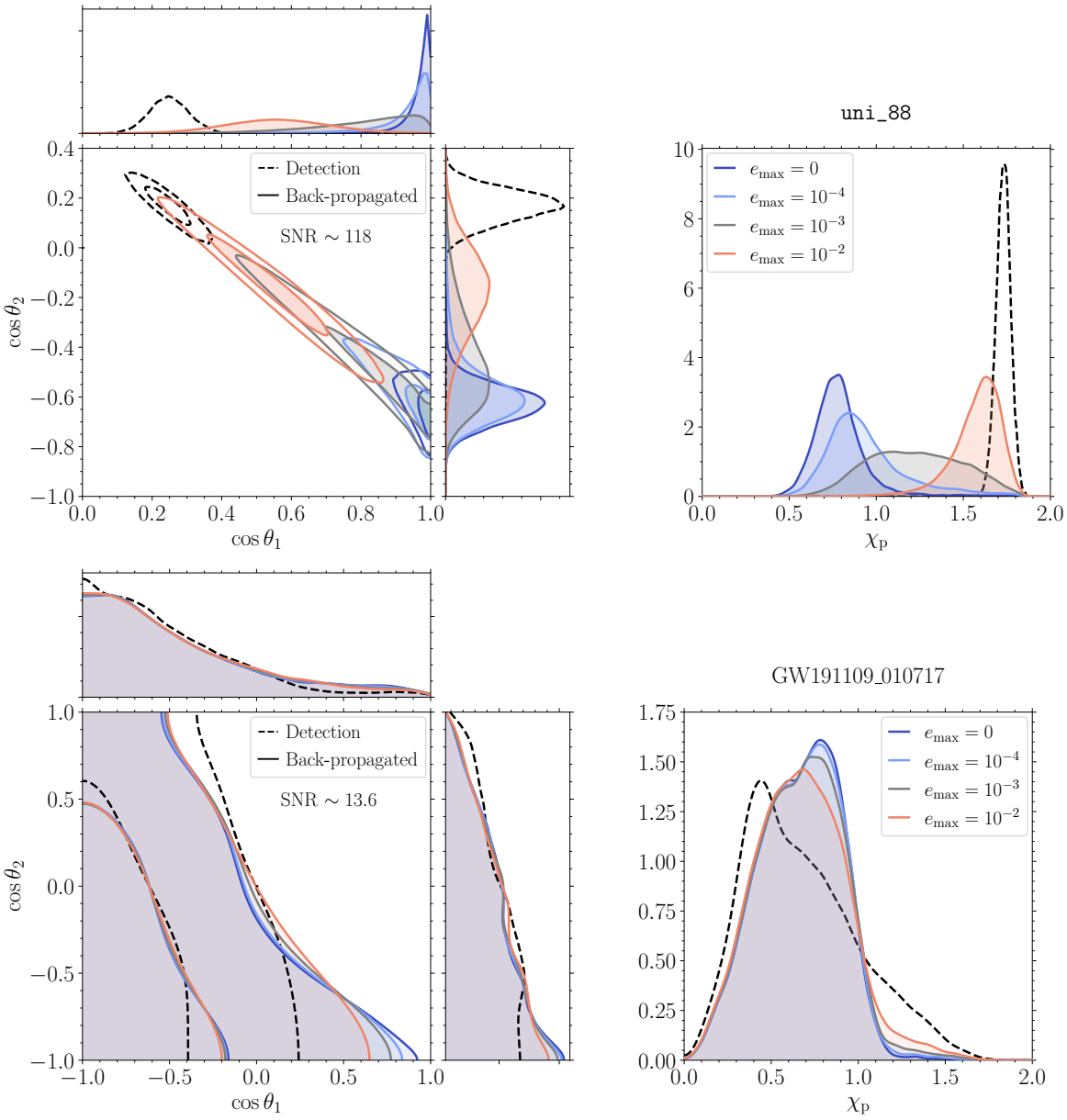

Figure 3.1: Back-propagated posterior distributions assuming both eccentric and quasi-circular configurations. The top panels show results for the synthetic signal labeled `uni_88` in the dataset of Ref. [3]; the bottom panel shows event GW191109_010717 [4]. In both cases, the left panels show the joint posterior distribution of the spin orientations (θ_1, θ_2) and the right panels show the posterior distribution of χ_p. Dashed curves show the distributions at detection ($f_{\rm ref} = 20$ Hz); solid curves are obtained by back-propagating posterior samples to $a = 10^4 M$. The dark blue distributions ($e_{\max} = 0$) assume sources evolved on quasi-circular orbit throughout their inspiral. The other curves assume some residual eccentricity at detection. These are drawn from a thermal distribution $f(e) \propto e$ truncated at $e_{\max} = 10^{-4}$ (light blue), 10^{-3} (gray), and 10^{-2} (red). Contours in the 2-dimensional distributions on the left correspond to 50% and 90% credible intervals. An animated version of this figure is available at www.davidegerosa.com/spinprecession.

is because $\chi_{\rm eff}$ is a constant of motion for both the eccentric and the quasi-circular problem [32] (at least at 2PN in spin precession, which is the order considered here). But crucially, larger residual eccentricities imply spin orientations that are closer to those at detection.

While this might seem counterintuitive at first, it is a direct consequence of the PN equations of motion [42, 85]. The evolution of the spin orientations depends on the semi-major axis a and eccentricity e through the orbital angular momentum L. This acts much like a time coordinate, with sources evolving from large L to small L. From the Newtonian scaling $L \propto \sqrt{a(1-e)}$, eccentric binaries have a smaller angular momentum than circular binaries for a given value of a. The posteriors shown in Fig. 3.1 are naturally ordered by angular momentum, with the eccentric back-propagated posteriors seated between the back-propagated circular posteriors (which have the largest orbital angular momentum) and the posteriors at detection (which have the smallest orbital angular momentum). The bottom panels of Fig. 3.1 show back-propagated posteriors for the LVK event GW191109_010717; once more, this system was chosen for its most pronounced differences between eccentric and circular back-propagated results across the considered GW catalog. GW191109_010717 has an SNR of ~ 13.6 and is consistent with a binary BH with $m_1 = 81^{+13}_{-9} M_\odot$, $m_2 = 60^{+16}_{-17} M_\odot$, $\chi_1 = 0.65^{+0.32}_{-0.58}$, and $\chi_2 = 0.82^{+0.15}_{-0.57}$. Although subtler, the same features we discussed for our simulated system are also present for GW191109_010717; this is, however, characterized by much larger uncertainties (the SNR is about 10 times lower). In this case, we report a distance $d_{\rm H} \sim 0.01$ between back-propagated posteriors with $e_{\rm max} = 10^{-2}$ and $e_{\rm max} = 0$. Overall, this shows that, for the events considered in this chapter, the systematic bias induced by neglecting residual eccentricity in band is mild. It might, however, become important for exceptionally loud events [162] and/or with the next leap in sensitivity of our detectors.

Despite the promising evidence for precession in GW200129_065458 [5, 159], we find $d_{\rm H} \sim 10^{-5}$ between back-propagated posteriors with $e_{\rm max} = 10^{-2}$ and $e_{\rm max} = 0$ when using the samples of Ref. [5]. This is likely attributed to the largely unconstrained posterior for the secondary spin.

3.3.2 Parameter-space exploration

We now present a broader exploration of the parameter space using the Hellinger distance (Sec. 3.2.3) as our summary statistic. Figure 3.2 shows the values of $d_{\rm H}$ across all the signals of Sec. 3.2.2, including both real and synthetic events. We compute Hellinger distances between the three eccentric back-propagated distributions $e_{\rm max} = 10^{-2}, 10^{-3}, 10^{-4}$ and the circular case $e_{\rm res} = e_{\rm max} = 0$. The distance is computed over $x = (\cos\theta_1, \cos\theta_2)$ and plotted against the median value of $\chi_{\rm p}$ at detection.

The Hellinger distance between our circular and eccentric back-propagated prediction increases with $\chi_{\rm p}$, indicating that the systematic uncertainty associated with residual eccentricity is strongly correlated with the amount of precession in the signal. More trivially and as already illustrated in Fig. 3.1, we find that the distance increases with $e_{\rm max}$.

On top of these main trends, Fig. 3.2 shows substantial variability, even across several orders of magnitude in $d_{\rm H}$. This is not surprising given the high dimensionality of the BH binary parameter space and our sparse coverage. For a given value of $\chi_{\rm p}$ and $e_{\rm max}$, we find that sources at lower (higher) SNR tend to have larger (smaller) values of $d_{\rm H}$, corresponding to the regime where statistical systematic uncertainties dominate the error budget. This can also be seen by comparing the top and bottom panels of Fig. 3.1.

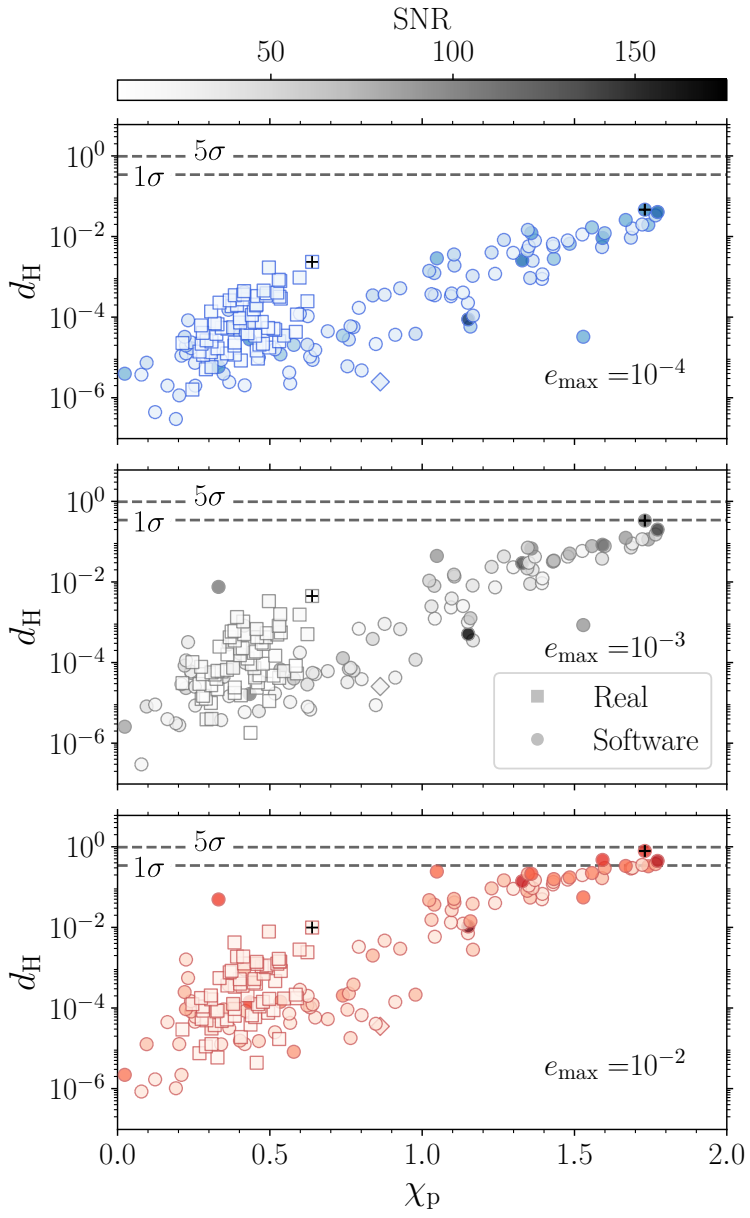

Figure 3.2: Hellinger distances between circular and eccentric back-propagated posterior distributions of $(\cos\theta_1, \cos\theta_2)$ as a function of the median value of $\chi_{\rm p}$ at detection. We consider 69 real events detected by LVK (squares) and 100 synthetic signals (circles). Diamonds mark results obtained using the posterior samples of Ref. [5] for event GW200129_065458. Crosses indicate the events used in Figs. 3.1 and 3.4. Panels and colors refer to different assumptions for the residual eccentricity in band. This is extracted from a thermal distribution truncated at $e_{\rm max} = 10^{-4}$ (blue, top), $e_{\rm max} = 10^{-3}$ (grey, middle), and $e_{\rm max} = 10^{-2}$ (red, bottom). Dashed horizontal lines mark the Hellinger distances values corresponding 1 and 5 σ-levels (cf. Table 3.1).

3.3.3 Marginalization with astrophysical models

The use of thermal distributions truncated at $e_{\rm max}$ in the previous sections was arbitrary. We now present a more motivated strategy that makes direct use of state-of-the-art population-synthesis predictions. We interpret this as an "astrophysical marginalization" over the residual eccentricity: the back-propagated posteriors on the spin directions one infers are broader than one would obtain by naively assuming that binaries evolved on ideal quasi-circular orbits for their entire inspiral.

Eccentricity at merger is a distinct signature of binaries that formed in dynamical environments, notably dense stellar clusters. We use predictions obtained with RAPSTER [102] and CMC [149], which are two of the current state-of-the-art cluster codes in the field. These are compared against a population of BH binaries formed in isolation as predicted with the STARTRACK [154, 103] code. For binaries formed in clusters, we label sources as (i) "ejected" for BHs that merge outside of the cluster; (ii) "in-cluster" for BHs that merge inside the cluster following binary formation, and (iii) "GW capture", which also merge inside the cluster but abruptly. The RAPSTER population is generated based on the assumptions detailed in Sec. III. A of Ref. [163]. For STARTRACK, we use the population referred to as "default model" in Ref. [164]. Results from CMC are extracted from Fig. 1 of Ref. [71], which refers to detectable populations of sources at $f_{\rm ref} = 10$ Hz. We eyeball their figure and consider skewed log-normal distributions with means of $10^{-6.8}$, $10^{-5.5}$, and $10^{-2.5}$, standard deviations of 10^{-1}, and skewness parameters of 9, 6, and 1 for the ejected, in-cluster and GW capture subchannels, respectively. We therefore weight each of these distributions as reported in Table 3.2. For the RAPSTER and STARTRACK populations, eccentricity and spin distributions are provided at BH formation, which we forward-propagate to $f_{\rm ref} = 10$ Hz as described in

	Ejected		In-cluster		GW-capture	
RAPSTER	0.71	(0.70)	0.20	(0.20)	0.09	(0.002)
CMC	0.70	(0.70)	0.20	(0.20)	0.10	(0.079)

Table 3.2: Fractional contributions to the BH merger rate for the three subchannels of the dynamical formation channel using predictions from RAPSTER and CMC. Numbers in parentheses refer to sources with $e_{\rm res} < e_{\rm thr} = 0.05$.

Sec. 2.2. Finally, it is important to note that the distribution obtained with Rapster does not directly represent observable distributions, since the code does not account for selection effects affecting highly eccentric sources.

For these two codes, we post-process information for the GW detectability by considering a single LIGO instrument and an SNR threshold of 8. Signals are computed using the IMRPHENOMXPHM [90] waveform model and a noise power spectral density that is representative of the 4th observing run. This is consistent with the injections from Ref. [101] introduced in Sec. 3.2.2. We analytically marginalize over the extrinsic parameters [165, 166] as implemented in Ref. [167]. This results in a set of weights $p_{\rm det}$ for each source in our simulated populations, which is then normalized, i.e., we set $\sum_i {\rm p_{det,i}} = 1$. For RAPSTER, the fractional contributions of each of the three subchannels is reported in Table 3.2.

Figure 3.3 shows the resulting residual eccentricities at $f_{\rm ref} = 10$ Hz. The distributions predicted for each formation (sub)channel are quite distinct and differ by orders of magnitude. Predictions from the two populations of dynamically assembled binaries are in broad agreement. With the notable exception of GW captures, residual eccentricities fall well below the current distinguishability threshold $e_{\rm thr} \simeq 0.05$ [52]. Even third-generation detectors, which might reach $e_{\rm thr} \simeq 10^{-3}$ [168], will not be of much help here. In the following, we truncate the distributions of Fig. 3.3 to $e \leq e_{\rm thr} \simeq 0.05$, which mimics a scenario where highly eccentric sources can be identified as such and

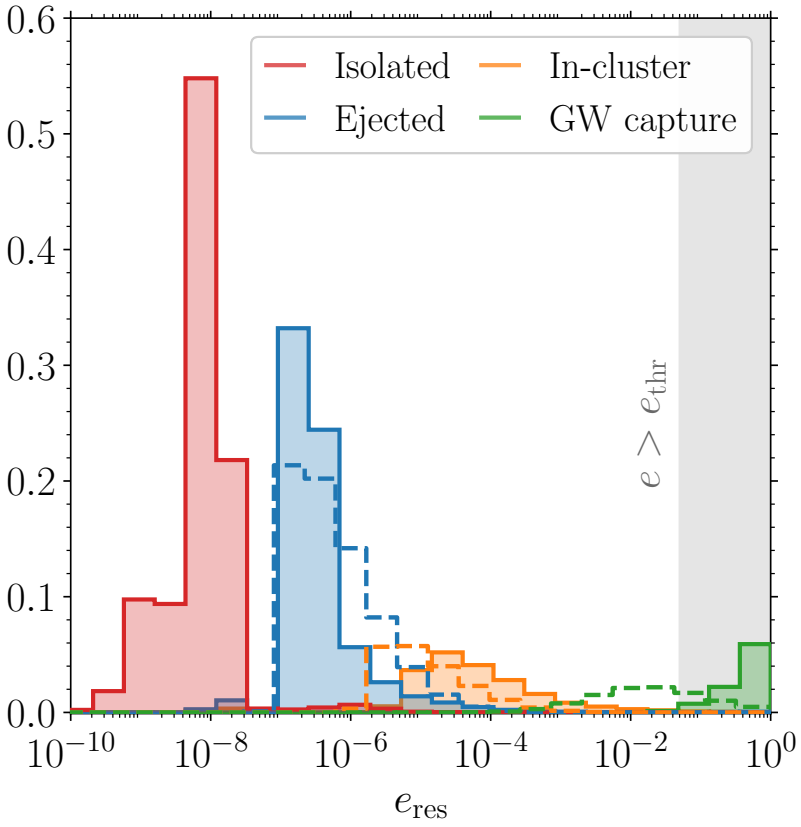

Figure 3.3: Distributions of eccentricities at the reference frequency $f_{\rm ref} = 10$ Hz for some representative astrophysical populations of BH binaries from stellar physics simulations. Distributions related to three subchannels within the two dynamically formed populations are shown in blue for ejected binaries merging outside the cluster, orange for binaries merging inside the cluster, and green for binaries formed via GW captures. For these, solid and dashed histograms show predictions from the Rapster and CMC codes, respectively. The isolated-binary population from StarTrack is shown in red. The grey area to the left marks systems with eccentricity larger than the resolvability threshold, here set to $e_{\rm thr} = 0.05$. Binaries are weighted by their GW detectability, and the resulting histograms are normalized to the cumulative detection probability, i.e., the sum of the bin heights for the isolated and dynamical channels is equal to 1. The contributions provided by each of the subchannels are reported in Table 3.2.

thus do not pollute our inference of binaries that appear quasi-circular. Note that Fig. 3.3 is likely to overestimate the importance of highly eccentric sources because of the related difficulties with estimating GW detectability; this partly motivates the difference between CMC and RAPSTER for the GW-capture subchannel.

Given these predictions, we perform the same operation discussed in Sec. 3.3 while drawing residual eccentricities from the distributions of Fig. 3.3. Notably, this does not provide an exhaustive picture of all possible eccentric mergers. Eccentric binaries are expected to form in environments other than globulars, such as active galactic nuclei [169], different types of star clusters [170], and hierarchical triples [171]. For clarity, we limit our analysis to the populations described above but stress that the methods presented here can be straightforwardly applied to other predictions.

Figure 3.4 shows results for the same software injection considered in top panels of Fig. 3.1. We first propagate the GW posteriors forward from $f_{\rm ref} = 20$ Hz (where the injections was performed) to 10 Hz (where the residual eccentricity is provided, see above). We then back-propagate spin directions to the joint large separation $a = 10^4$M. The detailed evolution of these posteriors as a function of a is provided in an animated version of Fig. 3.4, which is available at www.davidegerosa.com/spinprecession.

The results of Fig. 3.4 should be interpreted as our best estimate of the spin orientations at (or, more accurately, close to) BH formation given the detected GW data and *assuming* a specific formation pathway. Figure 3.4 shows the same trends highlighted in Sec. 3.3.1: distributions with the lowest (largest) residual eccentricity such as isolated binaries (GW captures) have back-propagated spin directions that are further (closer) to those at detection, and the main reason is that those binaries have a larger (lower) angular momentum. When considering contributions from all the dynamical subchannels, our predictions sit close to the distributions for the ejected and

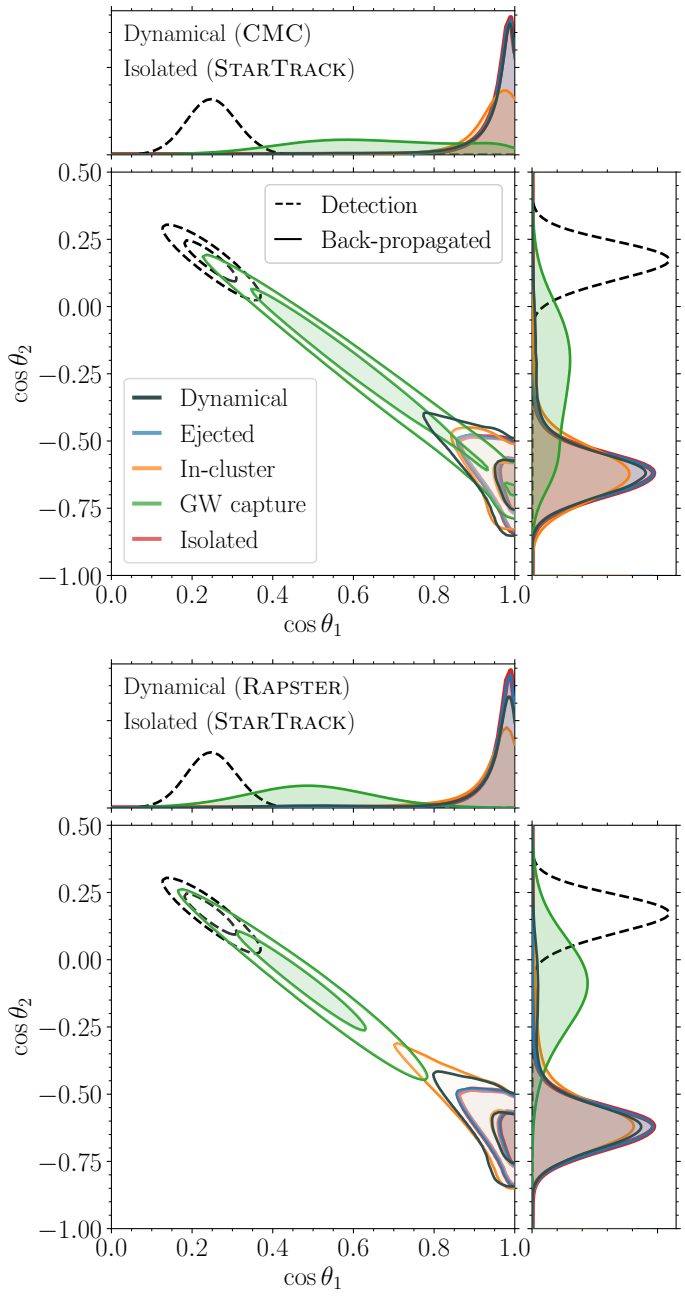

Figure 3.4: Back-propagated posteriors of the spin directions assuming astrophysically motivated distributions of residual eccentricity. We consider the SNR$\sim$ 100 synthetic signal `uni_88` from the dataset of Ref. [3] (cf. top panel of Fig. 3.1). Dashed curves show distributions at detection ($f_{\rm ref} = 20$ Hz) while solid curves show distributions at the common large separation ($a = 10^4 M$). Contours in the 2-dimensional distributions correspond to 50% and 90% credible intervals. The bottom (top) panel uses predictions for dynamically assembled BHs by the Rapster (CMC) code, see text for details. We present predictions from individual subchannels (blue, orange, green) as well as a joint prediction that considers the relative mixing fractions (dark grey). For reference, both panels report results from an isolated-star distribution from StarTrack (red), which are virtually indistinguishable from those obtained with the ejected subchannel (blue). An animated version of this figure is available at www.davidegerosa.com/spinprecession.

in-cluster subchannels because those two classes dominate the dynamical formation merger rate, as shown in Fig. 3.3 and Table 3.2 (recall that we are truncating the distribution at $e_{\rm thr}$, which further diminishes the GW-capture contribution).

Crucially, the procedure we present heavily relies on the adopted astrophysical population, which is subject to significant uncertainties. Furthermore, our results do not capture correlations between the residual eccentricity and the other parameters (say the masses or the spins) of the back-propagated signal. While our results are indicative even for fixed populations, we ultimately envision this approach to be used in synchronicity with full GW population fits, the results of which can then be repurposed to shed light on individual detections, see e.g. Ref. [161].

3.4 Conclusions

Some of the key observables in GW astronomy are time-dependent, i.e., their values change, sometimes significantly, as sources inspiral. Among these are the spin directions and the orbital eccentricity. Capturing their coupled evolution between BH formation and GW detection is important for an unbiased reconstruction of the formation pathway of stellar-mass BH binaries. Current ground-based detectors are not able to distinguish eccentricities in BH binaries which are $\lesssim 0.05$ at 10 Hz. Those sources are thus typically reported as compatible with binaries on quasi-circular orbits.

Eccentricity and spin inclinations are coupled (see Chap. 2) and, as illustrated in this chapter, mismodeling in the former at detection translates into biased distributions of the latter at BH formation. Residual eccentricity is a systematic uncertainty for the spin directions, which should be considered in addition to the statistical uncertainty due to detector noise. In particular, our study illustrates that:

(i) The systematic bias on the spin directions due to residual eccentricity increases with both the residual eccentricity itself as well as the amount of spin precession in the signals. This illustrates that this effect is indeed due to couplings between the precession and eccentricity sectors of the BH dynamics.

(ii) For the LVK events considered in this chapter, the systematic uncertainty due to residual eccentricity is subdominant compared to the statistical uncertainty of the spin directions ($d_{\rm H} \lesssim 0.01$).

(iii) The situation is reversed for putative sources with SNR ~ 100 and precessing spins, which might present spin posteriors at BH formation that are essentially disjoint from those obtained assuming quasi-circular orbits ($d_{\rm H} \sim 0.8$).

Residual eccentricity influences not only the spin predictions of individual events but also those of population-level analyses, which we plan to investigate in future work. Features in the inferred population of the BH spins are used to constrain specific mechanisms behind the assembly of BH binaries such as supernova kicks, tidal interactions, mass transfer, and even the symmetry of the environment [77, 80, 172, 125, 173, 174, 175, 176, 67, 177, 164]. GW population fits that include spin directions are now performed after binaries have been back-propagated to past time infinity (i.e. $f_{\rm ref} = 0$ Hz) *assuming quasi-circular orbits* [118, 117, 142, 178]. The evolution of eccentric binaries to past time infinity is still an open problem because the commonly employed averaging techniques [16, 85] are expected to break down [40]. In this chapter, we sidestepped the issue by halting our evolution at a large but finite separation, $a = 10^4$M. Extrapolating from what we presented here, we speculate that the importance of the systematic bias due to residual eccentricity might increase if evolutions are extended to larger separations, though we stress this requires the development of

an appropriate PN-evolution strategy (see Chap. 4) in conjunction with a population fit in hierarchical Bayesian statistics.

Residual eccentricity might also impact archival searches of stellar-mass BH binaries in LISA data. It has been argued that ground-based detections of merging binaries might be used to "know where to look for," thus digging deeper into the LISA noise and increasing the sensitivity of our searches [143, 145]. This chapter shows that residual eccentricity is an important caveat to this statement; we will not really know where to look for.

The uncertainty is further exacerbated by the known degeneracy between eccentricity and time to merger [179]. More broadly, residual eccentricity will have an impact whenever the spin directions are considered; this systematic effect will become more severe for larger SNRs, notably including massive BHs observed by LISA [180] and stellar-mass BHs observed by 3rd-generation ground-based observatories [181].

Still operating at the single-event level, we explored a potential strategy to quantify the systematic error due to residual eccentricity when inferring the BH spin directions, which relies on pre-computed astrophysical distributions. While admittedly model-dependent, the procedure highlighted in this chapter mitigates the eccentricity systematics by folding astrophysical modeling into the spin-orientation inference. The adopted astrophysical distribution of $e_{\rm res}$ is yet another systematic, but this is arguably better than blindly assuming $e_{\rm res} = 0$ for all posterior samples of all the events, as has been done so far.

Chapter 4

Non-adiabatic dynamics of eccentric black-hole binaries

Abstract

Eccentric black-hole binaries are among the most awaited sources of gravitational waves, yet their dynamics lack a consistent framework that provides a detailed and physically robust evolutionary description due to gauge issues. We present a new set of non-orbit-averaged equations, free from radiation-reaction gauge parameters, that accurately describe the evolution of orbital elements for eccentric, non-spinning black-hole binaries. We derive these equations by mapping the Keplerian orbital elements to a new set of characteristic parameters using energy and angular momentum definitions combined with near-identity transformations. The resulting framework is valid for arbitrary eccentricities, including parabolic and hyperbolic limits. Using this framework, we demonstrate effects of the non-adiabatic emission of gravitational waves —characteristic of eccentric binaries— on the orbital parameters. Furthermore, we assess the regime of validity of the widely used orbit-averaged equations first derived by Peters in 1964.

Importantly, their breakdown becomes evident at the first pericenter passage, implying that the validity of the orbit-averaged approximation cannot be inferred solely from binary initial conditions. The formalism we introduce, accurate up to 2.5 post-Newtonian order, aims to provide a robust tool for making reliable astrophysical predictions and accurately interpreting current and future gravitational wave data, paving the way for deeper insights into the dynamics of eccentric black hole binaries.

Summary

In this chapter, we consider the exact, i.e., non-averaged on any timescale, problem of describing the dynamics of *non-spinning* BH binaries. This is the first step toward a deeper understanding of the full problem central to this thesis, which includes spins. In Sec. 4.1.1, we reiterate the reasons why this study is meaningful in GW astronomy. In Sec. 4.1.2, we present an executive summary to consolidate the main results of the chapter, making them accessible amidst the sometimes tedious calculations. In Sec. 4.2, we provide a brief introduction to balance laws, introduce their application to describe the dynamics of BH binaries, and present both the Peters' and the osculating-orbit formalisms. In Sec. 4.3, we present the derivation of Eqs. (4.2)–(4.5). In Sec. 4.4, we compare the evolution of BH binaries using different approaches, investigate the breakdown of the orbit-average approximation, and study the impact of gauge parameters. Finally, in Sec. 4.5, we summarize our findings and outline future prospects.

The material presented in this chapter has been published in Fumagalli *et al.* (2025).

4.1 Introduction

4.1.1 Context

Accurately describing the dynamics of non-spinning BHs on eccentric orbits is a long-standing and fundamental challenge in astrophysics (see e.g. [182, 183, 184, 185, 186]). This problem has been approached from various perspectives over more than sixty years due to its critical importance, particularly in the GW field [50, 45, 187, 188, 189, 190, 191]. As shown in Sec. 1.2, a wide variety of formation channels for binary systems, ranging from stellar-mass [70, 74, 192, 193, 194, 195, 196, 182] to supermassive BHs [197, 198], predict their evolution on eccentric orbits. This highlights the need to understand eccentric system dynamics and the long-term evolution of their orbital parameters, which is the first step toward building accurate waveform templates for GW detections.

The dynamics of binary BHs is typically described using balance laws: the energy and angular momentum carried away by GWs are equated to the corresponding losses in the energy and angular momentum of the orbit, which directly leads to the coalescence of the binary [199, 94, 9, 200, 201]. The seminal work by Peters [16] was among the first to apply balance laws to eccentric binaries, establishing the most widely used framework for their dynamics. This formalism employs a Newtonian description of the orbital energy and angular momentum, and leverages an orbit-average approximation to capture the secular evolution of the orbital elements [187, 202, 203].

However, as initially mentioned in Chap. 2, this approach has important limitations. The concept of averaging pre-dates Peters' work, and was originally proposed by Isaacson [204, 205] as a method for handling gauge effects in the definitions of energy and angular momentum from a suitably defined stress-energy tensor. Yet, this averaging procedure relies on the existence of a GW timescale that is longer than the timescale of

gauge-dependent oscillations, allowing the deployment of multiple scale analysis [206] from which the secular (or averaged) approximation would constitute the leading order behavior. For generic binary systems, the latter is governed by the orbital timescale, while the former is the dissipative timescale associated with orbital energy loss due to GW emission, the so-called backreaction or radiation-reaction timescale. In nature, the requirement of separation of scales is not always met. Post-adiabatic corrections to the secular limit become important when constructing waveform templates [207, 50, 189, 187]. Further, for highly eccentric binaries, GW emission is concentrated during pericenter passage [208], and the timescale associated with the emission is thus shorter than the orbital period [209]. Even outside of the GW context, orbit averaging to obtain a secular approximation is well known to fail in three-body interactions [210], and more robust analysis methods have been developed to properly handle oscillatory orbital perturbations [211, 212], such as the perihelion precession of Mercury [213].

For an accurate description of binary dynamics, especially from dynamical captures, a closer look is needed. The equations of motion have to be defined locally, within the near-zone —a region enclosing the source and much smaller than the typical wavelength of the radiation emitted [94, 9]. There, the motion of the BHs is governed not only by their mutual Newtonian gravitational attraction, but also by dissipative terms accounting for GW emission. This "local" approach underpins the PN formalism [214, 215, 9].

Translating the equations of motion into orbital evolution first requires a precise definition of the orbit itself [50]. In GR, there is no unique way to define an orbit, leading to two main approaches: (i) the Lagrangian planetary or osculating formalism, introduced by Lincoln and Will [8], which relies on an intuitive Newtonian parametrization of the orbit, but with the orbital elements promoted to be functions of time; and (ii) the quasi-Keplerian formalism, developed by Damour and Deruelle [45], which employs a more

accurate PN parametrization. However, the latter introduces complexities like multiple eccentricity parameters, complicating the interpretation of the orbital elements, while the former requires caution in interpreting osculating quantities physically [207, 216].

Both approaches share a fundamental issue: they rely on instantaneous, local definitions of radiation-reaction terms, which are inherently gauge-dependent [217, 218, 219]. Gauge dependencies are a constant feature in GR and represent the invariance of the theory under coordinate transformations [94]. Not all components of the tensorial quantities characteristic of GR are meaningful. Certain gauges need to be chosen to remove spurious degrees of freedom and extract the physical content. A common example is the use of the Lorenz and Transverse-Traceless (TT) gauges in the linearized theory of gravity to extract GW potentials [200]. Although all gauges have a common origin, they are not all equivalent.

In this work, we focus solely on radiation-reaction gauges, which first enter the PN equations of motion at 2.5PN order. We define radiation-reaction gauges as those that arise when we artificially partition regions of spacetime to simplify the treatment of the two-body problem. For instance, the PN formalism is valid only in the near zone. At larger separations (which include ∞), this expansion diverges and a different formalism has to be employed [200]. To bridge these regimes, the two approaches must be connected in a region where their validity overlaps. This procedure, known as asymptotic matching [7], directly relies on defining such a boundary. However, this boundary is not a distinct region of spacetime but rather a conceptual limit imposed by our tools. Consequently, this locally (and arbitrarily) defined distance from the source can vary depending on the reference frame, introducing ambiguity that manifests as radiation-reaction gauge parameters [7, 200, 9]. These parameters enter the definition of the energy and angular momentum of the system, and the freedom in choosing them

renders the evolution of the orbital elements ambiguous, complicating the extraction of physically meaningful insights.

4.1.2 Executive summary

How, then, do eccentric BH binaries unambiguously evolve under GW emission, and across all relevant timescales? The orbit-averaged equations by Peters [16] provide an approximate and limited description. While osculating methods yield more precise equations of motion, they lead to orbital evolutions that are intrinsically ambiguous. In this work, we derive a novel, gauge-free, non-adiabatic set of evolutionary equations for the orbital elements of eccentric BH binaries, grounded in the osculating description of the orbit. Specifically, by "gauge-free" we mean that the equations we present are explicitly independent of the 2.5PN radiation-reaction gauge parameters. Further, in the remainder of this work, the term "gauge parameters" refers exclusively to the 2.5PN radiation reaction parameters.

We achieve this by redefining the orbit using the following mapping:

$$y = \bar{y} + \frac{1}{c^5}\delta\bar{y}, \tag{4.1}$$

where y represents any of the orbital parameters including eccentricity e, semi-latus rectum p [which is related to the semi-major axis a through $p = a(1 - e^2)$], true anomaly f, longitude of the pericenter ω, as well as the time variable t. The $\delta\bar{y}$ functions are defined to ensure that the evolution equations for $\bar{y}$ are free from radiation-reaction gauge dependencies. We shall refer to the barred quantities $\bar{y}$ as *characteristic parameters*, as these are not necessarily the geometric (or orbital) parameters describing the gauge-dependent orbital trajectory.

Radiation-reaction gauge parameters enter the dissipative terms of the osculating equations [7], which are proportional to c^{-5} and would vanish under orbit averaging. However, our reparametrization achieves gauge freedom without relying on this approximation. We find the $\delta\bar{y}$ functions by requiring that the expressions for the binary's energy and angular momentum recover their Newtonian forms when expressed in terms of the new characteristic variables $\bar{y}$ and applying near-identity transformations [220].

The resulting evolutionary equations of the characteristic parameters:

$$\frac{\mathrm{d}\bar{p}}{\mathrm{d}\bar{t}} = -\frac{8}{5}\frac{\eta}{c^5}\frac{M^3}{\bar{p}^3}(1+\bar{e}\cos\bar{f})^3\left[8+12\bar{e}\cos\bar{f}+\bar{e}^2\left(1+3\cos 2\bar{f}\right)\right], \tag{4.2}$$

$$\frac{\mathrm{d}\bar{e}}{\mathrm{d}\bar{t}} = -\frac{2}{15}\frac{\eta}{c^5}\frac{M^3}{\bar{p}^4}(1+\bar{e}\cos\bar{f})^3\left[72\cos\bar{f}+\bar{e}\left(116+52\cos 2\bar{f}\right)+\bar{e}^2\left(109\cos\bar{f}+\right.\right.$$
$$\left.\left.+11\cos 3\bar{f}\right)+\bar{e}^3\left(6+18\cos 2\bar{f}\right)\right], \tag{4.3}$$

$$\frac{\mathrm{d}\bar{f}}{\mathrm{d}\bar{t}} = \frac{M^{1/2}}{\bar{p}^{3/2}}\left(1+\bar{e}\cos\bar{f}\right)^2, \tag{4.4}$$

$$\frac{\mathrm{d}\bar{\omega}}{\mathrm{d}\bar{t}} = 0. \tag{4.5}$$

This set of equations describes the evolution of eccentric binaries in a manner consistent with the established osculating formalism while eliminating unphysical artifacts arising from radiation-reaction gauge parameters.

We leverage our new equations to test for violations of the adiabatic assumptions in the formalism of Ref. [16], assessing the regions of the $(\bar{p},\bar{e})$ parameter space where it can or cannot be employed. We confirm that the breakdown of the adiabatic formalism is connected to the timescales on which the binary evolution takes place. However, we show that knowledge of the initial conditions alone is insufficient to establish the validity of Peters' equations. Instead, one must examine the behavior of the timescales at the first pericenter passage.

4.2 Radiation reaction

4.2.1 Conservation laws

In Newtonian mechanics, knowing all forces in a system defines its equations of motion. However, in complex systems, this information is hard to obtain. Here, conservation laws provide key insights. Conservation laws are linked to the system's stress-energy tensor $T^{\alpha\beta}$ and are expressed through its divergence, which vanishes when all relevant contributions are included

$$T^{\alpha\beta}{}_{,\beta} = 0, \tag{4.6}$$

where the comma denotes a partial derivative. As a practical example, consider a perfect fluid in special relativity. By defining its stress-energy tensor and substituting it into Eq. (4.6), one obtains the Euler equations of motion (see Ref. [9] for a complete derivation).

Equation (4.6) represents a conservation law in flat spacetime, as it enables the definition of globally conserved quantities, such as total energy and angular momentum. This is due to the presence of partial derivatives, which allow differential identities to be transformed into integral ones. Specifically, total energy and angular momentum can be determined by integrating Eq. (4.6) over the entire three-dimensional space enclosing the source.

This property of Eq. (4.6) is lost in linearized gravity, where $g_{\mu\nu} \sim \eta_{\mu\nu} + \epsilon h_{\mu\nu} + \mathcal{O}(\epsilon^2)$ with $\eta_{\mu\nu}$ the flat Minkowski metric, $h_{\mu\nu}$ the linearized metric perturbation, and ϵ an order-keeping parameter. In GR, ordinary derivatives are replaced by covariant derivatives, and commas are substituted with semicolons. Behind this "extra dot" lies

the nearly fifty-year-long debate on the existence of GWs and the definition of the energy and momentum of the gravitational field [221, 94, 9, 222]. In GR, Eq. (4.6) becomes

$$T^{\alpha\beta}{}_{;\beta} = \left(\sqrt{-g}T^{\alpha\beta}\right)_{,\beta} + \Gamma^{\alpha}{}_{\beta\gamma}\left(\sqrt{-g}T^{\beta\gamma}\right) = 0, \tag{4.7}$$

where g is the metric determinant, and $\Gamma^{\alpha}{}_{\beta\gamma}$ are the Christoffel symbols, which are of $\mathcal{O}(\epsilon)$. The first term resembles the left-hand side of Eq. (4.6), while the second term indicates why Eq. (4.7) no longer describes the conservation of energy and angular momentum. Specifically, this term prevents the definition of globally conserved quantities solely from $T^{\alpha\beta}$ as one can always define a coordinate system where $\Gamma^{\alpha}_{\beta\gamma} = 0$ [94].

The strategy is to consider a quantity $t^{\alpha\beta}$ that represents the distribution of gravitational energy and momentum and is conserved alongside the matter stress-energy tensor. This leads to a conservation law analogous to Eq. (4.6)

$$\left(T^{\alpha\beta} + t^{\alpha\beta}\right)_{,\beta} = 0. \tag{4.8}$$

Various definitions for $t^{\alpha\beta}$ have been proposed in the literature (see Refs. [223, 224] for a comprehensive review). In this work, we adopt the formulation first put forward by Landau & Lifshitz [199], which arises from an exact reformulation of Einstein's equations [199, 200, 9] and leads to the popular pseudo-tensor $t^{\alpha\beta}$.

One might be tempted to interpret this quantity as the energy and momentum of the gravitational field. However, caution is required here. Due to its non-tensorial nature, the definition of $t^{\alpha\beta}$ is not unique; its value can change under coordinate transformations, and it can even be made to vanish in some frames [199, 204, 205, 225, 200, 9]. This is

not surprising and aligns with the equivalence principle in GR, which asserts that local gravitational effects can be nullified through an appropriate choice of coordinates.

For this reason, such pseudotensors cannot be used to infer the local back-reaction of a system due to gravitational radiation and cannot be directly used to define the equations of motion. However, Eq. (4.8) allows for the definition of globally conserved quantities and, through further algebraic manipulation, provides definitions for the fluxes of energy and angular momentum carried to infinity by gravitational radiation [226, 9].

It is important to note that Eqs. (4.6) and (4.8), although both representing conservation laws, are conceptually distinct [9]. The first arises from the local conservation of energy and momentum, making it a fundamental principle that is entirely independent of Einstein's equations in flat spacetime. In contrast, the second directly relies on Einstein's equations, as they are explicitly used in the definition of the stress-energy pseudotensor.

By integrating Eq. (4.8) over a surface $S_j = R^2 N_j$, where $R = |\boldsymbol{x}|$ is the distance from the source and $\boldsymbol{N} = \boldsymbol{x}/R$ is a unit vector, and assuming no intersection with matter while taking $R \to \infty$, the fluxes of energy and angular momentum transported by GW are defined, respectively, as

$$\mathcal{P} = c \oint_\infty (-g) t^{0k} \mathrm{d}S_k, \tag{4.9}$$

$$\mathcal{F}^{jk} = \oint_\infty \left[x^j (-g) t^{kn} - x^k (-g) t^{jn} \right] \mathrm{d}S_n. \tag{4.10}$$

To ensure a clear physical meaning, the integrals in Eqs. (4.9) and (4.10) must be evaluated in asymptotically Minkowskian coordinates. If this condition is not met, i.e., the spacetime is not flat at infinity, Eqs. (4.9) and (4.10), along with all quantities related to them, including total energy and angular momentum, become meaningless [94].

Therefore, we are interested only in the definition of $t^{\alpha\beta}$ in this regime, where we can also assume that the characteristic wavelength of GWs is much smaller than the background curvature scale. In other words, we must operate in the short-wavelength limit [204, 205, 94, 9, 200].

By exploiting the definition of the Landau-Lifshitz pseudotensor in this regime and applying the Brill-Hartle averaging procedure [227], along with imposing the Lorentz and TT gauge, one finally obtains a physically meaningful expression for $t^{\alpha\beta}$. This averaging method, first introduced in Ref. [227] and later applied in the GW context for the first time in Refs. [204, 205], is a necessary step as it enables a clear identification of the effects of GWs on the background spacetime. Consequently, it allows a practical definition of the energy and angular momentum content of GWs only [200]. The resulting Landau-Lifshitz pseudotensor depends entirely on the derivatives of the usual GW potentials expressed in the TT gauge

$$t^{\alpha\beta} = \frac{c^4}{32\pi}\left\langle\!\!\left\langle h^{\mathrm{TT}\,,\alpha}_{\gamma\delta}\; h^{\gamma\delta\,,\beta}_{\mathrm{TT}} \right\rangle\!\!\right\rangle, \tag{4.11}$$

where $\langle\!\langle\cdot\rangle\!\rangle$ is the Brill-Hartle average [227, 205]. We stress that such expression is invariant under any gauge transformation (see Ref. [205, 200, 9, 224] for a formal proof).

Plugging Eq. (4.11) into Eqs. (4.9) and (4.10) returns the fluxes expressed solely in terms of the gravitational potentials while preserving gauge-invariance. Specifically, defining the gravitational potentials in terms of the mass quadrupole tensor I^{jk} of the system leads to the famous quadrupole formula [9, 200]

$$\mathcal{P} = \frac{1}{5c^5}\,\ddot{I}^{\langle jk\rangle}\,\ddot{I}^{\langle jk\rangle} + \mathcal{O}(c^{-7}), \tag{4.12}$$

$$\mathcal{F}^{jk} = \frac{2}{5c^5}\left(\ddot{I}^{\langle jp\rangle}\dddot{I}^{\langle kp\rangle} - \ddot{I}^{\langle kp\rangle}\dddot{I}^{\langle jp\rangle}\right) + \mathcal{O}(c^{-7}), \tag{4.13}$$

where the overdots denote time derivatives and the angular brackets indicate the symmetric trace-free operation $n^{\langle jk\rangle} = n^j n^k - \frac{1}{3}\delta^{jk}$. With Eqs. (4.12) and (4.13) established, the motion is described by the related balance equations

$$\frac{\mathrm{d}\mathcal{E}}{\mathrm{d}t} = -\mathcal{P}, \tag{4.14}$$

$$\frac{\mathrm{d}\mathcal{L}^{jk}}{\mathrm{d}t} = -\mathcal{F}^{jk}, \tag{4.15}$$

where $\mathcal{E}$ represents the total energy of the system, and $\mathcal{L}^{jk}$ denotes the total angular momentum.

4.2.2 Two-body dynamics

Conservation laws, and consequently balance equations, have been extensively employed to describe the dynamics of two-body systems with varying degrees of accuracy. Equations (4.14) and (4.15) require knowledge of the energy, angular momentum, and fluxes. Expressions for these quantities have been central to the development of PN theory, and are now determined up to 4.5 PN order [7, 228, 229, 230, 231].

The lowest order, i.e., Newtonian, treatment of the two-body problem and definitions, in this regime, of energy, angular momentum, and orbital elements, are reported in Sec. 1.3. Here, we analyze the effects of radiation reaction on the dynamics of binary BHs. Specifically, these have to be accounted for on two distinct scales: globally and locally [9]. On the global scale, the total time derivative of the energy and angular momentum no longer vanishes; instead, due to GW emission, it equals the fluxes given

in Eqs. (4.12) and (4.13), which at leading order are expressed as [6, 7]

$$\mathcal{P} = -\frac{8}{5c^5}\eta^2\frac{M^2}{r^4}\left(4v^2 - \frac{11}{3}\dot{r}^2\right), \tag{4.16}$$

$$\mathcal{F}^{jk} = -\frac{8}{5c^5}\eta \boldsymbol{L}_{\rm N}\frac{M^2}{r^3}\left(2v^2 + 2\frac{M}{r} - 3\dot{r}^2\right). \tag{4.17}$$

Locally, i.e. in the near zone, the system dynamics have to react to what is happening globally i.e., in the far wave zone. In other words, equations of motion must include dissipative terms that account for the radiation of GW to infinity [9]. Such dissipative terms are proportional to c^{-5} and, at the leading order, result in an additional acceleration term on the particle

$$\boldsymbol{a} = -\frac{M\boldsymbol{n}}{r^3}\left[1 + \mathcal{O}(c^{-5})\right] = \boldsymbol{a}_{\rm N} + \boldsymbol{a}_{\rm 2.5PN}\,. \tag{4.18}$$

This expression is identical to the one reported in Eq. (1.1) when considering only the first term, i.e., the Newtonian, and that $\propto \mathcal{O}(c^{-5})$. In Eq. (4.18), conservative terms present in Eq. (1.1), characterized by even powers of c^{-1}, and higher-order corrections for the dissipative term have been omitted (cf. Refs. [7, 9]). The term $\boldsymbol{a}_{\rm 2.5PN}$ models the radiation-reaction contribution to the acceleration, and can only depend on v^2, m/r, and $\dot{r}^2$ [8, 6, 7]. In particular, one has

$$\boldsymbol{a}_{\rm 2.5PN} = -\frac{8}{5}\frac{\eta M^2}{r^3}\left(-A_{\rm 2.5PN}\,\dot{r}\boldsymbol{n} + B_{\rm 2.5PN}\,\boldsymbol{v}\right), \tag{4.19}$$

where

$$A_{\rm 2.5PN} = a_1 v^2 + a_2\frac{M}{r} + a_3\dot{r}^2, \tag{4.20}$$

$$B_{\rm 2.5PN} = b_1 v^2 + b_2\frac{M}{r} + b_3\dot{r}^2, \tag{4.21}$$

and the a_i's and b_i's are coefficients that still need to be determined. To this end, Ref. [7] employs asymptotic matching techniques to connect the near-zone solution for the dynamics with the far-zone wave fluxes. Here is where radiation-reaction gauges come into play. In practice, one must first define $\mathcal{E}$ and $\boldsymbol{\mathcal{L}}$ to include contributions at 2.5PN order

$$\mathcal{E} = E_{\rm N} + E_{\rm 2.5PN}, \tag{4.22}$$

$$\boldsymbol{\mathcal{L}} = \boldsymbol{L}_{\rm N} + \boldsymbol{L}_{\rm 2.5PN}. \tag{4.23}$$

Following the same reasoning used for writing down the generic definition of $\boldsymbol{a}_{\rm 2.5PN}$, we have

$$E_{\rm 2.5PN} = -\frac{8}{5}\frac{\eta M^2}{c^5 r^2}\dot{r}\left(p_1 v^2 + p_2\frac{M}{r} + p_3\dot{r}^2\right), \tag{4.24}$$

$$\boldsymbol{L}_{\rm 2.5PN} = \frac{8}{5}\boldsymbol{L}_{\rm N}\frac{\eta M}{c^5 r}\dot{r}\left(q_1 v^2 + q_2\frac{M}{r} + q_3\dot{r}^2\right), \tag{4.25}$$

where the p_i's and q_i's are again coefficients to be determined, and

$$\frac{{\rm d}\mathcal{E}}{{\rm d}t} = \boldsymbol{v}\cdot\boldsymbol{a}_{\rm 2.5PN} + \frac{{\rm d}E_{\rm 2.5PN}}{{\rm d}t}, \tag{4.26}$$

$$\frac{{\rm d}\boldsymbol{\mathcal{L}}}{{\rm d}t} = \boldsymbol{r}\times\boldsymbol{a}_{\rm 2.5PN} + \frac{{\rm d}\boldsymbol{L}_{\rm 2.5PN}}{{\rm d}t}. \tag{4.27}$$

Finally, one must match these expressions with the fluxes evaluated at the same PN order [6, 7], i.e., one must equate the right-hand side of Eqs. (4.26) and (4.27) with Eqs. (4.16) and (4.17). Since this work considers terms up to 2.5PN order, the fluxes defined in Eqs. (4.16) and (4.17) can be used for this purpose.

There are twelve undetermined coefficients in Eqs. (4.20), (4.21), (4.24), and (4.25).

However, comparing the terms in Eqs. (4.26) and (4.27) with those in Eqs. (4.16) and (4.17) specifies only ten of these coefficients. This leaves two degrees of freedom, represented by the arbitrary radiation-reaction gauge parameters α and β [6, 7]. We report the resulting expression for such parameters in Table 4.1. As noted in Refs. [7, 9], the presence of α and β reflects how the relative orbital separation vector $\boldsymbol{r}$, explicitly present in Eqs. (4.26) and (4.27), depends on the choice of coordinate frame. Although $\boldsymbol{r}$ is not a coordinate itself, its behavior is influenced by the adopted reference frame.

Each choice of α and β corresponds to a specific coordinate system. The harmonic coordinate system, commonly used in PN derivations [200, 9, 232], is defined by ($\alpha = -1$, $\beta = 0$) [7, 233]. However, this framework introduces unnecessary complexity in both the metric and the radiation reaction force [234, 9]. As demonstrated in Ref. [9], alternative combinations of these radiation-reaction gauges can significantly simplify some of the metric components and, consequently, the radiation reaction potentials. Notable examples include the Burke-Thorne gauge ($\alpha = 4$, $\beta = 5$) [235, 236, 94, 7] and the Schäfer gauge ($\alpha = 5/3$, $\beta = 3$) [234]. In the following, we compare our findings against equations of motion obtained with these three sets of gauge parameters.

	$i=0$	$i=1$	$i=2$
a_i	$3+3\beta$	$\frac{23}{3}+2\alpha-3\beta$	-5β
b_i	$2+\alpha$	$2-\alpha$	$-3-3\alpha$
p_i	$-(\alpha+2)$	0	β
q_i	0	α	0

Table 4.1: Coefficients of Eqs. (4.20), (4.21), (4.24) and (4.25) determined by matching Eqs. (4.26) and (4.27) with the fluxes of Eqs. (4.16) and (4.17). See Refs. [6, 7].

4.2.3 Lagrangian planetary equations

Once the expression for $\boldsymbol{a}_{2.5\mathrm{PN}}$ is determined, the method of osculating orbits provides a suitable framework to derive the evolution equations for the orbital elements; these are known as either Lagrangian planetary equations or osculating equations. The broad strategy is to make use of Newtonian description of the dynamics (Sec. 1.3) and solve Eq. (4.19) by promoting the quantities introduced in Eqs. (1.7)–(1.10) to functions of time, treating $\boldsymbol{a}_{2.5\mathrm{PN}}$ as a perturbation to the Newtonian two-body problem [9, 46]. Specifically, it assumes that, at any given time t_i, the system can be described by a Newtonian configuration characterized by a set of orbital elements

$$\mu^\sigma(t_i) = [p(t_i), e(t_i), f(t_i), \omega(t_i)]. \tag{4.28}$$

Due to the perturbation, these elements differ from those describing the system at another time t_j (with $i \neq j$). Practically, one needs to solve the following set of equations to recover the evolution of the orbital elements

$$\frac{\partial \boldsymbol{r}}{\partial \mu^\sigma}\frac{\mathrm{d}\mu^\sigma}{\mathrm{d}t} = 0, \tag{4.29}$$

$$\frac{\partial \boldsymbol{v}}{\partial \mu^\sigma}\frac{\mathrm{d}\mu^\sigma}{\mathrm{d}t} = \boldsymbol{a}_\mathrm{rr}, \tag{4.30}$$

where $\boldsymbol{r}$ and $\boldsymbol{v}$ are defined as in Eqs. (1.4) and (1.5). To this end, it is useful to express $\boldsymbol{a}_{2.5\mathrm{PN}}$ in the basis introduced in Sec. 1.3

$$\boldsymbol{a}_{2.5\mathrm{PN}} = \mathcal{R}\boldsymbol{n} + \mathcal{S}\boldsymbol{\lambda}, \tag{4.31}$$

$$\mathcal{R} = \frac{8}{5c^5}\frac{\eta M^2}{r^3}\dot{r}(A_{2.5} - B_{2.5}), \tag{4.32}$$

$$\mathcal{S} = -\frac{8}{5c^5}\frac{\eta M^2}{r^3}\dot{r}B_{2.5}, \tag{4.33}$$

where $A_{2.5}$ and $B_{2.5}$ are defined respectively in Eqs. (4.20) and (4.21) and their a_i and b_i coefficients reported in Table 4.1. The conversion between phase-space coordinates and orbital parameters is reported in Eqs. (1.7)–(1.10). The resulting evolution equations for the orbital elements μ^σ are then

$$\frac{\mathrm{d}p}{\mathrm{d}t} = \sqrt{\frac{p^3}{M}}\frac{2}{(1+e\cos f)}\mathcal{S}, \tag{4.34}$$

$$\frac{\mathrm{d}e}{\mathrm{d}t} = \sqrt{\frac{p}{M}}\left[\sin f\,\mathcal{R} + \frac{2\cos f + e(1+\cos^2 f)}{1+e\cos f}\mathcal{S}\right], \tag{4.35}$$

$$\frac{\mathrm{d}f}{\mathrm{d}t} = \sqrt{\frac{M}{p^3}}(1+e\cos f)^2 + \frac{1}{e}\sqrt{\frac{p}{M}}\left[\cos f\,\mathcal{R} - \frac{2+e\cos f}{1+e\cos f}\sin f\,\mathcal{S}\right], \tag{4.36}$$

$$\frac{\mathrm{d}\omega}{\mathrm{d}t} = \frac{1}{e}\sqrt{\frac{p}{M}}\left[-\cos f\,\mathcal{R} + \frac{2+e\cos f}{1+e\cos f}\sin f\,\mathcal{S}\right], \tag{4.37}$$

where $\mathcal{S}$ and $\mathcal{R}$ are defined in Eqs. (4.32) and (4.33). This set of equations captures the evolution of BH binary systems, including the orbital-timescale dynamics and the non-adiabatic emission of GWs. This formulation holds in both the parabolic and hyperbolic limits.

4.2.4 Peters' equations

The secular behavior of orbital elements is obtained by orbit averaging Eqs. (4.34)–(4.37). This yields

$$\left\langle\frac{\mathrm{d}p}{\mathrm{d}t}\right\rangle = -\frac{64}{5c^5}\frac{\mu M^2}{p^3}(1-e^2)^{3/2}\left(1+\frac{7}{8}e^2\right), \tag{4.38}$$

$$\left\langle\frac{\mathrm{d}e}{\mathrm{d}t}\right\rangle = -\frac{304}{15c^5}\frac{\mu M^2}{p^4}e(1-e^2)^{3/2}\left(1+\frac{121}{304}e^2\right), \tag{4.39}$$

which is the popular result by Peters [16] (these are equivalent to Eqs. (2.10) and (2.11) but expressed as funtion of semi-latus rectum p). Here, $\langle\cdot\rangle$ denotes the orbit-averaging operation defiend in Eq. (1.14). Specifically, Peters' approach relies on two key choices: (i) adopting the Newtonian definitions of energy and angular momentum, and (ii) averaging the resulting equations over the orbital period. Averaging removes the oscillatory variations occurring on the orbital timescale from the expressions for the energy, the angular momentum, and their corresponding fluxes. Consequently, ω remains fixed during the inspiral, and the usage of Newtonian definitions is justified.

The orbit-averaging approximation is valid whenever changes induced by radiation reaction are small over an orbital period. This requires the timescale [1]

$$\tau_{\rm rr} = \frac{p}{|{\rm d}p/{\rm d}t|}, \tag{4.40}$$

on which GW emission modifies the orbital parameters, to be much longer than the orbital period, i.e., $\tau_{\rm orb} \ll \tau_{\rm rr}$. Additionally, the orbital period must be finite. As pointed out in Chap. 2, Peters' equations predict that $e \to 1$ for all eccentric binaries as $t \to -\infty$, and consequently $\tau_{\rm orb} \to \infty$. This invalidates the assumptions used to derive the equations themselves, leading to an incorrect evolution of the orbital elements. Finally, as noted in Sec. 2.2.2, the definition of the radiation-reaction timescale given in Eq. (4.40) is not unique. In principle, it can be computed using different orbital elements and their respective time derivatives. While small differences may arise, there are no preferred parameters for defining $\tau_{\rm rr}$. We therefore choose to use the semi-latus rectum due to its straightforward interpretation.

[1] Note that this definition of the radiation reaction timescale is not unique (see Sec. 2.2.2), i.e. one could make other choices such as $\tau_{\rm rr} = e/|{\rm d}e/{\rm d}t|$ or $\tau_{\rm rr} = \omega_{\rm orb}/|{\rm d}\omega_{\rm orb}/{\rm d}t|$ where $\omega_{\rm orb}$ is the orbital frequency or use the definiton provided in Eq. (2.12). We have checked that such alternative choices do not alter the final results of this work.

4.3 Fixing the 2.5PN ambiguity

4.3.1 Why this chapter

The price to pay for adopting the osculating equations instead of Peters' is the presence of radiation-reaction gauge parameters. In Eqs. (4.24), (4.25), and (4.19), the expressions for energy, angular momentum, and their evolution, and consequently the evolution of the orbital elements, are inherently ambiguous, and this ambiguity is encoded in the free parameters α and β.

As discussed in Sec. 4.2.2, radiation-reaction gauge parameters enter the equations of motion at 2.5PN order. The appearance of new terms in the definition of energy and angular momentum when including radiation reaction is not unique to gravity [94, 9]. In electromagnetism, similar terms appear when considering the dynamics of charged bodies. In that context —and in complete analogy with binary BHs— part of the system's energy and angular momentum are converted into radiation which propagates outward, leaving the system. When balance equations are used to describe the dynamics, one must consider the additional terms known as Schott energy and angular momentum [237, 238, 239]. Specifically, such terms appear exactly as the 2.5 PN term in the right-hand side of Eqs. (4.26) [9, 240, 239]. However, the interpretation of either electromagnetic waves or their energy content is not ambiguous. Here, the analogy between electromagnetism and gravity cannot go any further than a mathematical resemblance. Schott terms have a clear physical meaning: they represent bound field energy, a quantity that remains attached to the system and is reversibly exchanged between the electromagnetic field and the bodies [9, 239].

In contrast, the 2.5PN terms in gravity directly result from dividing the spacetime into zones, which is required to connect the energy and angular momentum transported

by GWs at infinity, where they can be clearly quantified and measured, to the dynamics near the source, where these quantities are not well-defined for the gravitational field. The ambiguity in choosing the boundary where matching conditions are applied directly impacts the definition of the system's energy and angular momentum, making the physical interpretation of these quantities unclear. Resolving this issue is essential for accurately studying the dynamics of binary BHs. Specifically, our goal here is to derive osculating-like equations that do not depend on the parameters α and β.

As already discussed in Sec. 4.2.4, these gauge parameters can be eliminated by orbital averaging. Radiation-reaction terms appear in the equations of motion with odd powers of c^{-1}, as they are necessary to break the time-reversal invariance of the theory (radiation can only propagate outward). This also results in their disappearance when averaging is applied. However, orbital averaging results in an approximate description of the evolution of binaries and cannot be applied across the entire parameter space. This limitation justifies the need for the present work.

Our strategy is to introduce new definitions of the orbital elements. These new characteristic variables, for which we provide a mapping to their Keplerian counterparts, allow us to derive a set of evolution equations where the radiation-reaction gauge parameters are completely eliminated. This procedure requires invoking near-identity transformations, which we now introduce.

4.3.2 Near-identity transformations

Near-identity transformations (NITs) [211] are a mathematical tool used to simplify the equations of motion of dynamical systems by removing undesired dependencies on certain parameters. For instance, in the study of extreme mass-ratio inspirals, NITs are often employed to eliminate oscillatory terms from the equations of motion, enabling

more efficient and accurate integration [241, 242]. Similar techniques have also been employed in Refs. [46, 47] to derive the evolutionary equations for the orbital elements using the quasi-Keplerian formalism, although retaining gauge parameters. The core idea is to transform one's variables into a new set that retains the essential dynamics while suppressing unwanted dependencies in the equations of motion. Consider a generic dynamical system described by $\boldsymbol{x} = (x_0, x_1, \ldots, x_n)$ and their evolution equations

$$\dot{x_i} = f^0_{x_i}(\boldsymbol{x}) + \epsilon f_{x_i}(\boldsymbol{x}, k) + \mathcal{O}(\epsilon^2), \tag{4.41}$$

where $i = 0, \ldots, n$, the overdot denotes differentiation with respect to a chosen variable (e.g., time). The functions $f^j_{x_i}$ depend on both the variables $\boldsymbol{x}$ as well as another parameter k, which we wish to eliminate. The goal of NITs is to find a transformation that maps these variables to a new set, $\tilde{\boldsymbol{x}} = (\tilde{x}_0, \tilde{x}_1, \cdots, \tilde{x}_{\rm n})$, such that

$$\tilde{\boldsymbol{x}} \xrightarrow[\text{NIT}]{\text{Inverse}} \boldsymbol{x} + \mathcal{O}(\epsilon), \tag{4.42}$$

whenever $\epsilon \ll 1$. In this transformed framework, the equations of motion for the new variables are independent of k

$$\dot{\tilde{x}}_i = F^0_{\tilde{x}_i}(\tilde{\boldsymbol{x}}) + \epsilon F_{\tilde{x}_i}(\tilde{\boldsymbol{x}}) + \mathcal{O}(\epsilon^2). \tag{4.43}$$

To achieve this, we assume the existence of a transformation satisfying the inverse condition of Eq. (4.42) in the form

$$\boldsymbol{x} = \tilde{\boldsymbol{x}} + \epsilon X(\tilde{\boldsymbol{x}}, k), \tag{4.44}$$

where $X(\tilde{\boldsymbol{x}}, k)$ is an unknown set of functions. By differentiating this expression, comparing it with the original equations of motion Eq. (4.41), employing Eq. (4.43), and expanding in ϵ, one gets

$$\dot{X}(\tilde{\boldsymbol{x}}, k) = f_{x_i}(\tilde{\boldsymbol{x}}, k) - F_{\tilde{x}_i}(\tilde{\boldsymbol{x}}). \tag{4.45}$$

Here, make use of the assumption that the difference between the original and transformed variables is always of $\mathcal{O}(\epsilon)$, implying $F^0_{\tilde{x}_i} = f^0_{x_i}$. For the same reason, in all terms proportional to ϵ we can freely switch between $\boldsymbol{x}$ and $\tilde{\boldsymbol{x}}$. By integrating Eq. (4.45) and choosing $F_{\tilde{x}_i}$ appropriately, one can ensure that iterating this procedure results in equations of motion for $\tilde{\boldsymbol{x}}$ that are free from the unwanted dependency on k. The strength of NITs lies in the flexibility to choose the unknown functions $F_{\tilde{x}_i}(\tilde{\boldsymbol{x}})$.

We now apply this method to remove the dependency of the radiation-reaction gauge parameters α and β from the osculating equations describing BH binaries on generic orbits.

4.3.3 Our new set of evolutionary equations

We map the osculating orbital parameters (p, e, ω, f, t) to a new set $(\bar{p}, \bar{e}, \bar{\omega}, \bar{f}, \bar{t})$, and impose that their evolutionary equations are independent of α and β. We proceed as follows:

i) We use the definitions of energy and angular momentum from Eqs. (4.22) and (4.23) to define the mappings for $p(\bar{p}, \bar{e}, f)$ and $e(\bar{p}, \bar{e}, f)$.

ii) We them employ NIT (see Sec. 4.3.2) to handle the mappings for $\omega(\bar{p}, \bar{e}, f)$ and $t(\bar{p}, \bar{e}, f)$.

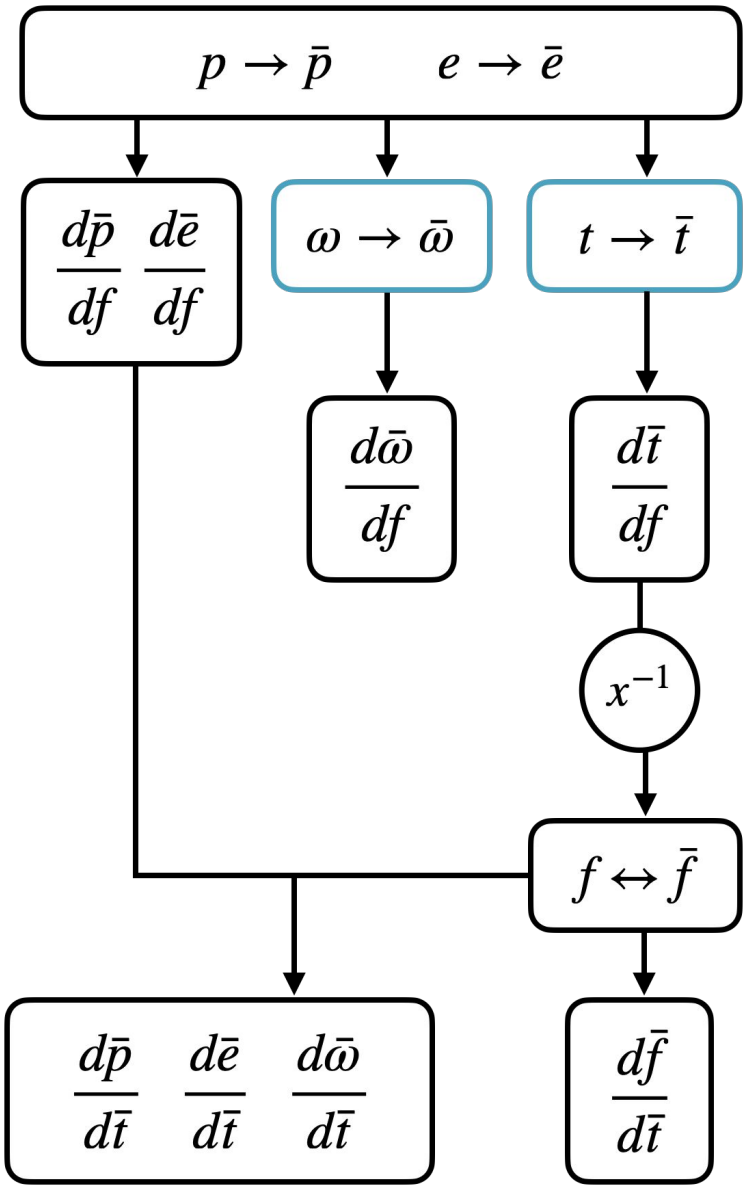

Figure 4.1: Derivation procedure for our new set of radiation-reaction, gauge-free evolutionary equations in terms of the characteristic parameters $\bar{p}$, $\bar{e}$, $\bar{\omega}$, $\bar{f}$. Light blue boxes indicate steps where NITs are used. The circular box labeled x^{-1} denotes where the inverse of the connected expression is taken. At any step, expansions in c^{-1} are performed and only terms up to $\mathcal{O}(c^{-5})$ are kept.

iii) The quantities f and $\bar{f}$ can be exchanged freely at the PN order here considered.

These mappings result in the evolutionary equations presented in Eqs. (4.2)–(4.5) above. A schematic representation of our procedure is presented in Fig. 4.1.

Before proceeding, let us comment on the ambiguities in this procedure. There is mathematical freedom in how one defines the mapping from the standard osculating quantities μ^σ to the new characteristic variables $\bar{\mu}^\sigma$. This is a result of the mathematical framework underpinning perturbation theory and is not related to gauge transformations in GR. Knowing this, how does one construct physically meaningful mappings? First, we enforce that the secular evolution of the binary, that is, Peters' equations in Eqs. (4.38)–(4.39) at the PN order we are considering, should remain invariant. Second, we use the secular approximation as a guide to choosing the mappings. For example, upon orbit averaging one has $\langle d\omega/dt\rangle = 0$, despite the fact that the full osculating equation $d\omega/dt$ in Eq. (4.37) does not necessarily vanish. The secular equation informs us that the orbit should not precess under radiation reaction, at least at leading PN order. We can thus use this fact to define the new characteristic variable $\bar{\omega}$. Similarly, from Eq. (4.22) and under orbit averaging, one has $\langle \mathcal{E}\rangle = E_{\rm N}$, which we use in part to obtain the characteristic variables $(\bar{p}, \bar{e})$. The full details of our procedure are presented below.

As a first step, we map the semi-latus rectum and the eccentricity to their redefined counterparts, $\bar{p}$ and $\bar{e}$. This mapping is achieved by requiring the following relations:

$$p = \bar{p} + \frac{1}{c^5}\delta\bar{p}\,(\bar{p}, \bar{e}, f, \alpha, \beta), \tag{4.46}$$

$$e = \bar{e} + \frac{1}{c^5}\delta\bar{e}\,(\bar{p}, \bar{e}, f, \alpha, \beta), \tag{4.47}$$

where $\delta\bar{p}$ and $\delta\bar{e}$ are generic unknown functions. To determine these functions, we

substitute Eqs. (4.46) and (4.47) into the expressions for $\mathcal{E}$ and $\mathcal{L}$, given in Eqs. (4.22) and (4.23), after expressing them in terms of the orbital elements using Eqs. (1.7)–(1.10).

Expanding the resulting expressions and retaining terms up to $\mathcal{O}(c^{-5})$, we impose the following conditions:

$$\mathcal{E} = \frac{M^2\eta}{2\bar{p}}\left(1-\bar{e}^2\right), \tag{4.48}$$

$$\mathcal{L} = M^{3/2}\eta\sqrt{\bar{p}}. \tag{4.49}$$

In doing this, i.e, requiring that the energy and angular momentum in the new barred variables are free from radiation-reaction gauge parameters, we find the following expressions for $\delta\bar{p}$ and $\delta\bar{e}$:

$$\delta\bar{p} = -\frac{16}{5}\frac{M^{5/2}}{\bar{p}^{3/2}}\,\eta\,(1+\bar{e}\cos f)^2\,\bar{e}\,\alpha\,\sin f, \tag{4.50}$$

$$\delta\bar{e} = -\frac{4}{5}\frac{M^{5/2}}{\bar{p}^{3/2}}\,\eta\,(1+\bar{e}\cos f)^2\,\{4+4\,\bar{e}\,(2+\alpha)\cos f+ \\ +\bar{e}^{\,2}[4+4\alpha-\beta+\beta\cos 2f]\}\sin f. \tag{4.51}$$

We specifically choose to employ $\mathcal{E}$ and $\mathcal{L}$ to carry out this step, as the semi-latus rectum and eccentricity, along with their respective evolution equations, are directly derived from these quantities and their derivatives. Finally, we differentiate Eqs. (4.46) and (4.47) with respect to f, solving for the derivatives of $\bar{p}$, $\bar{e}$.

Since no other constants of motion, such as energy or angular momentum, are available to map the remaining orbital parameters, we employ NITs. Our goal is to eliminate the gauge parameters α and β from $\mathrm{d}\omega/\mathrm{d}f$ and $\mathrm{d}t/\mathrm{d}f$. As these parameters appear only in terms $\propto c^{-5}$, this approach is consistent with the method described in

Sec. 4.3.2. We postulate the existence of the following NITs:

$$\omega = \bar{\omega} + \frac{1}{c^5}\delta\bar{\omega}(\bar{p}, \bar{e}, f, \alpha, \beta), \tag{4.52}$$

$$t = \bar{t} + \frac{1}{c^5}\delta\bar{t}(\bar{p}, \bar{e}, f, \alpha, \beta), \tag{4.53}$$

where $\delta\bar{\omega}$ and $\delta\bar{t}$ are unknown functions designed to remove the dependency on the gauge parameters. From Sec. 4.3.2, we define:

$$\delta\bar{\omega} = \int g(\bar{p}, \bar{e}, f, \alpha, \beta) - G(\bar{p}, \bar{e}, f)\mathrm{d}f, \tag{4.54}$$

$$\delta\bar{t} = \int s(\bar{p}, \bar{e}, f, \alpha, \beta) - S(\bar{p}, \bar{e}, f)\mathrm{d}f, \tag{4.55}$$

where g is the right-hand side of Eq. (4.37) divided by that of Eq. (4.36). This function can be decomposed as $g = g_{\mathrm{N}} + c^{-5}g_{2.5PN}$. Using this definition, we set $G = g_{\mathrm{N}}$. Similarly, s is defined as the reciprocal of the right-hand side of Eq. (4.36), rewritten as $s = s_{\mathrm{N}} + c^{-5}s_{2.5}$, from which we define $S = s_{\mathrm{N}}$. In all cases, we apply the mappings of Eqs. (4.47) and (4.46) and expand the resulting expressions in powers of c^{-1}, truncating them at $\mathcal{O}(c^{-5})$, obtaining the following expression for $\delta\bar{\omega}$ and $\delta\bar{t}$:

$$\begin{aligned}
\delta\bar{\omega} = \frac{1}{180}\frac{M^{5/2}}{\bar{p}^{5/2}}\frac{\eta}{\bar{e}}\Big\{&2304\cos\bar{f} + 96\,\bar{e}\,(23 + 3\alpha)\cos 2\bar{f} + \\
&+ \bar{e}^{\,2}[12\,(206 - 24\alpha + 18\beta)\cos f + 8\,(127 + 36\alpha + \\
&+ 9\beta)\cos 3\bar{f}] + \bar{e}^{\,3}[12\,(65 + 12\beta)\cos 2\bar{f} + 3\,(59 + \\
&+ 24\alpha + 24\beta)\cos 4\bar{f}\,] + \bar{e}^{\,4}[36\,(6 + \beta)\cos\bar{f} + 6\,(12 + \\
&+ 7\beta)\cos 3\bar{f} + 18\,\beta\cos 5\bar{f}\,]\Big\}\,, \\
\delta\bar{t} = \frac{2}{15}\frac{M^2}{\bar{p}}\frac{\eta}{\bar{e}^{\,2}}\Big\{&12\log\big(1 + \bar{e}\cos\bar{f}\,\big) + 84\,\bar{e}\cos\bar{f} +
\end{aligned} \tag{4.56}$$

$$+\bar{e}^2[(35+12\alpha)\cos 2\bar{f}-12\log\big(1+\bar{e}\cos\bar{f}\,\big)]+$$
$$+\bar{e}^3[(-12+12\alpha\,-\,9\,\beta)\cos\bar{f}+3\,\beta\cos 3\bar{f})]\big\}\,. \tag{4.57}$$

By differentiating Eqs. (4.52) and (4.53) with respect to f, using Eqs. (4.37) and (4.36), employing the new definition of $\bar{p}$ and $\bar{e}$ and, expanding the expressions in powers of c^{-1} retaining the terms up to $\mathcal{O}(c^{-5})$ we finally obtain $\mathrm{d}\bar{\omega}/\mathrm{d}f$ and $\mathrm{d}\bar{t}/\mathrm{d}f$.

To derive Eqs. (4.2), (4.3), and (4.5), we firstly divide $\mathrm{d}\bar{p}/\mathrm{d}f$, $\mathrm{d}\bar{e}/\mathrm{d}f$, $\mathrm{d}\bar{\omega}/\mathrm{d}f$ by $\mathrm{d}\bar{t}/\mathrm{d}f$. Then, we redefine f as

$$f=\bar{f}+\mathcal{O}(c^{-5}). \tag{4.58}$$

However, since f always appears as the argument of trigonometric functions in all expressions, expanding the resulting equations in powers of c^{-1} and truncating them at $\mathcal{O}(c^{-5})$ ensures that f is always interchangeable with $\bar{f}$.

It will not go unnoticed that Eqs. (4.5) and (4.4) align with those typically employed in a Newtonian framework. This is because, following the approach of Refs. [9, 7], we do not include 1PN and 2PN terms in our derivation. GWs solely extract energy and angular momentum from the system, leading only to variations in the semi-latus rectum and eccentricity. Since our analysis is restricted to radiation reaction effects, phenomena such as periastron precession [243, 9] are not captured by these equations, consistently with Ref. [46], but could be straightforwardly added using the methods of, e.g., Refs. [45, 244]. Finally, we provide some further information on the gauge parameters in this formalism. First, it is straightforward to show, by direct comparison, that no choice of (α,β) in Eqs. (4.34)–(4.36) can reproduce Eqs. (4.2)–(4.4). Thus, the characteristic variables and their evolutionary equations are not merely a suitable

gauge choice. Second, while we have removed the gauge parameters (α, β) from the evolution equations of the binary, they are, however, not completely removed from the two-body problem. The osculating formalism from which we started uses the mappings in Eqs. (1.7)–(1.10) for the orbital trajectory. Inserting these into the mappings in Eq. (4.46)–(4.47) and (4.50)–(4.51) reveals that the gauge parameters now appear inside of these coordinate trajectories. This is unsurprising: the gauge parameters describe different coordinate systems, and the trajectory is a coordinate-dependent quantity. Further, gauge parameters naturally arise as a result of extending perturbation theory to higher orders. The benefit of the characteristic parameters that we have derived is that they satisfy dynamical equations that are independent of these coordinate effects, and thus, one can obtain an unambiguous picture of BH binary dynamics in PN theory from them. Lastly, consistent with the osculating formalism, our equations remain valid for arbitrary values of eccentricity.

4.4 Non-adiabaticity in BH inspirals

We now investigate the consequences of our new set of equations and their adiabatic limit, which is equivalent to Peters' equations. We perform this investigation numerically due to the coupled and non-linear nature of the expressions involved. In this section, we adopt natural units with $G = c = 1$.

4.4.1 Numerical evolution

Figure 4.2 shows the evolution of the orbital elements for an equal-mass binary initialized with $\bar{p}_0 = 20M$, $\bar{e}_0 = 0.7$, $\bar{f}_0 = -\pi$ and $\bar{\omega}_0 = \pi$, employing the three methods described in Secs. 4.2.3, 4.2.4, and 4.3.3. We integrate from $\bar{t}_0 = 0$ to $\bar{t}_{\rm f} = 12933M$,

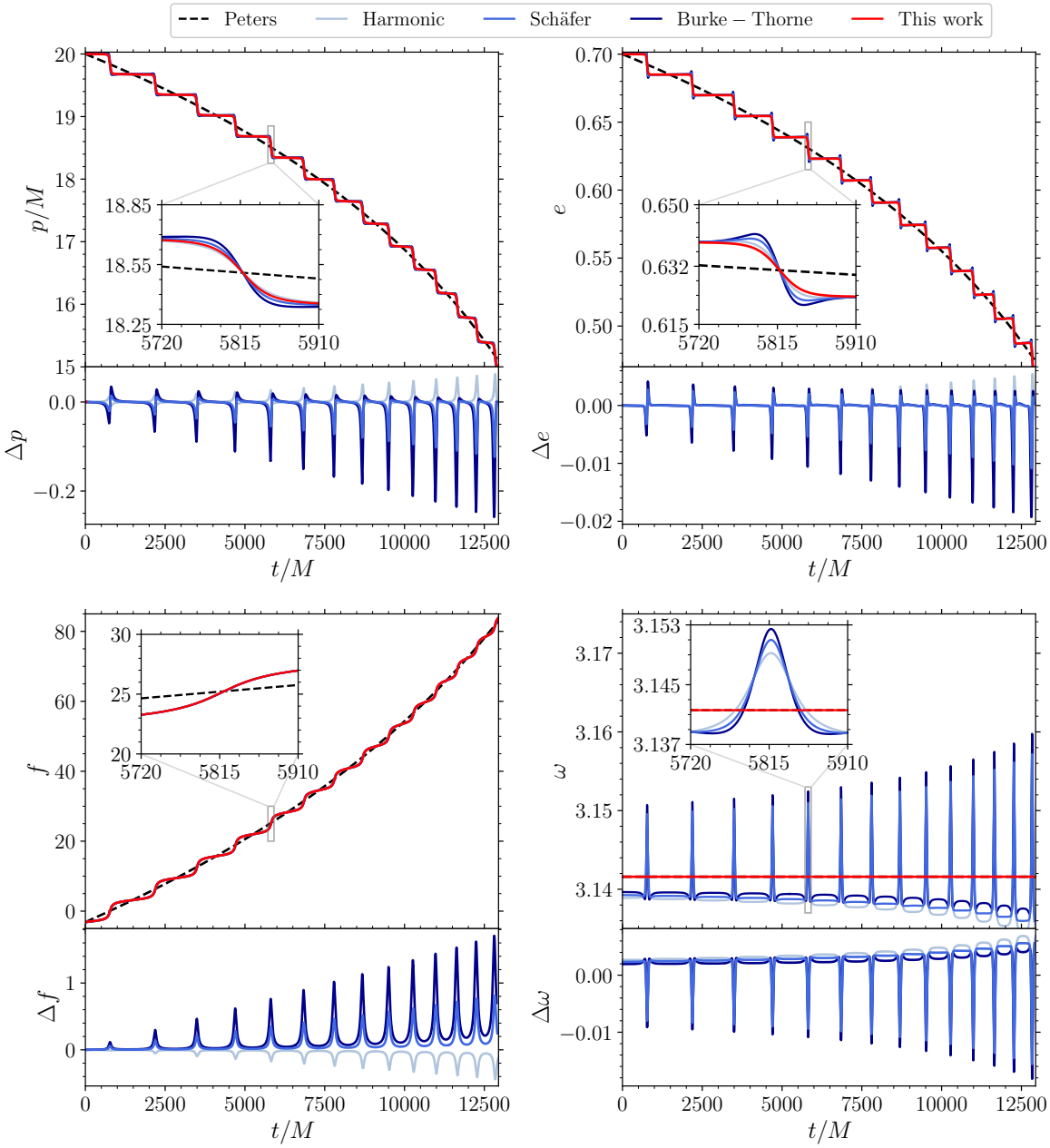

Figure 4.2: Evolution of the semi-latus rectum (top-left panel), eccentricity (top-right panel), true anomaly (bottom-left panel), and longitude of the pericenter (bottom-right panel) for a binary system with initial conditions $(\bar{p}_0, \bar{e}_0, \bar{f}_0, \bar{\omega}_0) = (20M, 0.7, -\pi, \pi)$. Binaries are evolved using different sets of equations: Peters' equations (dashed grey curve), Lagrangian planetary equations in the harmonic gauge (solid light blue curve), the Schäfer gauge (solid blue curve), and the Burke-Thorne gauge (solid dark blue curve), as well as the new set of equations presented in this chapter (solid red curve). The bottom subpanels of each panel show differences between the evolution obtained using the Lagrangian planetary equations and the gauge-free equations introduced in this work.

where the binary considered reaches a semi-latus rectum of $\bar{p}_{\rm f} = 15M$. The same initial values are used when comparing against Peters' equations, since at orders lower than 2.5PN the barred quantities coincide with their osculating counterparts. For the osculating equations, we convert the initial conditions using the mappings of Eqs. (4.46), (4.47), (4.52), and (4.53) for the three sets of gauge parameters introduced in Sec. 4.2.2: the Harmonic gauge, the Burke-Thorne gauge, and the Schäfer gauge. This ensures that the initial conditions for the osculating equations are identical to those used for our new equations for semi-latus rectum, eccentricity, and true anomaly, but show slight differences for ω_0 and t_0, which we summarize in Table 4.2.

Gauge	$\Delta\omega_0$	Δt_0
Harmonic	2.7×10^{-3}	1.7×10^{-1}
Burke-Thorne	1.9×10^{-3}	7.2×10^{-2}
Schäfer	2.3×10^{-3}	1.2×10^{-1}

Table 4.2: Difference between $\bar{\omega}_0$, $\bar{t}_0$ and ω_0, t_0 for the BH system described in Sec. 4.4.1. The quantities ω_0, t_0 are calculated from the initial values of the characteristic quantities as specified in Eq. (4.52) and (4.53).

Our method, along with the Lagrangian planetary equations, successfully reproduces the non-adiabatic emission of GWs: the orbital elements, specifically p and e, evolve in a step-like fashion, with drops occurring at pericenter passages where GW emission is the strongest. In contrast, Peters' equations capture only the secular evolution of these elements. At the same time, different gauge choices lead to distinct features in the evolution and, crucially, these differences lack a proper physical meaning. Among the four orbital elements, the evolution of ω, which in our case is absent as described in Sec. 4.3.3, is most prominently affected by these ambiguities. We emphasize once again that the evolution obtained using Eqs. (4.2)–(4.5) cannot be reproduced by any choice

of α and β.

4.4.2 Breakdown of the adiabatic approximation

Figure 4.2 shows that the orbital element evolution derived from Peters' equations aligns, on average, with the osculating evolution. Notably, no significant time shift is apparent, and all the examined evolutions reach approximately the same final values of eccentricity and semi-latus rectum at roughly the same time. This observation indicates that, while Peters' equations do not capture the finest details of the evolution, they provide a reliable treatment.

Conceptually, as highlighted in Sec. 4.2.4, orbital averaging should not be performed when the orbital parameters change on a timescale comparable to or shorter than the orbital period, i.e., when $\tau_{\rm rr} \lesssim \tau_{\rm orb}$. In Fig. 4.3, we illustrate the consequences of this orbital-averaging breakdown on the evolution of p and e. As in Fig. 4.2, we initialize three binaries with the same semi-latus rectum $\bar{p}_0 = 20M$ but different eccentricities $\bar{e}_0 = (0.5, 0.9, 0.99)$. We evolve these systems until they reach a final separation of $\bar{p}_f = 10M$, which we set as a conservative limit for our formalism and, more generally, for methods relying on the PN approximation [245, 246, 120]. Given a pair of initial conditions $(\bar{p}_0, \bar{e}_0)$, we compute one hundred evolutions with our non-adiabatic equations, each with a different initial true anomaly $\bar{f}_0$, and taking into account the non-uniform probability of finding a body along an eccentric orbit (that is Kepler's area law).

The mean of these evolutions is directly comparable to the evolution predicted by Peters' equations (which do not depend on the initial true anomaly). The time required for each system to reach the end of its evolution varies depending on the initial orbital positions.[2] In other words, BH binaries evolve at different rates depending

[2]We choose initial conditions such that $\bar{f}(t=0) = \bar{f}_0$, but on a Keplerian orbit, different values of

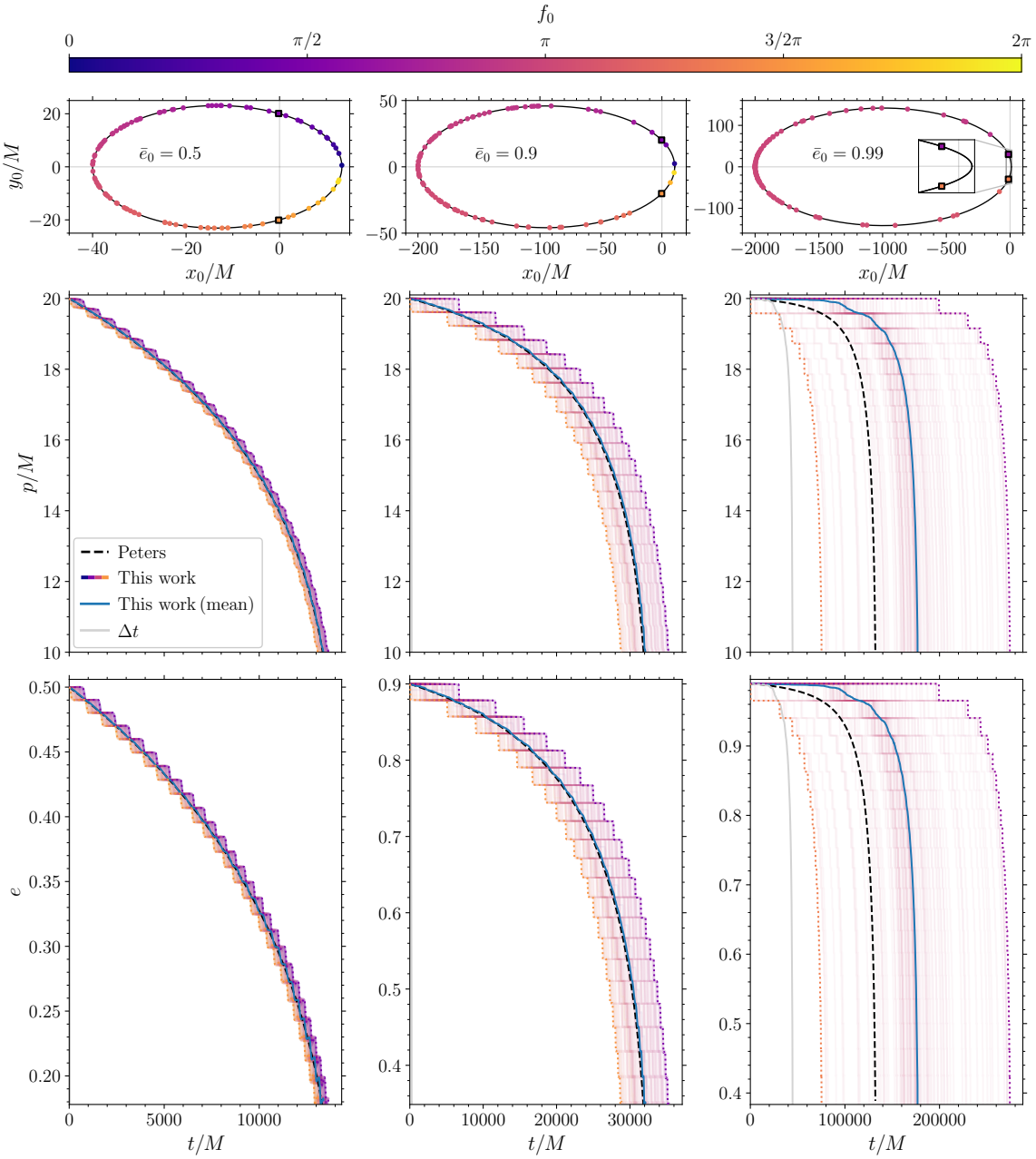

Figure 4.3: Evolution of the semi-latus rectum for binary systems with different initial eccentricities: $\bar{e}_0 = 0.5$ (left panel), $\bar{e}_0 = 0.9$ (central panel) and $\bar{e}_0 = 0.99$ (right panel), all with the same initial semi-latus rectum $\bar{p}_0 = 20M$ and concluding their evolution at $\bar{p}_0 = 10M$. For each pair $(\bar{p}_0, \bar{e}_0)$, we sampled 100 points along the initial elliptic orbit (top panels) and used the corresponding true anomaly as the initial condition for the evolution. The larger panels illustrate the evolution obtained using the equations presented in Sec. 4.3.3 (solid curves, colored according to the initial true anomaly) compared to Peters' equations (dashed black curves), which are insensitive to the initial starting point along the orbit. The mean evolution derived from our equations is shown in blue. The evolutions corresponding to the initial true anomalies marked by squares define the upper and lower boundaries enclosing all considered evolutions and are shown with dashed curves.

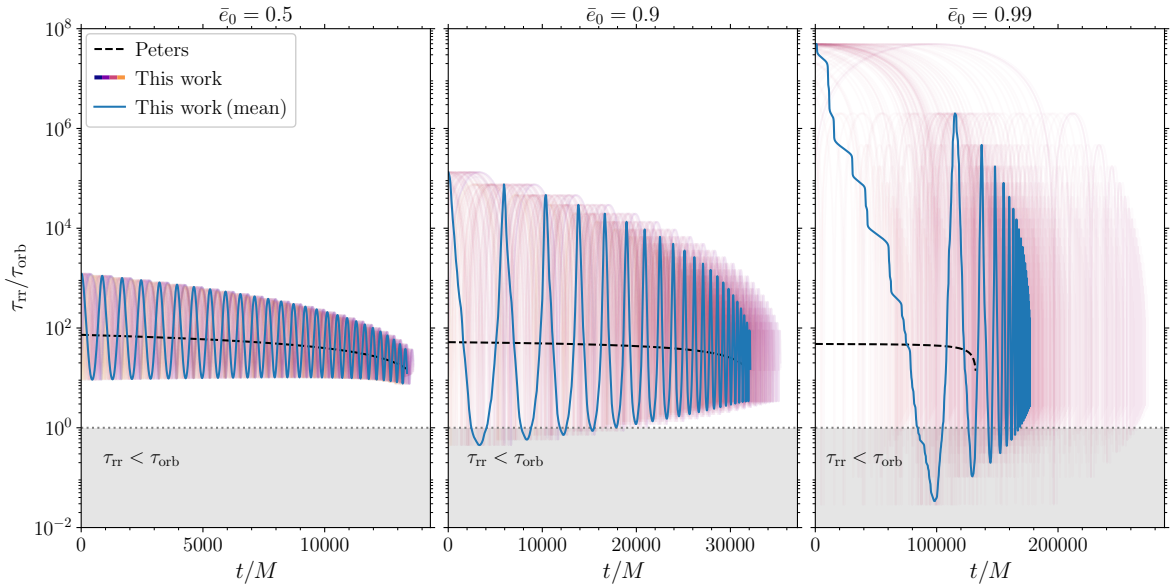

Figure 4.4: Evolution of the ratio $\tau_{\rm rr}/\tau_{\rm orb}$ for binary systems with different initial eccentricities: $\bar{e}_0 = 0.5$ (left panel), $\bar{e}_0 = 0.9$ (central panel), and $\bar{e}_0 = 0.99$ (right panel), all starting with the same initial semi-latus rectum $\bar{p}_0 = 20M$. The solid blue curves show the ratio's evolution, computed using the median values of $\bar{p}$, $\bar{e}$, and $\bar{f}$. The curves in a lighter shade show the timescale ratio for each of the evolutions presented in Fig. 4.3. The dashed black is computed using Peters' equations. The orbit-averaging procedure breaks down in the grey region where $\tau_{\rm rr} < \tau_{\rm orb}$.

on the positions of the two bodies along the same initial orbit. Second, when the eccentricity is small to moderate ($e_0 = 0.5$ and 0.9), the mean evolution obtained with our formalism is largely consistent with that of Peters'. This is not true in the highly eccentric case ($e_0 = 0.99$), where the evolution computed using Peters' equations is appreciably different from the mean of our non-adiabatic evolution.

To understand the reason for such divergence, Fig. 4.4 illustrates the evolution of the ratio $\tau_{\rm rr}/\tau_{\rm orb}$ for the same integrations of Fig. 4.3, measured using the single evolutions, their mean, as well as Peters' equations. It is important to note that, while $\tau_{\rm orb}$ is

$\bar{f}_0$ technically corresponds to different times by Kepler's equation. However, this formally reduces to an overall time shift in the solutions, which one always has the freedom to choose without affecting the underlying physics. If one corrects this, the spread in Fig. 4.3 collapses to the average.

independent of the position along the orbit [see Eq. (1.13)], $\tau_{\rm rr}$ from Eq. (4.40) depends on the true anomaly, leading to oscillations that correspond to the variations in the orbital elements. In the case of small eccentricity, the timescale hierarchy is always well respected. As the eccentricity increases, the system crosses the $\tau_{\rm rr} = \tau_{\rm orb}$ boundary somewhere during its evolution. As expected, this occurs at the periastron passage, where most of the gravitational radiation is emitted.

4.4.3 Parameter-space exploration

In Fig. 4.5, we extend these calculations by considering a larger set of initial values with $\bar{p}_0 \in [10M, 10^{2.5}M]$ and $\bar{e}_0 \in [0, 1)$. For each $(\bar{p}_0, \bar{e}_0)$, we evolve the binary using Peters' equations and our radiation-reaction-gauge-free, non-adiabatic equations until it reaches $\bar{p}_{\rm f} = 10M$. Since the last stable orbit corresponds to a semi-latus rectum of $p_{\rm LSO} = 2M(3+e)$, the evolutions reported remain within the regime where PN theory can still formally be defined, even in the most eccentric cases considered. As in Fig 4.3, we select one hundred values of $\bar{f}_0$ for each $(\bar{p}_0, \bar{e}_0)$, and compute the mean over the resulting evolutions. We then extract the time taken by the binary to complete the evolution, denoting the value obtained using Peters' equations as $t^{\rm P}_{\rm 10M}$ and the averaged value recovered with our non-adiabatic framework as $t^{\rm NA}_{\rm 10M}$. Specifically, we report the following quantity as a function of $(\bar{p}_0, \bar{e}_0)$:

$$\Delta t_{\rm 10M} = \frac{|t^{\rm P}_{\rm 10M} - t^{\rm NA}_{\rm 10M}|}{t^{\rm P}_{\rm 10M} + t^{\rm NA}_{\rm 10M}} \in [0, 1)\,. \tag{4.59}$$

The left panel of Fig. 4.5 shows that $\Delta t_{\rm 10M} \sim 1$ when the eccentricity is high and the semilatus rectum is small. Conversely, in regions where the binary separation is large and the eccentricity is small, $\Delta t_{\rm 10M}$ drops almost to zero, which implies Peters'

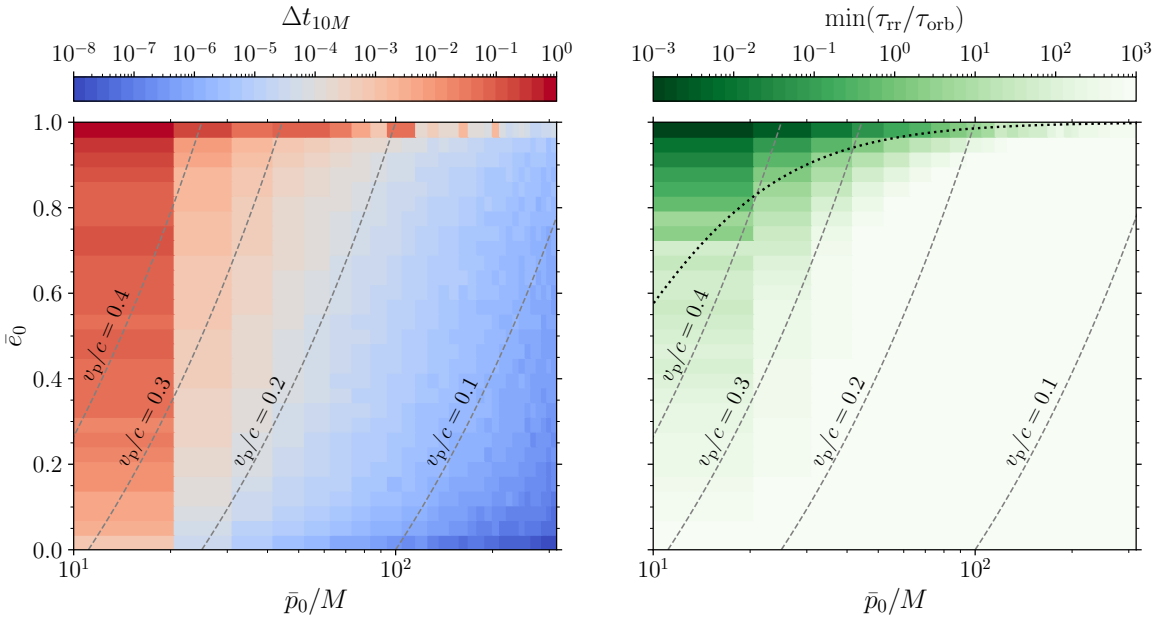

Figure 4.5: Breakdown of the orbital-average approximation in eccentric binary evolution across the parameter space. The left panel shows the normalized difference of the inspiral time $\Delta t_{10\rm M}$ between our formalism and Peters' as a function of the initial semi-latus rectum $\bar{p}_0$ and eccentricity $\bar{e}_0$. Specifically, we sample 100 initial values of the true anomaly for each pair (p_0, e_0). The right panel shows the timescale ratio $\tau_{\rm rr}/\tau_{\rm orb}$ for the mean evolution of these binaries. The dotted black curve indicates the separatrix of the timescale ratio, i.e., the point at which its minimum along the evolution is equal to one. This is approximated with the condition $\bar{f}_0 = \pi$. For reference, we report the contours of constant pericenter velocity $v_{\rm p}$ relative to the speed of light with dashed grey curves.

equations can be used reliably.

A symptom of the breakdown of the orbit-averaged approximation, as already noted in Sec. 4.4.2, is the inversion of the timescale hierarchy, i.e., $\tau_{\rm rr} \ll \tau_{\rm orb}$. Crucially, for evolutions carried out with our formalism, the timescale $\tau_{\rm rr}$ depends on f, meaning that knowing the initial values (p_0, e_0) is insufficient to determine whether the orbit-averaged approximation is valid. The right panel of Fig. 4.5 shows the minimum value of the timescale ratio $\tau_{\rm rr}/\tau_{\rm orb}$ along the inspiral, calculated using the mean evolution. This minimum occurs at the first pericenter passage, revealing that regions where

the timescale hierarchy is inverted, or equivalently where the ratio approaches unity, correspond to regions in the parameter space where the orbit-averaged approximation fails, resulting in $\Delta t_{10\mathrm{M}} \to 1$. The separatrix delineating the inversion of the timescale ratio is approximately given by the condition $\bar{f}_0 = \pi$. Finally, let us note that for scenarios with moderate to high initial eccentricities, the timescale hierarchy is restored in the later stages of evolution, corresponding to a significant decrease in eccentricity.

The non-adiabatic formalism we propose, similarly to the osculating equations, can also handle parabolic ($e = 1$) and hyperbolic ($e > 1$) orbits. Figure 4.6 presents three examples of generic binary systems, all starting with $\bar{p}_0 = 20M$, and considering $\bar{e}_0 = 0.9$ (top panel), $\bar{e}_0 = 1$ (middle panel), and $\bar{e}_0 = 1.01$ (bottom panel). We chose an initial value true anomaly in the proximity of $-\pi$ (where parabolic and hyperbolic orbits are singular), specifically setting at $\bar{f} = -3$ and $\bar{\omega}_0 = 0$. We evolve these binaries until they reach $\bar{p}_\mathrm{f} = 10M$. In both the parabolic and hyperbolic cases, binaries follow their respective unbound orbits before undergoing their first pericenter passage. During this event, a sufficient amount of energy is emitted via GW, causing the orbits to decay into bound elliptical trajectories.

4.4.4 Gauge effects

An additional example of the effects induced by the freedom to choose gauge parameters in the Lagrange planetary equations is illustrated in Fig. 4.7. We show the evolution of the timescale ratio $\tau_\mathrm{rr}/\tau_\mathrm{orb}$ for the binary system reported in Fig. 4.2, calculated using the Lagrangian planetary equations with three different gauge choices (see Sec. 4.4.1), Peters' equations, and our non-adiabatic formalism.

When using the Lagrangian planetary equations, this timescale ratio depends significantly on the choice of gauge, with prominent spurious features that vary over

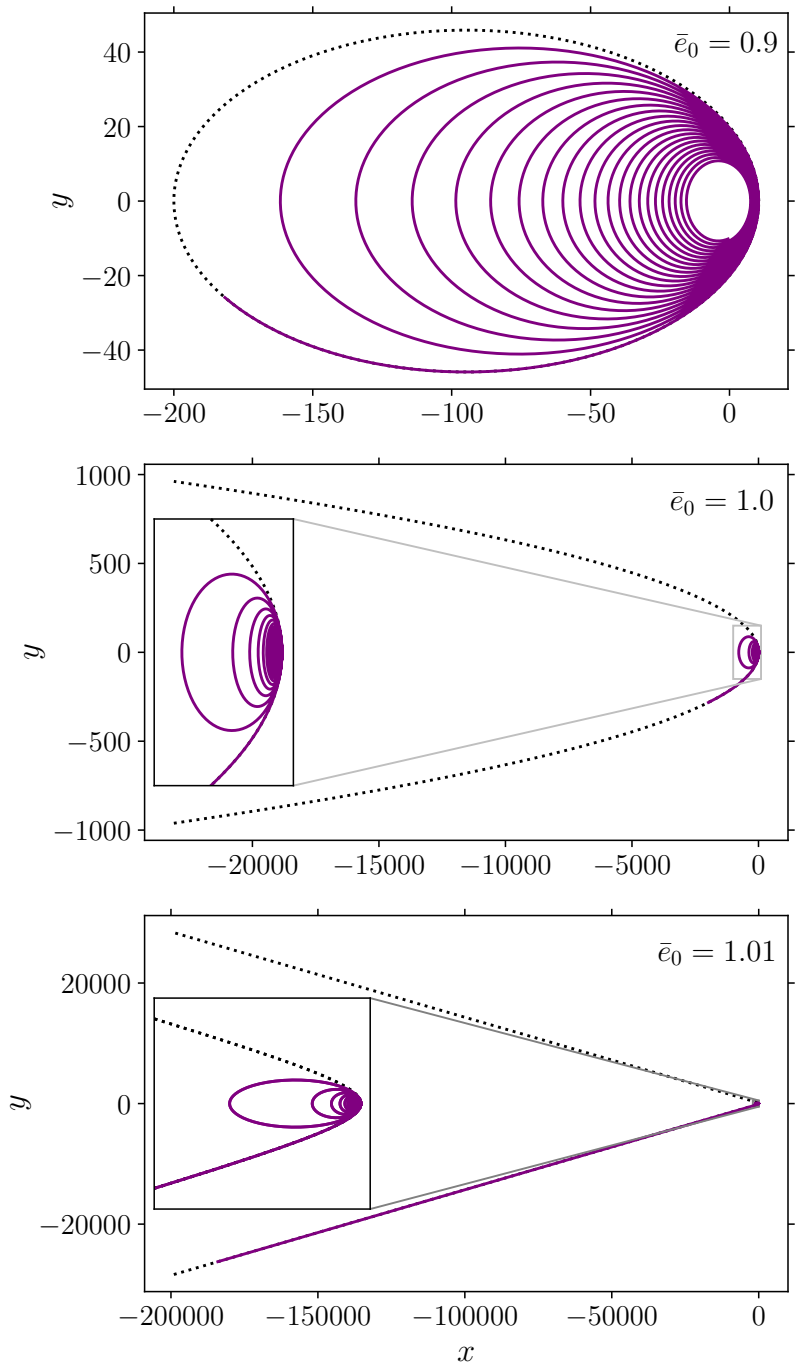

Figure 4.6: Time evolution of three binaries initially evolving on elliptical (top panel, $\bar{e}_0 = 0.9$), parabolic (middle panel, $\bar{e}_0 = 1$), and hyperbolic (bottom panel, $\bar{e}_0 = 1.01$) orbits. For all cases, we set $\bar{p}_0 = 20M$, $\bar{f}_0 = -3$, $\bar{\omega}_0 = 0$ and integrate up to $\bar{p}_{\rm f} = 10M$. The dotted black curves indicate the orbits described by the initial conditions. The purple curves are the non-adiabatic evolution under GW emission.

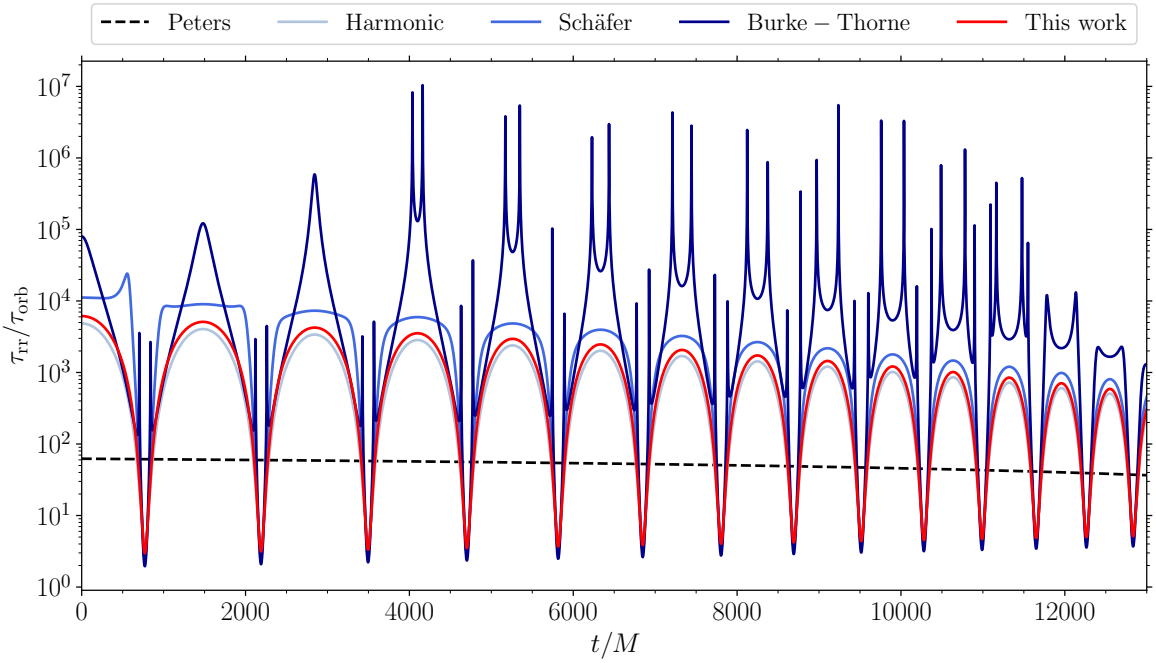

Figure 4.7: Evolution of the timescale ratio $\tau_{\rm rr}/\tau_{\rm orb}$ for the binary systems shown in Fig. 4.2. The solid curves in different shades of blue are computed using the Lagrangian planetary equation with three sets of gauge parameters (α, β): the harmonic gauge, the Schäfer gauge, and the Burke-Thorne gauge (from lighter to darker blue). The solid red curve is computed using our gauge-free equations. Finally, the dashed black curve is computed using Peters' orbit-averaged equations.

time. These variations are, once more, gauge artifacts and do not describe the physics of BH binaries. Among the three gauge choices, the harmonic gauge yields the smoothest evolution, resulting in evolutions that are somewhat closer to those predicted by our formalism (see also Fig. 4.2).

This sensitivity to gauge choices makes the Lagrangian planetary equations impractical for evaluating the breakdown of the orbital averaging approximation, as discussed in Sec. 4.4.1. In contrast, our formalism demonstrates a consistent behavior, free from spurious effects, while still capturing non-adiabatic effects.

4.5 Conclusion

4.5.1 Key findings

Eccentric binaries are among the most anticipated GW sources, with the potential to provide critical insights into the formation channels of BH binaries [71, 183]. These systems are key targets for current ground-based detectors and, in particular, for future space-based observatories like LISA [70, 247]. However, their accurate modeling remains challenging due to the non-adiabatic nature of GW emission, which significantly influences their orbital dynamics and long-term evolution.

In this work, we re-investigated the foundation of BH-binary dynamics in the PN regime and presented a non-adiabatic framework that is not affected by radiation-reaction gauge parameters, addressing the limitations of established methods such as the adiabatic approximation [16] and the Lagrangian planetary formalism [187]. The key result of this chapter is presented in Eqs. (4.2)–(4.4).

By eliminating the dependence on radiation-reaction gauge choices and avoiding orbit averaging, our formalism ensures a strictly physical, and therefore possibly observable, interpretation of the binary parameters and their evolution. This approach remains valid throughout the entire parameter space $(\bar{p}, \bar{e})$ where the PN approximation is applicable, including the parabolic and hyperbolic limits.

With these new equations, we quantify the regime of applicability of the popular Peters' equations, specifically that systems must satisfy the timescale condition $\tau_{\rm rr} \gg \tau_{\rm orb}$. Even if such a condition is widely known, our investigation highlights some non-trivial points. In particular, we find that:

(i) An inappropriate usage of Peters' equations can result in significant miscalculation

of the inspiral time of BH binaries, most crucially for binaries with large initial eccentricities and small semi-latus recta.

(ii) Initial conditions on eccentricity and semi-latus rectum (or equivalently semi-major axis) alone are insufficient to predict whether the orbit-averaging approximation breaks down. Instead, one must evaluate the timescale separation at the first periastron passage, which depends on the initial value of the true anomaly.

4.5.2 Implications

A detailed discussion of the astrophysical implications of our new set of equations is left for future work, including potential systematics in waveform modeling and astrophysical inference for eccentric BH binaries. For now, we provide some order-of-magnitude estimates of the differences in predictions obtained using our formalism and the common orbit-averaged approach.

Considering the three scenarios shown in Fig. 4.3, we assign physical units by setting a total mass of $60M_\odot$ and an initial semi-latus rectum of $\bar{p}_0 = 2 \times 10^{-3} R_\odot$. Table 4.3 shows the times required (and their differences) to complete the evolutions according to both Peters' equations and our new formalism. We consider the two extreme cases, i.e., the fastest and slowest evolution, corresponding to $\bar{f}_0 \approx \pi/2$ and $\bar{f}_0 \approx 3\pi/2$, respectively, together with the mean evolution. For the most eccentric case, the evolution time calculated when $\bar{f}_0 \approx 3\pi/2$ is larger than the value predicted by Peters' equations by about a factor of 2.

$\bar{e}_0$	$t^{\rm P}_{\rm 10M}$	$t^{\rm NA,\pi/2}_{\rm 10M}$	$t^{\rm NA,3\pi/2}_{\rm 10M}$	$t^{\rm NA}_{\rm 10M}$	Δt_{10M}
0.5	3.97	4.05 (0.09)	3.88 (0.08)	3.97 (0.01)	0.001
0.9	9.44	10.47 (1.03)	8.55 (0.89)	9.52 (0.08)	0.004
0.99	39.18	81.34 (42.16)	22.30 (16.87)	52.41 (13.23)	0.144

Table 4.3: Times, expressed in seconds, required to complete the evolutions shown in Fig. 4.3 for a non-spinning, equal-mass BH binary with $M = 60M_\odot$ and $\bar{p}_0 = 2 \times 10^{-3} R_\odot$, calculated using Peters' equations ($t^{\rm P}_{\rm 10M}$) and our formalism ($t^{\rm NA}_{\rm 10M}$) for $\bar{f}_0 \approx \pi/2$, $\bar{f}_0 \approx 3\pi/2$, and the mean evolution. In parentheses, we report the absolute difference between the inspiral times of our evolution and those from Peters'. Finally, the quantity Δt_{10M} is defined in Eq. (4.59).

4.5.3 Future prospects

This analysis could not be reliably performed using the Lagrangian planetary equations due to the presence of spurious and uncontrolled features in the evolution of the orbital parameters. However, it is worth stressing that the evolutions obtained when assuming the harmonic gauge produce the most consistent results, which are similar to those from our gauge-free method. To assess whether the proposed representation of the dynamics leads to a formally gauge-invariant description (in the sense of independence from gauge parameters, as is the case for globally defined quantities such as the total energy), one must now compute the energy and angular momentum fluxes. Due to the complexity of the calculation, we defer this analysis to future work.

This work is grounded in and directly compared to the osculating formalism, which incorporates the Newtonian and 2.5PN terms only in both the equations of motion and the definitions of energy and angular momentum. While terms up to 4.5PN are available, including both conservative and dissipative terms [248, 47], deriving Lagrangian planetary equations consistent with these higher orders requires a more detailed and careful treatment than that outlined in Sec. 4.2.3 as suggested in Ref. [46].

Most importantly, incorporating corrections to the dissipative terms at 3.5PN order introduces six new gauge parameters [7, 249], while employing 4.5PN corrections adds twelve additional gauge parameters. Although our method can, in principle, be extended to higher PN orders, including these corrections is non-trivial and would require a significantly more convoluted derivation. We leave such extensions to future work. Other non-adiabatic treatments of the dynamics of eccentric BH binaries have been presented in e.g., Ref. [250, 251], and a detailed comparison with those methods is another interesting avenue for future work. Finally, this study considers non-spinning black hole binaries. Chapters 2 and 3 are entirely dedicated to showing the correlation between the evolution of spin direction and eccentricity. Investigating how this new formalism influences this interplay, as well as the impact of spin on the evolution of eccentricity, is another important avenue that requires further careful study.

Chapter 5

Conclusions

"Our DeLorean consists of precession-averaged post-Newtonian evolutions."

–Mould and Gerosa (2022)

This chapter is a review of prior work and does not contain material previously published by the author in this form.

The discovery of the binary pulsar PSR1913+16 by Hulse and Taylor (1975) marked the birth of the two-body problem involving objects of comparable mass. This system was exceptional, as it exhibited nearly all the characteristics discussed throughout this thesis, including spins, eccentric orbits, and GW emission, and non-BH objects. Fifty years have elapsed, and the understanding of the dynamics of such systems remains an unresolved challenge and an active area of research, as this thesis intentionally seeks to demonstrate. As illustrated in Sec. 1.1, the pursuit of the equation of motion for a generic relativistic two-body system with comparable masses has a "long and tortuous history", initially driven by the necessity to compute the influence of relativistic effects on the observed times of arrival of PSR1913+16 and subsequently extended to assess their impact on the phase of potential GW emission.

When the comparable mass relativistic two-body problem was 40 years old, all the effort and time dedicated to calculating phases and accelerations ultimately yielded results. On September 15, 2015, the first direct detection of a binary BH merger was accomplished through GWs. Currently, after a decade, more than 200 such events have been observed. To interpret and detect these systems, an understanding of the equations of motion and a comprehensive knowledge of the dynamics of compact-object binaries is necessary. In GW astronomy, in order to discover phenomena, it is essential first to identify the possible sources. Theoretical waveform models must be applied to data streams to extract potential signals and, consequently, physical information about the systems that generated them.

A clear prediction derived from the dynamical formation scenario, as reported in Sec. 1.2, is that of compact binaries and, in particular, BH binaries, forming and evolving on highly eccentric orbits with the spin misaligned relative to the orbital angular momentum. This prediction markedly contrasts with the expectations of the isolated formation channels family, which anticipate quasi-circular orbits and spins that are either aligned or nearly aligned. Consequently, eccentricity and spin misalignment serve as parameters that can aid in distinguishing between these two primary formation hypotheses. Nevertheless, all such assertions have been characterized as *predictions* or *hypotheses*; therefore, although they certainly guide us in identifying relevant observational targets, they require empirical testing and comparison with observed signals to be validated as confirmed phenomena.

Using eccentricity and spin precession to understand the formation scenario of the binary that produced a GW signal is not as simple as using the values of the masses or spin magnitudes. This is because the former changes over time, while the latter stays constant. Suppose formation channels predict specific values for spin angles and

eccentricity at the moment of formation. How can we use their observed values at merger, considering that billions of years have passed between these two points? How do we handle the fact that during these long inspirals, GWs cause eccentricity to drop dangerously close to zero, leaving us with a vanishingly small quantity to measure? Here, understanding the overall dynamics, from formation to merger, makes all the difference.

This thesis focuses on the study of spin-precessing and eccentric BH binary systems. Our goal is to perform an in-depth analysis and improve understanding of the long-term evolution of these systems. In Chapter 2 we present a PN, multi-timescale analysis of these sources able to capture both precession and moderate eccentricity over long inspirals. We show that the evolution of an eccentric binary can be reduced to that of an effective source on quasi-circular orbits via an analytical rescaling of the spin-precession equations, coupled to a PN prescription for the secular evolution of the eccentricity. We then extend the double averaging approach presented in Gerosa *et al.* (2023), which was previously limited to quasi-circular sources, to accommodate eccentric ones. Consequently, we were able to examine the long-term evolution of these systems effectively, uncovering an interaction between precession and eccentricity: the spins of eccentric binaries undergo precession over shorter timescales, and their nutation amplitude is modified in comparison to those of BH on quasi-circular orbits. This both opens new avenues and complicates existing methods for understanding the formation scenarios. Since spins retain a memory of the eccentric past of the binary, we argue that it would be possible to extract information about eccentricity from spin angle measurements; on the other hand, if eccentricity cannot be adequately detected, all the analyses that attempt to reconstruct the spin history of BH binaries would be polluted by it. Specifically, to infer the formation channel, we usually rely on population

studies, which require spin angles to be backpropagated to past time infinity. In Chapter 3, we demonstrate that the ghost of undetectable residual eccentricity will haunt us in this operation and therefore must be marginalized over. In that chapter, we analyze, measure, and quantify the consequences of backpropagating spin angle posterior probability distributions, both with and without considering the non-detectable residual eccentricity. We consider both real events, up to those presented in GWTC-3, and simulated ones. Since the effects of eccentricity on spin precession depend on the magnitude of both, we show that for the real events analyzed, which do not show strong signs of spin precession and for which the spin angles are poorly measured, are not particularly influenced by residual eccentricity. Instead, when high SNR and highly precessing events are considered, the influence of eccentricity is substantial—signaling that this would become a problem in the near future, with the upgrade of detector sensitivity and the advent of LISA and third-generation detectors like the Einstein Telescope and Cosmic Explorer. To address these concerns, we use population synthesis codes. These codes can predict the distribution of eccentricity at merger and, crucially, the fraction of binaries with specific eccentricity values. With this information, we can marginalize over non-detectable eccentricities; however, this approach relies on the astrophysical models specifically used in the codes.

The content presented in Chap. 3 merely constitutes the preliminary stage. To accurately assess the real influence of residual eccentricity on the problem of formation channels, it is necessary to expand the scope of the investigation to a population-level analysis. As previously indicated, this requires back-propagating the spin measurements to past-time infinity [118]. This procedure is undertaken because, at that (non-physical) point of the evolution, the spin angles became constant, converging to a single value, which subsequently dictates the entire evolution. This characteristic is a known property

of quasi-circular spin-processing BH binaries [35], but, regrettably, it does not hold when eccentric orbits are taken into consideration. In such cases, as emphasized in Chaps. 2 and 3, the orbital angular momentum no longer diverges as $r \to \infty$.

How do we deal with spin-precessing and eccentric binaries at the population level? To address this question, we needed to go back to the beginning. In fact, in the regime of large separations, the formalism outlined in Chap. 2 becomes inapplicable. This framework depends on a strict hierarchy of timescales, which cannot be inverted or altered. In the case of circular orbits, it is consistently true that the orbital timescale is shorter than the precession timescale, which in turn is shorter than the radiation reaction timescale. However, this hierarchy does not hold for spinning and eccentric systems. It has long been recognized that the emission of GW in an eccentric system (disregarding spin effects) is inherently asymmetric due to the varying separation between the two bodies along the orbit, in contrast to the circular case. Notably, there are bursts of GW emission when the bodies are at pericenter relative to apocenter, where the emission is nearly negligible. The largest is the eccentricity; the closer the bodies pass to each other, the more intense the bursts of radiation become. This suggests that for a system characterized by high eccentricity, the hierarchy of timescales, which has to be observed in our approach, fails to hold. But when does this breakdown occur? At which eccentricities? Answering this question is as easy as comparing two numbers, but unfortunately, one of them is not as readily available. Specifically, knowledge of an accurate, i.e., one that does not rely on any approximation such as orbital averaging, radiation reaction timescale, requires knowledge of the evolution equations of the orbital elements (see Eq. (4.40)). However, recovering the latter bit of information is not straightforward. In Chap. 4 we explain why. If the reconstruction of spin histories is hindered by residual eccentricity, the PN-exact evolution of purely eccentric binaries

is hindered by radiation-reaction gauge parameters. These parameters are commonly present in the non-adiabatic evolution equation for eccentric systems, namely, the Lagrangian planetary equations. This means that the equations are ambiguous, and the evolution of eccentric systems, along with the definition of the radiation reaction timescale, depend on the specific choice of gauge parameters, which can assume arbitrary values. Clearly, we want to avoid this ambiguity, as it makes our already complicated problem even more convoluted.

In Chap. 4, we propose a possible solution to these issues by deriving a new set of non-adiabatic evolution equations for the orbital elements of non-spinning eccentric systems. These equations are expressed in a novel parameter set connected to their Keplerian counterparts via an analytical mapping, and are independent of radiation-reaction gauge parameters. With this new framework, we can analyze the dynamics of eccentric binaries and define the radiation reaction timescale without ambiguities, ultimately examining the breakdown of one component of the timescale hierarchy upon which our formalism is based: $\tau_{\rm orb} \ll \tau_{\rm rr}$. This again represents only the initial step, as it considers solely non-spinning systems and does not encompass all PN terms typically present.

This thesis opens more doors than it closes. The dynamics of spin precession and eccentric systems is rich and offer many future research prospects, such as those discussed in Sec. 2.6 regarding the generalization of spin precession to systems formed with non-BH objects, or the search for a formalism capable of building population distributions for spin-precessing and eccentric systems, as well as the subsequent extension of the formalisms presented in Chap. 2 to cover the entire parameter space, including high eccentricities based on those in Chap. 4.

These are just a few examples and are all symptoms of the complexity and beauty

of the relativistic two-body problem, which, after 50 years, still plays a pivotal role in GW astronomy, and its deep understanding remains a fascinating challenge that the theoretical community continues to pursue.

Bibliography

[1] F. Dostoevskij, *I demoni*, I Classici universale economica Feltrinelli (Feltrinelli, 2009).

[2] J. R. R. Tolkien, *The Fellowship of the Ring*, The Lord of the Rings, Vol. 1 (George Allen and Unwin, London, 1954).

[3] V. De Renzis and D. Gerosa, github.com/ViolaDeRenzis/twoprecessingspins, doi.org/10.5281/zenodo.6777952 (2022).

[4] R. Abbott et al., Phys. Rev. X **13**, 041039 (2023), arXiv:2111.03606 [gr-qc].

[5] M. Hannam, C. Hoy, J. E. Thompson, S. Fairhurst, V. Raymond, et al., Nature **610**, 652 (2022), arXiv:2112.11300 [gr-qc].

[6] B. R. Iyer and C. M. Will, Phys. Rev. Lett. **70**, 113 (1993).

[7] B. R. Iyer and C. M. Will, Phys. Rev. D **52**, 6882 (1995).

[8] C. W. Lincoln and C. M. Will, Phys. Rev. D **42**, 1123 (1990).

[9] E. Poisson and C. Will, *Gravity: Newtonian, Post-Newtonian, Relativistic* (Cambridge University Press, 2014).

[10] A. Einstein, L. Infeld, and B. Hoffmann, Annals of Mathematics **39**, 65 (1938).

[11] P. D. D'Eath, Phys. Rev. D **12**, 2183 (1975).

[12] A. Einstein, Sitzungsberichte der Königlich Preussischen Akademie der Wissenschaften , 831 (1915).

[13] M. Mathisson, Gen. Relat. Gravit. **42**, 1011 (2010).

[14] A. Papapetrou, P. R. Soc. Lond. A **209**, 248 (1951).

[15] P. C. Peters and J. Mathews, Phys. Rev. **131**, 435 (1963).

[16] P. C. Peters, Phys. Rev. **136**, 1224 (1964).

[17] L. I. Schiff, Proceedings of the National Academy of Science **46**, 871 (1960).

[18] B. M. Barker and R. F. O'Connell, Phys. Rev. D **12**, 329 (1975).

[19] B. M. Barker and R. F. Oconnell, Gen. Relat. Gravit. **11**, 149 (1979).

[20] R. A. Hulse and J. H. Taylor, Astrophys. J. Lett. **195**, L51 (1975).

[21] J. H. Taylor, L. A. Fowler, and P. M. McCulloch, Nature **277**, 437 (1979).

[22] G. Boerner, J. Ehlers, and E. Rudolph, Astron. Astrophys. **44**, 417 (1975).

[23] B. M. Barker and R. F. O'Connell, Astrophys. J. Lett. **199**, L25 (1975).

[24] K. S. Thorne and J. B. Hartle, Phys. Rev. D **31**, 1815 (1985).

[25] J. H. Taylor and J. M. Weisberg, Astrophys. J. **253**, 908 (1982).

[26] Nobel Prize Outreach, Press release (2025).

[27] Ligo: History (2025), accessed September 14, 2025.

[28] L. E. Kidder, C. M. Will, and A. G. Wiseman, Phys. Rev. D **47**, R4183 (1993), arXiv:gr-qc/9211025 [gr-qc].

[29] T. A. Apostolatos, C. Cutler, G. J. Sussman, and K. S. Thorne, Phys. Rev. D **49**, 6274 (1994).

[30] L. E. Kidder, Phys. Rev. D **52**, 821 (1995), arXiv:gr-qc/9506022 [gr-qc].

[31] E. Poisson, Phys. Rev. D **57**, 5287 (1998), arXiv:gr-qc/9709032 [gr-qc].

[32] É. Racine, Phys. Rev. D **78**, 044021 (2008), arXiv:0803.1820 [gr-qc].

[33] The LIGO Scientific Collaboration, the Virgo Collaboration, the KAGRA Collaboration, A. G. Abac, I. Abouelfettouh, F. Acernese, K. Ackley, S. Adhicary, D. Adhikari, N. Adhikari, et al., (2025), arXiv:2508.18080 [gr-qc].

[34] M. Kesden, D. Gerosa, R. O'Shaughnessy, E. Berti, and U. Sperhake, Phys. Rev. Lett. **114**, 081103 (2015), arXiv:1411.0674 [gr-qc].

[35] D. Gerosa, M. Kesden, U. Sperhake, E. Berti, and R. O'Shaughnessy, Phys. Rev. D **92**, 064016 (2015), arXiv:1506.03492 [gr-qc].

[36] B. P. Abbott, R. Abbott, T. D. Abbott, M. R. Abernathy, F. Acernese, K. Ackley, C. Adams, T. Adams, P. Addesso, R. X. Adhikari, et al., Phys. Rev. Lett. **116**, 061102 (2016), arXiv:1602.03837 [gr-qc].

[37] R. Abbott, T. D. Abbott, S. Abraham, F. Acernese, K. Ackley, C. Adams, R. X. Adhikari, V. B. Adya, C. Affeldt, M. Agathos, et al., Phys. Rev. D **102**, 043015 (2020), arXiv:2004.08342 [astro-ph.HE].

[38] R. Abbott, T. D. Abbott, S. Abraham, F. Acernese, K. Ackley, C. Adams, R. X. Adhikari, V. B. Adya, C. Affeldt, M. Agathos, et al., Phys. Rev. Lett. **125**, 101102 (2020), arXiv:2009.01075 [gr-qc].

[39] S. J. Miller, M. Isi, K. Chatziioannou, V. Varma, and I. Mandel, Phys. Rev. D **109**, 024024 (2024), arXiv:2310.01544 [astro-ph.HE].

[40] D. Gerosa, G. Fumagalli, M. Mould, G. Cavallotto, D. P. Monroy, D. Gangardt, and V. De Renzis, Phys. Rev. D **108**, 024042 (2023), arXiv:2304.04801 [gr-qc].

[41] A. Klein, Y. Boetzel, A. Gopakumar, P. Jetzer, and L. de Vittori, Phys. Rev. D **98**, 104043 (2018), arXiv:1801.08542 [gr-qc].

[42] A. Klein, (2021), arXiv:2106.10291 [gr-qc].

[43] K. S. Phukon, A. Gupta, S. Bose, and P. Jain, Phys. Rev. D **100**, 124008 (2019), arXiv:1904.03985 [gr-qc].

[44] C. Cutler, T. A. Apostolatos, L. Bildsten, L. S. Finn, E. E. Flanagan, D. Kennefick, D. M. Markovic, A. Ori, E. Poisson, G. J. Sussman, et al., Phys. Rev. Lett. **70**, 2984 (1993), arXiv:astro-ph/9208005 [astro-ph].

[45] T. Damour and N. Deruelle, Annales de L'Institut Henri Poincare Section (A) Physique Theorique **43**, 107 (1985).

[46] T. Damour, A. Gopakumar, and B. R. Iyer, Phys. Rev. D **70**, 064028 (2004), arXiv:gr-qc/0404128 [astro-ph].

[47] C. Königsdörffer and A. Gopakumar, Phys. Rev. D **73**, 124012 (2006), arXiv:gr-qc/0603056 [gr-qc].

[48] K. G. Arun, L. Blanchet, B. R. Iyer, and M. S. S. Qusailah, Phys. Rev. D **77**, 064034 (2008), arXiv:0711.0250 [gr-qc].

[49] A. Tucker and C. M. Will, Phys. Rev. D **104**, 104023 (2021), arXiv:2108.12210 [gr-qc].

[50] N. Loutrel, S. Liebersbach, N. Yunes, and N. Cornish, Class. Quantum Grav. **36**, 025004 (2019), arXiv:1810.03521 [gr-qc].

[51] M. Boschini, N. Loutrel, D. Gerosa, and G. Fumagalli, Phys. Rev. D **111**, 024008 (2025), arXiv:2411.00098 [gr-qc].

[52] M. E. Lower, E. Thrane, P. D. Lasky, and R. Smith, Phys. Rev. D **98**, 083028 (2018), arXiv:1806.05350 [astro-ph.HE].

[53] I. M. Romero-Shaw, D. Gerosa, and N. Loutrel, Mon. Not. R. Astron. Soc. **519**, 5352 (2023), arXiv:2211.07528 [astro-ph.HE].

[54] A. G. Abac, R. Abbott, H. Abe, F. Acernese, K. Ackley, C. Adamcewicz, S. Adhicary, N. Adhikari, R. X. Adhikari, V. K. Adkins, et al., Astrophys. J. **973**, 132 (2024), arXiv:2308.03822 [astro-ph.HE].

[55] I. Romero-Shaw, P. D. Lasky, and E. Thrane, Astrophys. J. **940**, 171 (2022), arXiv:2206.14695 [astro-ph.HE].

[56] N. Gupte, A. Ramos-Buades, A. Buonanno, J. Gair, M. C. Miller, M. Dax, S. R. Green, M. Pürrer, J. Wildberger, J. Macke, et al., (2024), arXiv:2404.14286 [gr-qc].

[57] I. Romero-Shaw, J. Stegmann, H. Tagawa, D. Gerosa, J. Samsing, N. Gupte, and S. R. Green, (2025), arXiv:2506.17105 [astro-ph.HE].

[58] The LIGO Scientific Collaboration, the Virgo Collaboration, the KAGRA Collaboration, A. G. Abac, I. Abouelfettouh, F. Acernese, K. Ackley, C. Adamcewicz, S. Adhicary, D. Adhikari, et al., (2025), arXiv:2508.18082 [gr-qc].

[59] LIGO Scientific Collaboration and Virgo Collaboration and KAGRA Collaboration, Ligo, virgo and kagra observing run plans (2025), accessed: 2025-09-16.

[60] A. G. Abac, R. Abbott, I. Abouelfettouh, F. Acernese, K. Ackley, S. Adhicary, N. Adhikari, R. X. Adhikari, V. K. Adkins, D. Agarwal, et al., Astrophys. J. Lett. **970**, L34 (2024), arXiv:2404.04248 [astro-ph.HE].

[61] The LIGO Scientific Collaboration, the Virgo Collaboration, the KAGRA Collaboration, A. G. Abac, I. Abouelfettouh, F. Acernese, K. Ackley, C. Adamcewicz, S. Adhicary, D. Adhikari, et al., (2025), arXiv:2507.08219 [astro-ph.HE].

[62] M. Mapelli, in *Handbook of Gravitational Wave Astronomy* (Springer, 2021) p. 16.

[63] D. Gerosa and M. Fishbach, Nat. Astron. **5**, 749 (2021), arXiv:2105.03439 [astro-ph.HE].

[64] I. Mandel and A. Farmer, Phys. Rep. **955**, 1 (2022), arXiv:1806.05820 [astro-ph.HE].

[65] I. Mandel and F. S. Broekgaarden, Living Rev. Relativ. **25**, 1 (2022), arXiv:2107.14239 [astro-ph.HE].

[66] M. Zevin, C. Pankow, C. L. Rodriguez, L. Sampson, E. Chase, V. Kalogera, and F. A. Rasio, Astrophys. J. **846**, 82 (2017), arXiv:1704.07379 [astro-ph.HE].

[67] A. Q. Cheng, M. Zevin, and S. Vitale, Astrophys. J. **955**, 127 (2023), arXiv:2307.03129 [astro-ph.HE].

[68] M. Zevin, S. S. Bavera, C. P. L. Berry, V. Kalogera, T. Fragos, P. Marchant, C. L. Rodriguez, F. Antonini, D. E. Holz, and C. Pankow, Astrophys. J. **910**, 152 (2021), arXiv:2011.10057 [astro-ph.HE].

[69] D. Gerosa, E. Berti, R. O'Shaughnessy, K. Belczynski, M. Kesden, D. Wysocki, and W. Gladysz, Phys. Rev. D **98**, 084036 (2018), arXiv:1808.02491 [astro-ph.HE].

[70] J. Samsing, Phys. Rev. D **97**, 103014 (2018), arXiv:1711.07452 [astro-ph.HE].

[71] M. Zevin, I. M. Romero-Shaw, K. Kremer, E. Thrane, and P. D. Lasky, Astrophys. J. Lett. **921**, L43 (2021), arXiv:2106.09042 [astro-ph.HE].

[72] S. Torniamenti, M. Mapelli, C. Périgois, M. Arca Sedda, M. C. Artale, M. Dall'Amico, and M. P. Vaccaro, Astron. Astrophys. **688**, A148 (2024), arXiv:2401.14837 [astro-ph.HE].

[73] A. Olejak and K. Belczynski, Astrophys. J. Lett. **921**, L2 (2021), arXiv:2109.06872 [astro-ph.HE].

[74] H. Tagawa, B. Kocsis, Z. Haiman, I. Bartos, K. Omukai, and J. Samsing, Astrophys. J. Lett. **907**, L20 (2021), arXiv:2010.10526 [astro-ph.HE].

[75] S. Naoz, Annu. Rev. Astron. Astrophys. **54**, 441 (2016), arXiv:1601.07175 [astro-ph.EP].

[76] A. Sesana, Front. Astron. Space Sci. **8**, 7 (2021), arXiv:2105.11518 [astro-ph.CO].

[77] D. Gerosa, M. Kesden, E. Berti, R. O'Shaughnessy, and U. Sperhake, Phys. Rev. D **87**, 104028 (2013), arXiv:1302.4442 [gr-qc].

[78] C. L. Rodriguez, M. Zevin, C. Pankow, V. Kalogera, and F. A. Rasio, Astrophys. J. Lett. **832**, L2 (2016), arXiv:1609.05916 [astro-ph.HE].

[79] S. Vitale, R. Lynch, R. Sturani, and P. Graff, Class. Quantum Grav. **34**, 03LT01 (2017), arXiv:1503.04307 [gr-qc].

[80] S. Stevenson, C. P. L. Berry, and I. Mandel, Mon. Not. R. Astron. Soc. **471**, 2801 (2017), arXiv:1703.06873 [astro-ph.HE].

[81] S. S. Bavera, T. Fragos, Y. Qin, E. Zapartas, C. J. Neijssel, I. Mandel, A. Batta, S. M. Gaebel, C. Kimball, and S. Stevenson, Astron. Astrophys. **635**, A97 (2020), arXiv:1906.12257 [astro-ph.HE].

[82] S. Banerjee, A. Olejak, and K. Belczynski, Astrophys. J. **953**, 80 (2023), arXiv:2302.10851 [astro-ph.HE].

[83] J. Samsing, M. MacLeod, and E. Ramirez-Ruiz, Astrophys. J. **784**, 71 (2014), arXiv:1308.2964 [astro-ph.HE].

[84] F. Antonini, I. M. Romero-Shaw, and T. Callister, Phys. Rev. Lett. **134**, 011401 (2025), arXiv:2406.19044 [astro-ph.HE].

[85] G. Fumagalli and D. Gerosa, Phys. Rev. D **108**, 124055 (2023), arXiv:2310.16893 [gr-qc].

[86] G. Morras, G. Pratten, and P. Schmidt, Phys. Rev. D **111**, 084052 (2025), arXiv:2502.03929 [gr-qc].

[87] M. A. Scheel, M. Boyle, K. Mitman, N. Deppe, L. C. Stein, C. Armaza, M. S. Bonilla, L. T. Buchman, A. Ceja, H. Chaudhary, et al., (2025), arXiv:2505.13378 [gr-qc].

[88] J. Healy and C. O. Lousto, Phys. Rev. D **105**, 124010 (2022), arXiv:2202.00018 [gr-qc].

[89] D. Ferguson, E. Allsup, S. Anne, G. Bouyer, M. Gracia-Linares, H. Iglesias, A. Jan, P. Laguna, J. Lange, E. Martinez, et al., Phys. Rev. D **112**, 044043 (2025), arXiv:2309.00262 [gr-qc].

[90] G. Pratten, C. García-Quirós, M. Colleoni, A. Ramos-Buades, H. Estellés, M. Mateu-Lucena, R. Jaume, M. Haney, D. Keitel, J. E. Thompson, et al., Phys. Rev. D **103**, 104056 (2021), arXiv:2004.06503 [gr-qc].

[91] M. Colleoni, F. A. Ramis Vidal, N. K. Johnson-McDaniel, T. Dietrich, M. Haney, and G. Pratten, Phys. Rev. D **111**, 064025 (2025), arXiv:2311.15978 [gr-qc].

[92] G. Fumagalli, I. Romero-Shaw, D. Gerosa, V. De Renzis, K. Kritos, and A. Olejak, Phys. Rev. D **110**, 063012 (2024), arXiv:2405.14945 [astro-ph.HE].

[93] G. Fumagalli, N. Loutrel, D. Gerosa, and M. Boschini, Phys. Rev. D **112**, 024012 (2025), arXiv:2502.06952 [gr-qc].

[94] C. Misner, K. Thorne, and J. Wheeler, *Gravitation* (Princeton University Press, 1973).

[95] W. D. Goldberger and I. Z. Rothstein, Phys. Rev. D **73**, 104029 (2006), arXiv:hep-th/0409156 [hep-th].

[96] R. A. Porto, (2016), arXiv:1601.04914 [hep-th].

[97] T. Damour, Phys. Rev. D **64**, 124013 (2001), arXiv:gr-qc/0103018 [gr-qc].

[98] J. D. Schnittman, Phys. Rev. D **70**, 124020 (2004), arXiv:astro-ph/0409174 [astro-ph].

[99] Ž. Ivezić, A. J. Connolly, J. T. VanderPlas, and A. Gray, *Statistics, Data Mining, and Machine Learning in Astronomy. A Practical Python Guide for the Analysis of Survey Data, Updated Edition* (2020).

[100] G. Fumagalli, D. Gerosa, and N. Loutrel, (2025), arXiv:2508.21125 [gr-qc].

[101] V. De Renzis, D. Gerosa, G. Pratten, P. Schmidt, and M. Mould, Phys. Rev. D **106**, 084040 (2022), arXiv:2207.00030 [gr-qc].

[102] K. Kritos, V. Strokov, V. Baibhav, and E. Berti, Phys. Rev. D **110**, 043023 (2024), arXiv:2210.10055 [astro-ph.HE].

[103] A. Olejak, C. L. Fryer, K. Belczynski, and V. Baibhav, Mon. Not. R. Astron. Soc. **516**, 2252 (2022), arXiv:2204.09061 [astro-ph.HE].

[104] J. Stegmann, D. Gerosa, I. Romero-Shaw, G. Fumagalli, H. Tagawa, and L. Zwick, (2025), arXiv:2505.13589 [astro-ph.HE].

[105] D. Gerosa, G. Foroni, G. Fumagalli, and E. Berti, (2025), arXiv:2508.19735 [gr-qc].

[106] G. Fumagalli, G. Shaifullah, and A. Sesana, Astron. Astrophys. **697**, A25 (2025), arXiv:2311.01505 [astro-ph.HE].

[107] Università degli Studi di Milano, Meetmetonight 2025 (2025), accessed: 2025-10-13.

[108] G. Morras, G. Pratten, and P. Schmidt, (2025), arXiv:2503.15393 [astro-ph.HE].

[109] E. Payne, S. Hourihane, J. Golomb, R. Udall, D. Davis, and K. Chatziioannou, Phys. Rev. D **106**, 104017 (2022), arXiv:2206.11932 [gr-qc].

[110] T. Islam, V. Varma, J. Lodman, S. E. Field, G. Khanna, M. A. Scheel, H. P. Pfeiffer, D. Gerosa, and L. E. Kidder, Phys. Rev. D **103**, 064022 (2021), arXiv:2101.11798 [gr-qc].

[111] A. Ramos-Buades, A. Buonanno, M. Khalil, and S. Ossokine, Phys. Rev. D **105**, 044035 (2022), arXiv:2112.06952 [gr-qc].

[112] A. Nagar, P. Rettegno, R. Gamba, S. Albanesi, A. Albertini, and S. Bernuzzi, Phys. Rev. D **108**, 124018 (2023), arXiv:2304.09662 [gr-qc].

[113] A. M. Knee, I. M. Romero-Shaw, P. D. Lasky, J. McIver, and E. Thrane, Astrophys. J. **936**, 172 (2022), arXiv:2207.14346 [gr-qc].

[114] M. Garg, S. Tiwari, A. Derdzinski, J. G. Baker, S. Marsat, and L. Mayer, Mon. Not. R. Astron. Soc. **528**, 4176 (2024), arXiv:2307.13367 [astro-ph.GA].

[115] A. Klein and P. Jetzer, Phys. Rev. D **81**, 124001 (2010), arXiv:1005.2046 [gr-qc].

[116] H. Yu, S. Ma, M. Giesler, and Y. Chen, Phys. Rev. D **102**, 123009 (2020), arXiv:2007.12978 [gr-qc].

[117] N. K. Johnson-McDaniel, S. Kulkarni, and A. Gupta, Phys. Rev. D **106**, 023001 (2022), arXiv:2107.11902 [astro-ph.HE].

[118] M. Mould and D. Gerosa, Phys. Rev. D **105**, 024076 (2022), arXiv:2110.05507 [astro-ph.HE].

[119] B. Moore and N. Yunes, Class. Quantum Grav. **36**, 185003 (2019), arXiv:1903.05203 [gr-qc].

[120] A. Buonanno, B. R. Iyer, E. Ochsner, Y. Pan, and B. S. Sathyaprakash, Phys. Rev. D **80**, 084043 (2009), arXiv:0907.0700 [gr-qc].

[121] N. Loutrel and N. Yunes, Class. Quantum Grav. **34**, 135011 (2017), arXiv:1702.01818 [gr-qc].

[122] L. Á. Gergely, Z. I. Perjés, and M. Vasúth, Phys. Rev. D **58**, 124001 (1998), arXiv:gr-qc/9808063 [gr-qc].

[123] W. M. Farr, S. Stevenson, M. C. Miller, I. Mandel, B. Farr, and A. Vecchio, Nature **548**, 426 (2017), arXiv:1706.01385 [astro-ph.HE].

[124] S. Stevenson, A. Vigna-Gómez, I. Mandel, J. W. Barrett, C. J. Neijssel, D. Perkins, and S. E. de Mink, Nature Communications **8**, 14906 (2017), arXiv:1704.01352 [astro-ph.HE].

[125] N. Steinle and M. Kesden, Phys. Rev. D **103**, 063032 (2021), arXiv:2010.00078 [astro-ph.HE].

[126] L. Reali, M. Mould, D. Gerosa, and V. Varma, Class. Quantum Grav. **37**, 225005 (2020), arXiv:2005.01747 [gr-qc].

[127] D. Gerosa and M. Kesden, Phys. Rev. D **93**, 124066 (2016), arXiv:1605.01067 [astro-ph.HE].

[128] L. Wen, Astrophys. J. **598**, 419 (2003), arXiv:astro-ph/0211492 [astro-ph].

[129] A. S. Hamers, Res. Notes AAS **5**, 275 (2021), arXiv:2111.08033 [gr-qc].

[130] W. G. Laarakkers and E. Poisson, Astrophys. J. **512**, 282 (1999), arXiv:gr-qc/9709033 [gr-qc].

[131] I. Harry and T. Hinderer, Class. Quantum Grav. **35**, 145010 (2018), arXiv:1801.09972 [gr-qc].

[132] F. D. Ryan, Phys. Rev. D **55**, 6081 (1997).

[133] C. A. R. Herdeiro and E. Radu, Phys. Rev. Lett. **112**, 221101 (2014), arXiv:1403.2757 [gr-qc].

[134] M. LaHaye, H. Yang, B. Bonga, and Z. Lyu, Phys. Rev. D **108**, 043018 (2023), arXiv:2212.04657 [gr-qc].

[135] F. Douchin and P. Haensel, Astron. Astrophys. **380**, 151 (2001), arXiv:astro-ph/0111092 [astro-ph].

[136] K. Yagi and N. Yunes, Phys. Rep. **681**, 1 (2017).

[137] B. P. Abbott et al., Phys. Rev. X **9**, 031040 (2019), arXiv:1811.12907 [astro-ph.HE].

[138] R. Abbott et al., Phys. Rev. X **11**, 021053 (2021), arXiv:2010.14527 [gr-qc].

[139] R. Abbott et al., Phys. Rev. D **109**, 022001 (2024), arXiv:2108.01045 [gr-qc].

[140] I. M. Romero-Shaw, P. D. Lasky, and E. Thrane, Mon. Not. R. Astron. Soc. **490**, 5210 (2019), arXiv:1909.05466 [astro-ph.HE].

[141] S. Kulkarni, N. K. Johnson-McDaniel, K. S. Phukon, N. V. Krishnendu, and A. Gupta, Phys. Rev. D **109**, 043002 (2024), arXiv:2308.05098 [astro-ph.HE].

[142] R. Abbott et al., Phys. Rev. X **13**, 011048 (2023), arXiv:2111.03634 [astro-ph.HE].

[143] K. W. K. Wong, E. D. Kovetz, C. Cutler, and E. Berti, Phys. Rev. Lett. **121**, 251102 (2018), arXiv:1808.08247 [astro-ph.HE].

[144] D. Gerosa, S. Ma, K. W. K. Wong, E. Berti, R. O'Shaughnessy, Y. Chen, and K. Belczynski, Phys. Rev. D **99**, 103004 (2019), arXiv:1902.00021 [astro-ph.HE].

[145] B. Ewing, S. Sachdev, S. Borhanian, and B. S. Sathyaprakash, Phys. Rev. D **103**, 023025 (2021), arXiv:2011.03036 [gr-qc].

[146] A. Toubiana, S. Babak, S. Marsat, and S. Ossokine, Phys. Rev. D **106**, 104034 (2022), arXiv:2206.12439 [gr-qc].

[147] B. P. Abbott et al., Astrophys. J. **883**, 149 (2019).

[148] A. G. Abac et al., (2023), arXiv:2308.03822 [astro-ph.HE].

[149] K. Kremer, C. S. Ye, N. Z. Rui, N. C. Weatherford, S. Chatterjee, G. Fragione, C. L. Rodriguez, M. Spera, and F. A. Rasio, Astrophys. J. Supp. S. **247**, 48 (2020), arXiv:1911.00018 [astro-ph.HE].

[150] K. Kritos, V. Strokov, V. Baibhav, and E. Berti, (2022), arXiv:2210.10055 [astro-ph.HE].

[151] P. Schmidt, F. Ohme, and M. Hannam, Phys. Rev. D **91**, 024043 (2015), arXiv:1408.1810 [gr-qc].

[152] D. Gerosa, M. Mould, D. Gangardt, P. Schmidt, G. Pratten, and L. M. Thomas, Phys. Rev. D **103**, 064067 (2021), arXiv:2011.11948 [gr-qc].

[153] I. Romero-Shaw, P. D. Lasky, and E. Thrane, Astrophys. J. Lett. **921**, L31 (2021), arXiv:2108.01284 [astro-ph.HE].

[154] K. Belczynski, J. Klencki, C. E. Fields, A. Olejak, E. Berti, G. Meynet, C. L. Fryer, D. E. Holz, R. O'Shaughnessy, D. A. Brown, et al., Astron. Astrophys. **636**, A104 (2020), arXiv:1706.07053 [astro-ph.HE].

[155] M. Mapelli, Front. Astron. Space Sci. **7**, 38 (2020), arXiv:2105.12455 [astro-ph.HE].

[156] F. Antonini and M. Gieles, Mon. Not. R. Astron. Soc. **492**, 2936 (2020), arXiv:1906.11855 [astro-ph.HE].

[157] S. Ossokine, A. Buonanno, S. Marsat, R. Cotesta, S. Babak, T. Dietrich, R. Haas, I. Hinder, H. P. Pfeiffer, M. Pürrer, et al., Phys. Rev. D **102**, 044055 (2020), arXiv:2004.09442 [gr-qc].

[158] V. Varma, S. E. Field, M. A. Scheel, J. Blackman, D. Gerosa, L. C. Stein, L. E. Kidder, and H. P. Pfeiffer, Phys. Rev. Res. **1**, 033015 (2019), arXiv:1905.09300 [gr-qc].

[159] V. Varma, S. Biscoveanu, T. Islam, F. H. Shaik, C.-J. Haster, M. Isi, W. M. Farr, S. E. Field, and S. Vitale, Phys. Rev. Lett. **128**, 191102 (2022), arXiv:2201.01302 [astro-ph.HE].

[160] J. Chung, P. Kannappan, C. T. Ng, and P. Sahoo, J. Math. Anal. Appl **138**, 280 (1989).

[161] C. J. Moore and D. Gerosa, Phys. Rev. D **104**, 083008 (2021), arXiv:2108.02462 [gr-qc].

[162] A. G. Abac, I. Abouelfettouh, F. Acernese, K. Ackley, C. Adamcewicz, S. Adhicary, D. Adhikari, N. Adhikari, R. X. Adhikari, V. K. Adkins, et al., Phys. Rev. Lett. **135**, 111403 (2025), arXiv:2509.08054 [gr-qc].

[163] S. Yi, A. Kuntz, E. Barausse, E. Berti, M. H.-Y. Cheung, K. Kritos, and A. Maselli, Phys. Rev. D **109**, 124029 (2024), arXiv:2403.09767 [gr-qc].

[164] A. Olejak, J. Klencki, X.-T. Xu, C. Wang, K. Belczynski, and J.-P. Lasota, Astron. Astrophys. **689**, A305 (2024), arXiv:2404.12426 [astro-ph.HE].

[165] L. S. Finn and D. F. Chernoff, Phys. Rev. D **47**, 2198 (1993), arXiv:gr-qc/9301003 [gr-qc].

[166] D. Gerosa and M. Bellotti, Class. Quantum Grav. **41**, 125002 (2024), arXiv:2404.16930 [astro-ph.HE].

[167] D. Gerosa, github.com/dgerosa/gwdet, doi.org/10.5281/zenodo.889966 (2017).

[168] P. Saini, Mon. Not. R. Astron. Soc. **528**, 833 (2024), arXiv:2308.07565 [astro-ph.HE].

[169] J. Samsing, I. Bartos, D. J. D'Orazio, Z. Haiman, B. Kocsis, N. W. C. Leigh, B. Liu, M. E. Pessah, and H. Tagawa, Nature **603**, 237 (2022), arXiv:2010.09765 [astro-ph.HE].

[170] A. A. Trani, S. Rastello, U. N. Di Carlo, F. Santoliquido, A. Tanikawa, and M. Mapelli, Mon. Not. R. Astron. Soc. **511**, 1362 (2022), arXiv:2111.06388 [astro-ph.HE].

[171] A. Vigna-Gómez, E. Grishin, J. Stegmann, A. Olejak, S. A. Popa, B. Liu, A. S. Rajamuthukumar, L. A. C. van Son, A. Bobrick, and A. Dorozsmai, Astron. Astrophys. **699**, A272 (2025), arXiv:2503.17006 [astro-ph.SR].

[172] J. Stegmann and F. Antonini, Phys. Rev. D **103**, 063007 (2021), arXiv:2012.06329 [astro-ph.HE].

[173] B. McKernan, K. E. S. Ford, T. Callister, W. M. Farr, R. O'Shaughnessy, R. Smith, E. Thrane, and A. Vajpeyi, Mon. Not. R. Astron. Soc. **514**, 3886 (2022), arXiv:2107.07551 [astro-ph.HE].

[174] T. M. Tauris, Astrophys. J. **938**, 66 (2022), arXiv:2205.02541 [astro-ph.HE].

[175] M. Mould, D. Gerosa, F. S. Broekgaarden, and N. Steinle, Mon. Not. R. Astron. Soc. **517**, 2738 (2022), arXiv:2205.12329 [astro-ph.HE].

[176] A. Santini, D. Gerosa, R. Cotesta, and E. Berti, Phys. Rev. D **108**, 083033 (2023), arXiv:2308.12998 [astro-ph.HE].

[177] C. Adamcewicz, S. Galaudage, P. D. Lasky, and E. Thrane, Astrophys. J. Lett. **964**, L6 (2024), arXiv:2311.05182 [astro-ph.HE].

[178] The LIGO Scientific Collaboration, the Virgo Collaboration, the KAGRA Collaboration, A. G. Abac, I. Abouelfettouh, F. Acernese, K. Ackley, C. Adamcewicz, S. Adhicary, D. Adhikari, et al., (2025), arXiv:2508.18083 [astro-ph.HE].

[179] R. Buscicchio, A. Klein, E. Roebber, C. J. Moore, D. Gerosa, E. Finch, and A. Vecchio, Phys. Rev. D **104**, 044065 (2021), arXiv:2106.05259 [astro-ph.HE].

[180] M. Colpi, K. Danzmann, M. Hewitson, K. Holley-Bockelmann, P. Jetzer, G. Nelemans, A. Petiteau, D. Shoemaker, C. Sopuerta, R. Stebbins, et al., (2024), arXiv:2402.07571 [astro-ph.CO].

[181] D. Reitze, R. X. Adhikari, S. Ballmer, B. Barish, L. Barsotti, G. Billingsley, D. A. Brown, Y. Chen, D. Coyne, R. Eisenstein, et al., in *Bull. Am. Astron. Soc.*, Vol. 51 (2019) p. 35, arXiv:1907.04833 [astro-ph.IM].

[182] N. DePorzio, L. Randall, and Z.-Z. Xianyu, (2024), arXiv:2402.09513 [gr-qc].

[183] M. Zeeshan and R. O'Shaughnessy, Phys. Rev. D **110**, 063009 (2024), arXiv:2404.08185 [gr-qc].

[184] D. J. D'Orazio and J. Samsing, Mon. Not. R. Astron. Soc. **481**, 4775 (2018), arXiv:1805.06194 [astro-ph.HE].

[185] J. Samsing and D. J. D'Orazio, Mon. Not. R. Astron. Soc. **481**, 5445 (2018), arXiv:1804.06519 [astro-ph.HE].

[186] J. Samsing and D. J. D'Orazio, Phys. Rev. D **99**, 063006 (2019), arXiv:1807.08864 [astro-ph.HE].

[187] C. W. Lincoln and C. M. Will, Phys. Rev. D **42**, 1123 (1990).

[188] T. Damour, A. Gopakumar, and B. R. Iyer, Phys. Rev. D **70**, 064028 (2004), arXiv:gr-qc/0404128.

[189] A. Pound, E. Poisson, and B. G. Nickel, Phys. Rev. D **72**, 124001 (2005), arXiv:gr-qc/0509122.

[190] M. A. Shaikh, V. Varma, H. P. Pfeiffer, A. Ramos-Buades, and M. van de Meent, Phys. Rev. D **108**, 104007 (2023), arXiv:2302.11257 [gr-qc].

[191] M. Boschini, N. Loutrel, D. Gerosa, and G. Fumagalli, Phys. Rev. D **111**, 024008 (2025), arXiv:2411.00098 [gr-qc].

[192] L. Gondán and B. Kocsis, Mon. Not. R. Astron. Soc. **506**, 1665 (2021), arXiv:2011.02507 [astro-ph.HE].

[193] B. Rom, R. Sari, and D. Lai, Astrophys. J. **964**, 43 (2024), arXiv:2310.03801 [astro-ph.HE].

[194] M. Dall'Amico, M. Mapelli, S. Torniamenti, and M. A. Sedda, Astron. Astrophys. **683**, A186 (2024), arXiv:2303.07421 [astro-ph.HE].

[195] T. Osburn, N. Warburton, and C. R. Evans, Phys. Rev. D **93**, 064024 (2016), arXiv:1511.01498 [gr-qc].

[196] I. M. Romero-Shaw, S. Goorachurn, M. Siwek, and C. J. Moore, Mon. Not. R. Astron. Soc. **534**, L58 (2024), arXiv:2407.03869 [astro-ph.HE].

[197] A. Sesana, Class. Quantum Grav. **30**, 244009 (2013), arXiv:1307.4086 [astro-ph.CO].

[198] A. Gualandris, F. M. Khan, E. Bortolas, M. Bonetti, A. Sesana, P. Berczik, and K. Holley-Bockelmann, Mon. Not. R. Astron. Soc. **511**, 4753 (2022), arXiv:2201.08646 [astro-ph.GA].

[199] L. Landau and E. Lifshitz, *The Classical Theory of Fields: Volume 2* (Elsevier Science, 1975).

[200] M. Maggiore, *Gravitational Waves: Volume 1: Theory and Experiments* (Oxford University Press, 2008).

[201] L. Blanchet, Living Rev. Relativ. **27**, 4 (2024), arXiv:1310.1528v6 [gr-qc].

[202] B. R. Iyer and C. M. Will, Phys. Rev. Lett. **70**, 113 (1993).

[203] T. Mora and C. M. Will, Phys. Rev. D **66**, 101501 (2002), arXiv:gr-qc/0208089.

[204] R. A. Isaacson, Phys. Rev. **166**, 1263 (1968).

[205] R. A. Isaacson, Phys. Rev. **166**, 1272 (1968).

[206] C. M. Bender and S. A. Orszag, *Advanced Mathematical Methods for Scientists and Engineers* (McGraw-Hill, 1978).

[207] N. Loutrel, S. Liebersbach, N. Yunes, and N. Cornish, Class. Quantum Grav. **36**, 01LT01 (2019), arXiv:1801.09009 [gr-qc].

[208] M. Turner, Astrophys. J. **216**, 610 (1977).

[209] N. Loutrel, Class. Quantum Grav. **40**, 215004 (2023), arXiv:2304.00836 [gr-qc].

[210] F. Antonini, S. Chatterjee, C. L. Rodriguez, M. Morscher, B. Pattabiraman, V. Kalogera, and F. A. Rasio, Astrophys. J. **816**, 65 (2016), arXiv:1509.05080 [astro-ph.GA].

[211] J. C. Neu, SIAM J. Appl. Math. **38**, 189 (1980).

[212] N. Krylov, N. Bogoliubov, and S. Lefschetz, *Introduction to Non-linear Mechanics* (Princeton University Press, 1949).

[213] D. Smith, *Singular-Perturbation Theory: An Introduction with Applications* (Cambridge University Press, 1985).

[214] S. Chandrasekhar, Astrophys. J. **142**, 1488 (1965).

[215] S. Chandrasekhar and Y. Nutku, Astrophys. J. **158**, 55 (1969).

[216] C. M. Will, Class. Quantum Grav. **36**, 195013 (2019), arXiv:1906.08064 [gr-qc].

[217] G. Schaefer, Lett. Nuovo Cim. **36**, 105 (1983).

[218] K. S. Thorne, Rev. Mod. Phys. **52**, 299 (1980).

[219] W. L. Burke, J. Math. Phys. **12**, 401 (1971).

[220] P. Lynch, V. Witzany, M. van de Meent, and N. Warburton, Class. Quantum Grav. **41**, 225002 (2024), arXiv:2405.21072 [gr-qc].

[221] L. Witten, *Gravitation: an Introduction to current research* (Wiley, 1962).

[222] D. Kennefick, *Traveling at the Speed of Thought: Einstein and the Quest for Gravitational Waves* (Princeton University Press, 2007).

[223] A. Saffer, N. Yunes, and K. Yagi, Class. Quantum Grav. **35**, 055011 (2018), arXiv:1710.08863 [gr-qc].

[224] D. Su and Y. Zhang, Phys. Rev. D **85**, 104012 (2012), arXiv:1204.0089 [gr-qc].

[225] L. V. Verozub, Annalen Phys. **17**, 28 (2008), arXiv:0801.3425 [gr-qc].

[226] K. S. Thorne, Rev. Mod. Phys. **52**, 299 (1980).

[227] D. R. Brill and J. B. Hartle, Phys. Rev. **135**, 271 (1964).

[228] A. Gopakumar, B. R. Iyer, and S. Iyer, Phys. Rev. D **55**, 6030 (1997), arXiv:gr-qc/9703075 [gr-qc].

[229] L. Blanchet, Phys. Rev. D **55**, 714 (1997), arXiv:gr-qc/9609049 [gr-qc].

[230] K. G. Arun, L. Blanchet, B. R. Iyer, and S. Sinha, Phys. Rev. D **80**, 124018 (2009), arXiv:0908.3854 [gr-qc].

[231] L. Blanchet, Living Rev. Relativ. **5**, 3 (2002), arXiv:gr-qc/0202016 [gr-qc].

[232] W. Junker and G. Schaefer, Mon. Not. R. Astron. Soc. **254**, 146 (1992).

[233] T. Damour and N. Deruelle, Phys. Lett. A **87**, 81 (1981).

[234] G. Schaefer, Lett. Nuovo Cim. **36**, 105 (1983).

[235] K. S. Thorne, Astrophys. J. **158**, 997 (1969).

[236] W. L. Burke, J. Math. Phys. **12**, 401 (1971).

[237] D. Griffiths, *Introduction to Electrodynamics* (Pearson, 2014).

[238] G. Schott, The London, Edinburgh, and Dublin Philosophical Magazine and Journal of Science **29**, 49 (1915).

[239] Ø. Grøn, in *Springer Handbook of Spacetime* (2014) p. 165.

[240] C. R. Galley, A. K. Leibovich, R. A. Porto, and A. Ross, Phys. Rev. D **93**, 124010 (2016), arXiv:1511.07379 [gr-qc].

[241] M. van de Meent and N. Warburton, Class. Quantum Grav. **35**, 144003 (2018), arXiv:1802.05281 [gr-qc].

[242] P. Lynch, M. van de Meent, and N. Warburton, Class. Quantum Grav. **39**, 145004 (2022), arXiv:2112.05651 [gr-qc].

[243] T. Damour and G. Schafer, Nuovo Cim. B **101**, 127 (1988).

[244] T. Mora and C. M. Will, Phys. Rev. D **69**, 104021 (2004), [Erratum: Phys. Rev. D 71, 129901 (2005)], arXiv:gr-qc/0312082.

[245] A. Buonanno, Y. Chen, and T. Damour, Phys. Rev. D **74**, 104005 (2006), arXiv:gr-qc/0508067 [gr-qc].

[246] M. Campanelli, C. O. Lousto, H. Nakano, and Y. Zlochower, Phys. Rev. D **79**, 084010 (2009), arXiv:0808.0713 [gr-qc].

[247] J. Samsing and D. J. D'Orazio, Mon. Not. R. Astron. Soc. **481**, 5445 (2018), arXiv:1804.06519 [astro-ph.HE].

[248] M. E. Pati and C. M. Will, Phys. Rev. D **65**, 104008 (2002), arXiv:gr-qc/0201001 [gr-qc].

[249] L. Blanchet, G. Faye, and D. Trestini, Class. Quantum Grav. **42**, 065015 (2025), arXiv:2407.18295 [gr-qc].

[250] S. Tanay, L. C. Stein, and J. T. Gálvez Ghersi, Phys. Rev. D **103**, 064066 (2021), arXiv:2012.06586 [gr-qc].

[251] S. Tanay, L. C. Stein, and G. Cho, Phys. Rev. D **107**, 103040 (2023), arXiv:2110.15351 [gr-qc].